Comparison of observations and modelling of surface mass balance variations in East Antarctica

Author:

Bianca Kallenberg

A thesis submitted for the degree of Doctor of Philosophy
of the Australian National University

June 2016

I hereby declare that the material contained in my thesis is entirely my own work, except of where accurate acknowledgement of another source has been made

Bianca Kallenberg

Acknowledgements

My greatest gratitude goes to my supervisor Paul Tregoning for providing me with the opportunity to conduct my research project, his guidance and encouragement throughout my studies and for giving me the once in a lifetime opportunity to travel to Antarctica for a closely related research project.

I would like to express my great appreciation to Anthony Purcell for his never ending patience and guidance in teaching programming skills and setting up my code. My sincerer gratitude goes to Rhys Hawkins for all his help and support in solving remaining and newly occurring issues within my codes, for always being around to answer questions and his effort to help solving issues, and to put me back on track during my last months.

I wish to acknowledge Stefan Ligtenberg for his forthcoming support in explaining his model, for providing me with the RACMO data set and his model results, and his general help in establishing my program.

I would like to thank Achraf Koulali, Sebastien Allgeyer, Evan Gowan, Janosch Hoffman and Christopher Watson for their advice, guidance and help on any question I threw on them, programming issues and Antarctic research.

A special thank goes to Lydie Lescarmontier, not only for her support and advice in glaciology but for her great company and supervision during our stay in Antarctica, her friendship, support and her lovely cooking during the last month of my PhD.

I would like to thank my parents for their love and support, and for always believing into me. I would like to thank my friends in Germany for good times whenever I visit and of course all my friends here at RSES who made these past years an unforgettable time. This includes my friends at the paddocks and my incredible sweet horses Betsy and Shackleton, who always cheer me up regardless of how I feel, and who give me so many amazing moments.

Last but not least all my love and thankfulness goes to my partner Kris Currie for his never-ending patience, his support and for being my rock, walking with me all the way to the end of a long rocky road.

Abstract

Mass balance changes of the Antarctic ice sheet are of significant interest due to its sensitivity to climatic changes and the contribution to changes in global sea level that is makes. In recent years, the Antarctic ice sheet has experienced increased temperatures inducing surface melting, accelerated ice flow and ice discharge but also an increase in accumulation. Geodetic observations suggest variable behaviour across the ice sheet, with an increase in mass over a vast area of East Antarctica and substantial thinning in West Antarctica.

Despite considerable improvement on surface mass balance estimates using a variety of techniques, disparity remains mainly due to uncertainties of each method and the unknown contribution of glacial isostatic adjustment, the response of the lithosphere to prolonged surface loads. Estimates of bedrock uplift rates are limited and existing models are poorly constrained due to the lack of observations as a result of the extensive permanent ice coverage in Antarctica.

This study investigates the possibility of combining and comparing altimetry and gravity observations by employing a regional climate model to simulate near surface climate and firn compaction, to separate the contributing ice sheet mass balance components of surface mass, firn compaction, ice dynamics and glacial isostatic adjustment within the observed signals. The region of interest covers an area including Enderby, Kemp and Mac.Robertson Land, in East Antarctica, an area where an increase in ice mass and ice height has been recorded over the past decade. Despite the general agreement that the positive signal is primarily related to increased snowfall, large uncertainties remain in bedrock uplift rates in this region due to the lack of observations.

Estimates of ice dynamic rates are obtained by removing modelled surface elevation variations, due to surface mass and firn compaction, from altimetry observations, which are subsequently employed in models of mass variations to compare with gravimetric observations.

Table of Contents

Chapter 1

Introduction

Understanding and estimating surface mass balance of the Antarctic Ice Sheet is of great interest, as the melting of the ice sheet contributes significantly to global sea level changes. With a volume of ice of ~27 million km^3 the Antarctic Ice Sheet (AIS) contains ~88% of all terrestrial ice [Fretwell et al., 2013] and is the largest ice sheet on Earth. The remaining ice can be found in the Greenland Ice Sheet (~11%) and within smaller ice fields (~1%) such as permafrost and glaciers in the Himalayas, Patagonia, and Alaska [Solomon, 2007; Allison, et al., 2009].

The amount of freshwater held within the AIS is equivalent to 58.3 m of global sea level rise, with a potential contribution of 53.3 m from the East Antarctic Ice Sheet and 4.3 m from the West Antarctic Ice Sheet [Fretwell et al., 2013]. In comparison, the entire Greenland Ice Sheet contains an equivalent of 7.4 m of global sea level rise [Bamber et al., 2013]. Despite the fact that global sea level has varied in the past, it had not changed significantly for several thousand years until the late 19th century [Church et al., 2011]. Church & White [2011] found a rate of sea level rise of 1.7 ± 0.2 mm/year from 1900 to 2009, with an increase of 2.1 ± 0.2 mm/year between 1972 and 2008 alone [Church et al., 2011]. The rate at which global sea level is increasing appears to be accelerating, especially since the late 20th century [Church and White, 2011; Watson et al., 2015]. This correlates well with the beginning of rising global temperatures and, with global temperatures continuing to rise and major cities situated along coastlines, this will remain a serious concern in the future [Church et al., 2011]. Therefore, it is of great importance to understand how present-day temperatures and potentially increasing future temperatures affect ice mass balance, and to what extent the AIS may contribute to future changes in global sea level.

To determine the contribution of the Antarctic Ice Sheet to future sea level changes a sound understanding about the processes within and beneath the ice sheet is required. However, due to the remoteness of the continent, persistent ice coverage and rough climatic conditions, obtaining observations and in-situ measurements is challenging and vast areas remain unsampled. Despite advances in observational technology and the employment of satellites to measure ice thickness, ice velocity, gravity and bedrock movement, large uncertainties remain in interpreting the signal and assessing the origin of the observed change. Satellites detect a general change in mass or height that can be derived from different causes. A change in mass that is observed by the Gravity Recovery And Climate Experiment (GRACE) mission can be induced by a change in surface mass or the distribution of mass within the Earth, primarily due to the viscoelastic response of the Earth's lithosphere due to glacial isostatic adjustment [Shepherd et al., 2012]. Satellite altimetry observations are additionally affected by surface height changes due to the compaction of snow, in addition to variations in ice mass and glacial isostatic adjustment. Even though models exist for ice sheet elevation and thickness [e.g. Monaghan and Bromwich, 2008], ice flow velocities [e.g. Rignot et al., 2008], bedrock elevation [e.g. Fretwell et al., 2013], glacial isostatic adjustment [e.g. Whitehouse et al., 2012; Ivins et al., 2013 Peltier et al., 2015] or regional climate models to simulate the Antarctic near-surface climate [e.g. Bromwich et al., 2011; Lenaerts et al., 2012], large uncertainties remain within the models due to the lack of observations across the AIS. This leads to uncertainties in accurately interpreting satellite observations, as the signals have to be assigned and allocated to the correct origin and observed changes need to be distinguished and separated to obtain the amount of change within the contributing cause.

To contribute to the understanding of Antarctic surface mass balance changes and the interpretation of satellite observations I have compared modelled surface mass balance and surface elevation changes with observations from GRACE and ICESat, respectively, with the motivation to contribute to the estimation of surface mass balance variations of polar ice sheets.

Consisting of four chapters, this thesis first provides background information and an overview of the AIS and the processes that have to be considered when studying ice mass balance, followed by an introduction about the satellite missions and the regional climate model deployed in my research.

To be able to correctly interpret altimetry measurements it is important to incorporate topographic changes due to the compaction of snow that occur within the firn layer that covers the AIS. Therefore, I developed my own firn compaction model that can be applied to my simulations on temporal elevation changes and I investigated the sensitivity of the model to small variations in the input values. This part of my research is covered in the third chapter

Finally I compared my modelled elevation changes in the firn layer with measurements from the ICESat mission to obtain an estimate of ice discharge values. Using my obtained estimates for ice discharge I then model temporal changes in mass and elevation to compare my modelled mass and height anomalies with observations from GRACE and ICESat. My method and results are described in the fourth chapter.

The thesis is completed with a concluding summary of my research in chapter five.

1.1 Antarctic Ice Sheet

The Antarctic continent is 99% covered by the world's largest body of ice – the Antarctic Ice Sheet (AIS). Located over the geographical South Pole, Antarctica is entirely surrounded by the Southern Ocean and has not been ice-free since the last ice age began around 34 million years ago [Steffen and Wu, 2011]. The AIS rises more than 1000 m above sea level for most of the continent, except coastal regions and ice shelves, and reaches a maximum thickness of over 4800 m in the Astrolabe Subglacial Basin [Fretwell et al., 2013]. Driven by internal deformation and sliding, the ice flows towards the coast [Bamber et al., 2000] where it flows into the ocean and forms large floating ice shelves [Ligtenberg, 2014]. Islands within these ice shelves are considered part of the continent, creating an immense surface area totalling ~14 million km^2 [Rémy and Frezzotti, 2006; Riffenburgh, 2006]. On top of the ice sheet a ~100 m thick firn layer is found, consisting of snow that has not melted and is slowly transformed to glacier ice through the process of densification [Ligtenberg, 2014]. Geographically, the continent is divided into the Antarctic Peninsula, West Antarctica and East Antarctica, separated by the Transantarctic Mountains (Figure 1.1). While the East Antarctic Ice Sheet (EAIS) is located on bedrock that is largely above sea level [Riffenburgh, 2006; Allison et al., 2009] the West Antarctic Ice Sheet (WAIS) is grounded on bedrock that is primarily below sea level, in places by more than 2000 m [Dalziel and Lawver, 2001; Allison et al., 2009; Fretwell et al., 2013]. Two large ice shelves are located between East and West Antarctica, the Ross Ice Shelf and the Filchner-Ronne Ice Shelf, each of an approximate size of 500,000 km^2 [Rignot et al., 2013], while several smaller ice shelves stretch along the coast.

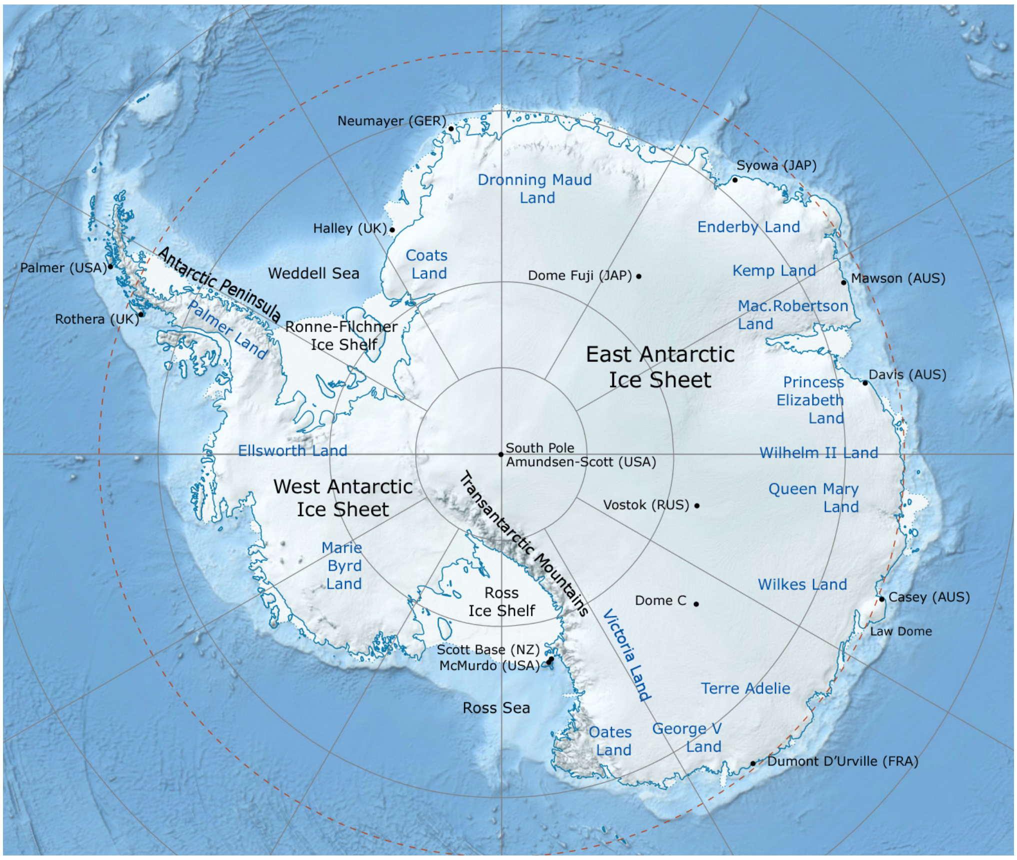

Figure 1.1: Overview of regions and locations across the Antarctic Ice Sheet [Haran et al., 2014; Scambos et al., 2007].

The climate of the AIS is strongly influenced by the surrounding Southern Ocean, the isolated location and size of the continent, and the terrain of the ice sheet. The average annual temperature across the ice sheet varies from approximately -60 degrees Celsius on the East Antarctic plateau to approximately -10 degrees Celsius near the ice sheet margins (Figure 1.2a). Although the major part of the AIS encounters sub-zero temperatures throughout the year, temperatures in coastal regions and on the Antarctic Peninsula can rise above zero degrees Celsius during warmer summer months. Due to such low temperatures, not much moisture is collected in the air above the ice sheet, creating a cold and dry climate. The highest snowfall rates can be observed at the Antarctic Peninsula and along the ice sheet margins, where more water vapour is collected in the air due to the surrounding ocean, while the interior does not receive much more snowfall than ~10 cm annually (Figure 1.2b), more often experiencing precipitation in form of diamond dust (ice crystals) [Schlosser et al., 2010].

The climate in Antarctica is strongly influenced by its surrounding atmospheric pressure systems and ocean currents; these include the Antarctic Circumpolar Current (ACC), the Antarctic Circumpolar Trough (ACT) and the Southern Annual Mode (SAM), also called the Antarctic Oscillation. Additionally, pressure systems such as Mean Sea Level Pressure (MSLP) and the El Niño Southern Oscillation (ENSO) also have an effect on climate patterns across the AIS. The ACC is an ocean current that surrounds the Antarctica circumpolar, consequently keeping warmer ocean water away from the continent and thus enabling the ice sheet. The ACT describes a belt of low pressure that surrounds the continent between 60°S and 65°S, encompassing variable westerlies. This zone mainly exists due to cyclones forming in the mid-latitudes and ending their southwards journey near the Antarctic coast. The expansion and contraction of the trough occurs twice a year, usually in March and September, and results in an ACT that is deeper and located farther south than usual [van den Broeke, 2007]. The SAM is an oscillation of the north-south location of the westerly wind belt featuring a temporal strengthening and weakening of the westerlies. A positive SAM indicates stronger than average circumpolar winds and weakens the katabatic wind over the EAIS, decreasing the downward mixing of warm air and thus cooling the surface in East Antarctica. The Antarctic Peninsula, on the other hand, experiences significant warming during a positive SAM [van den Broeke, 2007]. The atmospheric pressure taken at sea level is the MSLP, and is renowned to be closely related to changes in the SAM. Bromwich and Wang [2008] found that a high seasonal variability in MSLP in austral summer was consistent with a strong negative trend in the SAM. ENSO is the global-scale ocean-air interaction in the tropical western pacific (El Niño and La Niña) and a strong influence of ENSO on the Antarctic climate has been found [Sasgen et al., 2010; Fogt et al., 2010]. Transported by Rossby waves from the tropics towards the pole, it causes anomalies in the surrounding pressure system and changes in synoptic weather along the coast, primarily near the coast of West Antarctica [Monaghan and Bromwich, 2008; Sasgen et al., 2010; Boening et al., 2012]. Due to the ACT and cyclones, fierce storms regularly strike the continent, bringing warm moist air and precipitation towards the pole [Monaghan and Bromwich, 2008] and occasionally high precipitation events that occur only a few times per year but can bring up to 50% of the total annual accumulation [Schlosser et al., 2010]. Furthermore, the amount of water vapour in the atmosphere is additionally affected by the extent of sea ice, which varies from 4 million km^2 in summer to 19 million km^2 in winter, having a significant impact on seasonal atmosphere-ocean exchanges [Tietäväinen et al., 2008].

The topographic slope and the orientation of the AIS leads cold dense air to flow down the steep vertical slope of the plateau, significantly contribute to the distribution of surface mass, positively (deposition) and negatively (erosion) (Figure 1.2c) [Lenaerts and van den Broeke, 2012]. This is known as katabatic wind. Scarchilli et al. [2010] found that strong winds can easily displace suspended snow, with a thickness of 200 m, a few kilometres downwind and that frequently up to 50% of precipitation is removed and relocated.

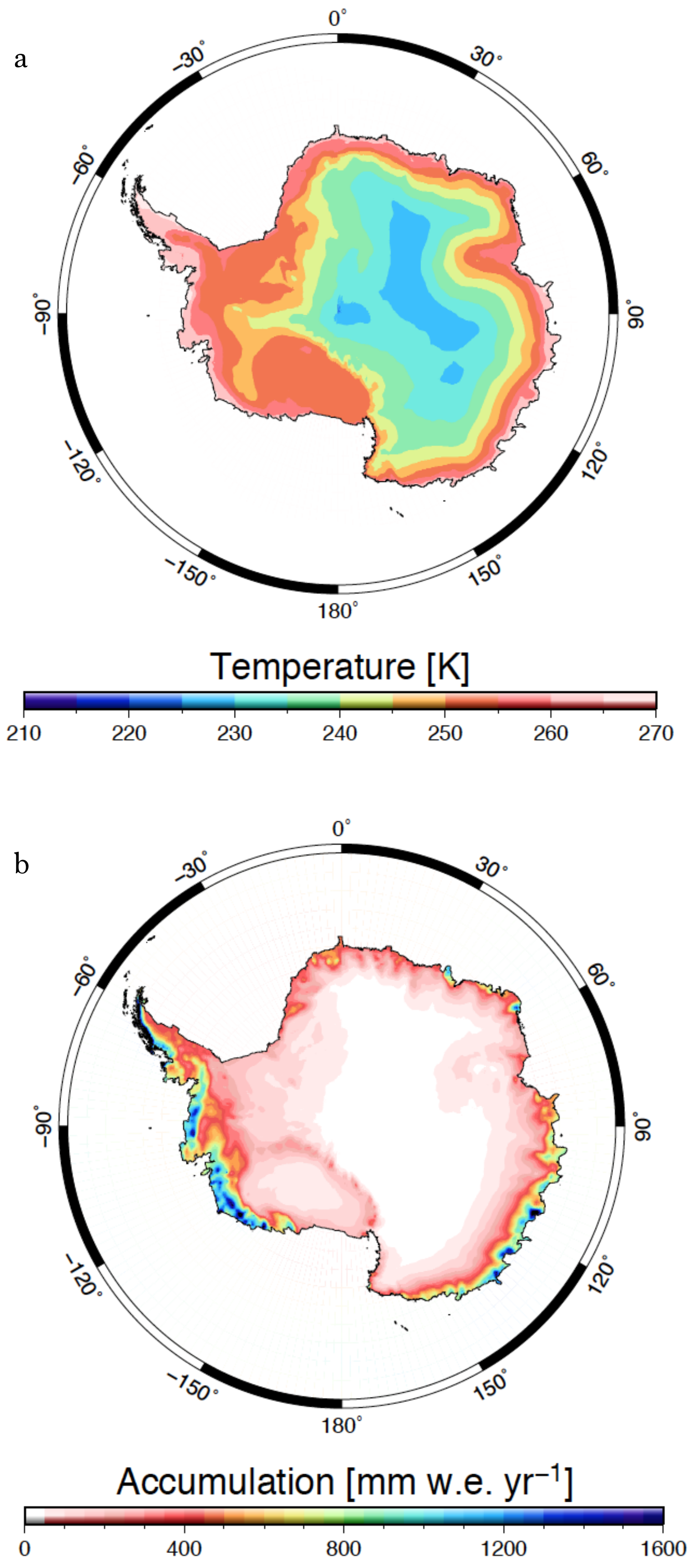

Figure 1.2a-b: Spatial distribution of the (a) average annual temperature and (b) accumulation, as provided by the regional climate model RACMO2/ANT.

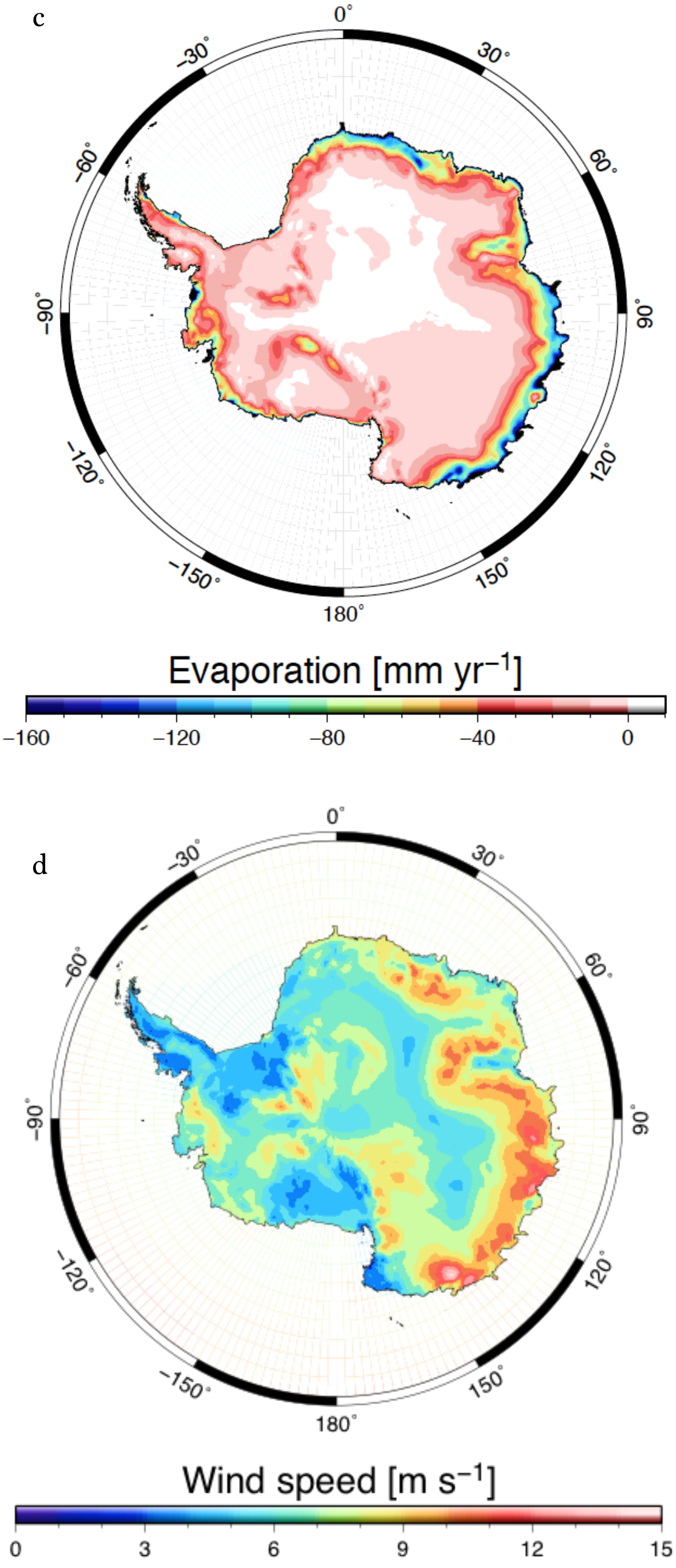

Figure 1.2c-d: Spatial distribution of (c) all sublimation and deposition processes combined (evaporation), positive is mass loss, negative is mass gain, and (d) average annual wind speed at 10 m above the surface, as provided by RACMO2/ANT.

The maximum snow transport occurs during autumn and winter [Parish and Bromwich, 2006] and is usually transported into the atmosphere [Scarchilli et al., 2010]. Drifting snow interacts with the atmosphere by increasing the lower atmosphere moisture content, thus leading to increased snowfall in regions where the atmosphere usually contains little moisture [Lenaerts and van den Broeke, 2012]. Locally, drifting snow erosion and deposition have a significant impact on snow mass variations and need to be included in surface mass balance estimates (Figure 1.2d) [Lenaerts and van den Broeke, 2012].

1.2 Ice sheet mass balance

The amount of ice within a glacier or ice sheet varies over time and is controlled by the processes that contribute to mass gain and mass loss of the ice body. The difference between the mass that is added and removed is referred to as the ice sheet mass balance and is positive if mass input exceeds output and negative if reversed. Determining variations in ice mass balance is of great interest to understand its possible effects on global sea level changes as a negative mass balance contributes to global sea level rise.

The term “surface mass balance” describes all processes that are collectively known as mass exchanges, generally referred to as accumulation and ablation processes [Cuffey and Paterson, 2010]. The term “accumulation” includes all mechanism where snow and ice is added to the ice sheet, and represents the mass input for the AIS. Due to the higher water vapour content in the atmosphere, snowfall usually occurs near the coastline in Antarctica and only occasionally in the interior. In vast areas of the AIS, freshly accumulated snow is often redistributed by the strong katabatic winds, playing an important role in mass exchanges. Regions that are subject to snow blowing distributions are created due to the interaction between topography and the wind. Snow depositions are generally found along regional slopes, nunataks and crevasses, or hollows that are filled up with wind-transported snow [Cuffey and Paterson, 2010], while zones of exposed blue-ice are often found on the leeward side of nunataks [Ligtenberg et al., 2014]. In Antarctica, zones of exposed blue ice are formed in regions where ablation exceeds accumulation and ~1 % of the EAIS is covered by wind-induced (e.g. Byrd Glacier) and melt-induced (e.g. Lambert Glacier and Amery Ice Shelf) blue ice areas [van den Broeke et al., 2006; Ligtenberg et al., 2014].

Ablation processes include the discharge of snow and ice due to ice melting, both at the surface and at the glacier base, and erosion and sublimation (the direct transition from solid to gas without entering the liquid phase) on the surface. In a cold environment like Antarctica, sublimation is the dominant ablation mechanism, favoured by dry air and strong winds [Cuffey and Paterson, 2010]. While sublimation occurs year-round in some parts of Antarctica (e.g. Dry Valleys [Fountain et al., 2006]), in other regions short ablation periods during summer are usually interrupted by returning cooling events and/or snowfall. Melt streams form in regions where temperatures occasionally reach the melting point. However, not all of the meltwater drains, but refreezes, either on the surface, percolated within a cold snow or firn layer, or within fractures and crevasses [Cuffey and Paterson, 2010].

The primary mechanism of mass output of the AIS is by ice discharge into the surrounding ocean as the ice sheet passes the grounding line (boundary between grounded and floating ice) and forms floating ice shelves. This leads to iceberg calving and basal melting at the bottom of the floating ice shelves [Zwally et al., 2002; Cuffey and Paterson, 2010]. The rate at which these processes contribute to the mass balance of the entire ice sheet over a period of time, determine the change of total mass.

To emphasise the contribution of the accumulation and ablation processes, surface mass balance (SMB) can be written as:

$$\mathrm{SMB} = A - S - W_E + W_D - M_{Ru}, \tag{1.1}$$

Where A represents accumulation, S sublimation, W_E and W_D wind erosion and wind deposition of surface snow, respectively, and M_{Ru} meltwater runoff. All terms represent a change in mass and are given in kg m^{-2} yr^{-1}. The distribution of snow by wind is negative where it erodes and positive where it deposits. As the snow is primarily distributed across the ice sheet, drifting snow erosion can be neglected on a continental scale but is found to significantly affect local SMB changes [Lenaerts and van den Broeke, 2012]. Sublimation can also be either positive or negative as sublimation usually exceeds depositions due to water vapour [Cuffey and Paterson, 2010]. Although the process of meltwater runoff is small in Antarctica since most of the meltwater refreezes locally, it cannot be neglected, as meltwater runoff occasionally occurs in some parts of the AIS. To obtain the overall change in mass balance (MB) the volume of ice discharge (D) over the grounding line has to be subtracted from the surface mass balance:

$$MB = SMB - D. \tag{1.2}$$

1.3 Firn

Firn is the material that composes the intermediate product between snow and ice. Usually the term “snow” is restricted to the material that has not changed since it fell and still has its initial density [Cuffey and Paterson, 2010]. In Antarctica the density of fresh snow is typically ~350 kg m^{-3}, but can vary between 300 kg m^{-3} in the cold interior and up to 450 kg m^{-3} along the coastline [Helsen et al., 2008b; Ligtenberg et al., 2011]. Due to cold temperatures and nonexistent regular snowmelt events in Antarctica, surface snow is constantly buried during precipitation events, constantly increasing surface loads. Once fresh snow is deposited, different stages of densification are passed before it reaches the state of dense glacier ice. The densification process is highly dependent on accumulation rate and temperature and is commonly referred to as “firn compaction” [Cuffey and Paterson, 2010; Arthern et al., 2010; Ligtenberg et al., 2011]. During the compaction, air is removed and snow crystals are compressed, deformed and repositioned. As a result, the density changes with depth, overburden pressure and temperature, and increases until the density of ice (approximately 917 kg m^{-3}) is reached [Herron and Langway, 1980; Cuffey and Paterson, 2010]. Through this process the firn layer compacts, reducing its thickness and thus the elevation of the ice sheet. This is an important factor when measuring ice surface heights, as the thickness of the firn layer constantly changes, and surface elevation changes may be due to the densification of the firn layer rather than mass loss [e.g. Li and Zwally, 2004; Riva et al., 2009; Li and Zwally, 2010].

Within the transformation process, Herron and Langway [1980] identified three stages of densification with the fastest densification rate in the first stage; here the dominant mechanism is packing, settling and re-arranging of snow grains. After reaching a density of about 550 kg m^{-3} densification slows down significantly and compaction occurs mainly due to material transfer by sublimation, diffusion and deformation processes. This stage continues until the pore close-off depth is reached and air bubbles are trapped within the ice, usually at a density of approximately 830 kg m^{-3}. In the last stage, remaining air bubbles undergo further compression until the density of glacier ice, ~917 kg m^{-3}, is reached [Herron and Langway, 1980; Ligtenberg et al., 2011]. In regions where surface temperatures occasionally climb above freezing, meltwater will occur and can penetrate into the firn layer. During such events, water percolates down through the firn layer, filling up the air pores and will partly remain attached to snow crystals. Once the meltwater reaches a layer with temperatures below zero it will refreeze, replace available air space with ice and efficiently compact this layer [Ligtenberg, 2014].

Due to the differences in snow consistency (dry or wet), accumulation rate and temperature variations, the depth and time it takes for snow to turn into ice varies. Commonly, transition depth and time is greatest in extremely cold regions with low accumulation rates, while more temperate regions with high accumulation rates show a much shorter transformation time [Cuffey and Patterson, 2010]. Therefore, while the firn-ice transition on a glacier in the European Alps can be found at a depth of 32 metres, correlating to an age of 13 years [Vallon et al., 1976 found in Cuffey and Paterson, 2010], it takes around 280 years at Byrd in West Antarctica with a transition depth of 64 metres. Even more impressive is the area around Vostok, with temperatures around 30°C colder than Byrd and with less accumulation. Here the transition is found at a depth of 95 metres, corresponding to a time of 2500 years [Cuffey and Paterson, 2010].

The general physics of firn densification is complex and still not fully understood. Components such as grain settling, re-crystallisation and diffusion have not been fully analysed [Herron and Langway, 1980] and observations are mainly obtained by laboratory experiments with some in-situ measurements [e.g. Li and Zwally, 2004; Arthern et al., 2010]. Moreover, the process of meltwater percolation and refreezing within a firn layer has to be considered, as the refreezing of meltwater results in layers with higher densities and possibly creations of complete ice lenses [Ligtenberg et al., 2011]. While some models consider melting of the top layer and refreezing within the annual snow layer [Li and Zwally, 2011; Helsen et al., 2008; Li and Zwally, 2011] or firn column [Ligtenberg et al., 2011; Simonsen et al., 2013], other studies incorporate the refreezing of meltwater in the form of ice lenses [Reeh, 2008; Sørensen, 2011]. A more precise representation is not yet possible, as the effect of percolating meltwater is not known in more detail.

Due to the complexity of firn densification, assumptions on surface mass, stress, temperature and density are made to simplify the models that describe the processes within the densification stage. Any advanced model is still based on descriptions of physical processes that govern densification, and models still rely on empirical calibrations with considerable uncertainties, especially in time-dependent simulations [Reeh, 2008]. Therefore there is no universal physical model for predicting densification rates in the firn column [Li and Zwally, 2004; Arthern et al., 2010]. Semi-empirical densification models [e.g. Herron and Langway, 1980; Arthern and Wingham, 1998; Ligtenberg et al., 2011; Simonsen et al., 2013] and physically based models [e.g. Zwally and Li, 2002; Reeh, 2005; Helsen et al., 2008], which cope with the different densification processes, have been developed. These models include adjustable rate coefficients to match ice core profiles or laboratory experiments [e.g. Zwally and Li, 2002; Helsen et al., 2008; Arthern et al., 2010; Ligtenberg et al., 2011; Simonsen et al., 2013]. While those models agree fairly well with selected field observations and firn core data, every model predicts different sensitivities to the physical conditions of density temperature, accumulation, grain-size and overlying snow weight [Arthern et al., 2010]. Ice core samples and snow-pits can reveal density profiles as a function of depth, and investigations have parameterised density-depth profiles in terms of accumulation rate, mean annual surface air temperature and deposition density at the surface [Arthern et al., 2010]. Since these profiles do not provide information about the compaction rate, a steady-state situation is often assumed in order to estimate the firn compaction, with the attempt to establish time-dependent models [e.g. Zwally and Li, 2002; Reeh, 2008; Li and Zwally, 2011; Ligtenberg et al., 2011]. A detailed description of firn densification models of the AIS can be found in Chapter 3.

1.4 Glacial isostatic adjustment

The Earth's lithosphere and mantle react elastically and viscoelastically to surface loads and adjusts when the load is added or removed. The initial response of the lithosphere is elastic and instantaneous until the weight is removed. Should the load have remained for hundreds or even thousands of years, the deformation of the lithosphere slowly continues viscoelastically by depressing into the mantle, displacing the viscous mantle material beneath, and thus uplifting the lithosphere, the forebulge, in front of the load [Wahr et al., 1995; Allison et al., 2009]. In regions where large ice sheets once covered the continent, such as the Laurentide ice sheet in North America or the Fennoscandia ice sheet in Scandinavia, the bedrock has been found to undergo significant changes since the ice sheets have vanished. After the surface load is removed, the lithosphere adjusts to the reduced weight by rebounding, initially in the form of a quick elastic response (instantaneously), followed by a slow viscoelastic rebound over hundreds to thousands of years, accompanied by the subsidence of the forebulge region. Due to the slow relaxation of the Earth's mantle the process of isostatic adjustment is still ongoing and apparent today [e.g. Steffen and Wu, 2011].

After the Last Glacial Maximum (LGM) about 20,000 - 14,000 years ago, large ice sheets began to disappear and the size of the polar ice caps declined [Clark et al, 2009]. During the ongoing transfer of water-mass between the oceans and the ice sheets, the lithosphere continuously deformed because of the changing water load [Steffen and Wu, 2011]. Since the LGM, the AIS retreated and the adjustment of the bedrock beneath the current ice cover is an ongoing process [Wahr et al., 1995; Steffen and Wu, 2011].

There are several possibilities for observing and estimating Glacial Isostatic Adjustment (GIA) rates. Fennoscandia is described as the key area for GIA research due to its long settlement history with an early start of scientific investigations that commenced in the late 17th century [Steffen and Wu, 2011]. To study present-day GIA rates, observations of relative sea level, tide-gauges, shoreline tilting, geomorphology, as well as GPS and gravity measurements are used, to provide information about crustal movements [e.g. Whitehouse et al., 2012a,b; Peltier et al., 2015]. To cover a time period that can be dated back to several thousand years it is necessary to look at relative sea level (RSL) observations that indicate a rise or fall in any particular coastal area since the LGM. The magnitude of RSL movement is governed by changes in ocean water volume, isostasy in reaction to mass redistribution, and tectonic uplift or subsidence of the Earth's crust, and varies with distance from the former ice sheet. Surface-pressure is greatest in the centre of an ice sheet, hence, the isostatic component is largest in that area and gradually decreases towards the former ice edges, being negative outside the ice sheet and over the oceans and small but positive for far-field continents [e.g. Johnston and Lambeck, 1999].

Field observations on GIA uplift rates can be found all over Scandinavia and North America, in the form of sea-level marks, tide gauges or by gravimetric or bedrock movement surveillance. However, observations of ongoing isostasy rates in Antarctica are extremely limited due to the extensive ice coverage that still exists across the continent. In ice-free regions around Antarctica raised beaches, former shorelines and sea-level reconstructions derived from radiocarbon dating of organic material as well as dating of sedimentary transitions collected from sedimentary cores have been studied to obtain relative sea level variations [e.g. Zwartz et al., 1998; Nakada et al., 2000]. Established ice models are based on observations where possible, but are strongly affected by the paucity of observations and large uncertainties about the previous ice extent of the AIS. There are different assumptions on past ice volumes in the reconstruction of the ice sheet: growth and ablation rates, ice mechanics and extent of the bedrock depression beneath the ice load [Nakada and Lambeck, 1988]. Due to the insufficient observations that can be found around Antarctica, relative sea-level information is commonly used from far-field sites such as Barbados or Tahiti [e.g. Whitehouse and Bradley, 2013] to study global sea-level changes. Generally the models are based on global relative sea-level observations, suggesting an universal ice sheet history of the Late Pleistocene Antarctic and Arctic ice sheet [e.g. Nakada and Lambeck, 1988; Nakada et al., 2000] as well as the Laurentide and Fennoscandia ice sheets [e.g. Peltier, 2002; Peltier, 2004], respectively, and are supported by additional observations in and near Antarctica where available [e.g. Whitehouse et al., 2012a; Ivins et al., 2013; Argus et al., 2014].

The timing of melting events and the contribution of individual ice sheets to sea level needs to be estimated to allocate ice sheet melting history and relative sea level observations. Therefore, ice sheets that covered the continents during the Late Pleistocene and Holocene have to be reconstructed in their extent and thickness. The prediction of uplift rates in GIA models strongly depends on the ice history used and the underlying Earth rheology model. While there is general agreement amongst scientists that the Antarctic ice cover during the LGM was more extensive than it is at present, it is not agreed to what extent [Ivins and James, 2005]. Nakada and Lambeck [1988, 1989] established three Arctic and four Antarctic models, respectively, to construct a correlation between modelled and observed sea-level changes, each model differs in ice volume, timing of melting and its contribution to sea-level. More recently, Nakada et al. [2000] updated the models by comparing field observations and modelling results, constraining a maximum (ANT5) and minimum (ANT6) ice-loading history model of the AIS.

The ICE-“NG” models by Peltier [e.g. Peltier, 2002; Peltier, 2004; Argus et al., 2014; Peltier et al., 2015] are primarily based on radiocarbon-dated sea-level histories, which provide constraints on mantle viscosity and deglaciation history for the past 10,000 calendar years [Peltier, 2004]. The ICE-NG series of models started as ICE-1G in 1976 [Peltier and Andrews, 1976] and have been updated and improved with growing knowledge. The latest version is the ICE-6G_C (VM5a) [Argus et al., 2014], where ICE-6G represents the deglaciation model and VM5 the viscoelastic model that is used to represent the Earth’s rheology. The new ICE-6G_C model is a revised version of the former ICE-5G (VM2) model and represents the deglaciation events of the last ice age [Peltier et al., 2015]. Not only has the model been constrained to conform to available geological observations of ice thickness changes obtained from exposure-age dating, relative sea level histories and the age of the onset of marine sedimentation from radiocarbon dating, it has also been explicitly refined to apply and match available GPS measurements of vertical bedrock motion [Argus et al., 2014]. To enhance the ICE-6G_C for Antarctica, observations of vertical and horizontal crustal movement of 59 GPS sites in Antarctica were used and the ice thickness is adjusted to enable the model to fit GPS uplift rates, ice thickness change data and sea level histories. The model is found to fit the totality of these data well [Argus et al., 2014].

In 2005 Ivins and James [2005] developed the IJ05 model to provide a GIA model for Antarctica. Their model is based on radiocarbon dating, marine records, sedimentary core data, as well as moraine and lacustrine data of ice-free exposures, and both bathymetric and seismic mapping, respectively. Compared to the ICE-5G model, the IJ05 predicts a substantially smaller meltwater input into the oceans (65% less volume than the ICE-5G model), assuming that more meltwater had been contributed from other ice sheets. Furthermore, they used a different forward model to predict vertical crustal velocities, strongly depending on mantle creep strength or mantle viscosity [Ivins and James, 2005]. Ivins and James [2013] have improved their IJ05 model to develop IJ05_R2 by incorporating new datasets that have become available: a substantially improved set of geological and ice core data, and GPS vertical motion observations.

Prior to this, Whitehouse et al. [2012a,b] developed a new deglaciation model and GIA model for Antarctica, likewise building upon the work of Ivins and James [2005]. Beside the widely available datasets of marine and terrestrial geological and geophysical observations, and recently introduced past ice sheet extent studies from multibeam (swath) bathymetry, they have synthesised the existing data and combined them with a numerical ice-sheet model to reconstruct the AIS at different time steps [Whitehouse et al., 2012a]. The result of their approach is a new deglaciation model, W12, (and W12a, an adjusted version of the initial model to fit GPS observations across the Antarctic Peninsula) that presents an estimate for the ice sheet volume at the LGM being lower than previous studies and an improved GIA model that fits relative sea level data and GPS observations. The outcomes of the improved deglaciation models (W12 and IJ05_R2) result in a smaller GIA correction, directly affecting ice sheet mass balance estimates by a difference of ~70 Gt/yr (shown in Table 1.2) [Velicogna and Wahr, 2013].

While the latest versions of the described GIA models significantly improved the reconstruction of the AIS history, attempts have been made to subtract uplift rates and ice mass balance changes derived from satellite observations. Riva et al. [2009] published a present-day GIA model derived from using a hybrid ice-firn surface density model to estimate mass changes from altimetry, and combined these observations with GRACE observations of mass change (Chapter 2, Section 2.1) to separate GIA from surface processes. Under the assumption of a bottom (rock) and a top (ice/firn) layer of different densities and thickness, they modelled GIA uplift rates as:

$$H_{GIA} = (M_{GRACE} - \rho_{surf})\ H_{ICESat} / (\rho_{rock} - \rho_{surf}) \tag{1.3}$$

where H_{GIA} describes the variation in bedrock topography, M_{GRACE} and H_{ICESat} represent the mass change and elevation changes as observed by GRACE and ICESat (Chapter 2, Section 2.1 and 2.2), accordingly, and ρ_{rock} and ρ_{surf} the average density of the rock and surface layers, respectively [Riva et al., 2009; Gunter et al., 2014]. Their model results are in good agreement with the IJ05 model and glaciological models [e.g. Huybrecht, 2002] but differed significantly from the ICE-5G model [Riva et al., 2009].

Gunter et al. [2014] recently revisited the approach by Riva et al. [2009], by including a firn densification model and SMB estimates, with the aim to account for surface mass processes:

$$H_{GIA} = M_{GRACE} - [(H_{ICESat} - H_{Firn})\ \rho_a + M_{Firn}] / (\rho_{rock} - \rho_a) \tag{1.4}$$

with H_{Firn} and M_{Firn} representing changes in height and mass due to firn compaction, and where the density ρ_a varies between 917 kg m^{-3}, when $(H_{ICESat} - H_{Firn}) < 0$ and $| H_{ICESat} - H_{Firn}| > 2\sigma_h$, and the density difference between ice/snow, when $(H_{ICESat} - H_{Firn}) > 0$ and $| H_{ICESat} - H_{Firn}| > 2\sigma_h$. σ_h represents the uncertainty of the height estimates, which is derived from the firn compaction and the altimetry data set:

$$\sigma_h = \sqrt{\sigma_{ICESat}^2 + \sigma_{Firn}^2}\ , \tag{1.5}$$

with the uncertainty in the ICESat observations, σ_{ICESat}, and in the firn densification model, σ_{Firn}, respectively [Gunter et al., 2014]. The results for the GIA estimates show a general agreement with the IJ05 and W12a models, showing a slight subsidence in East Antarctica, and uplift in West Antarctica, namely between the Ross and Filchner Ronne Ice Shelf. Additionally, the overall estimate of ice mass changes are similar to results of Shepherd et al. [2012], King et al. [2012] and Sasgen et al. [2013].

In 2002, before the launch of the GRACE satellites, Velicogna and Wahr [2002] presented simulated results for a method to separate Antarctic GIA and ice mass balance using GRACE and altimetry data. By simulating GRACE and ICESat data they obtained a root-mean square accuracy of 5.3 mm yr^{-1} for GIA and 19.9 mm yr^{-1} for MB. They mentioned that their largest source of error within the combined signal is the effect of unknown mass of accumulation and firn density, which is why they added GPS measurements as additional constraints. Their technique was based on recovering spatial variability of ice mass trend and GIA signals to initially solve for SMB and GIA before adding GPS measurements of vertical velocities to solve for firn densities.

Using an analogous iterative approach as described by Wahr et al. [2000], ICESat data alone can be used to determine ice mass changes. These data are assumed to be only sensitive to ice thickness changes and have not been corrected for firn densification and GIA, as SMB estimates would be contaminated regardless, due to model uncertainties [Wahr et al., 2000; Velicogna and Wahr, 2002]. The MB estimate from ICESat is used to calculate the rate of change in the geoid and is removed from the GRACE data. The remaining change in the geoid from the GRACE data is interpreted as GIA signal, which is subsequently removed from the ICESat observations. That process is repeated to obtain a better SMB estimate [Wahr et al., 2000] until the improvement is negligible [Velicogna and Wahr, 2002]. According to Velicogna and Wahr [2002] using two observables to determine three unknowns is the limiting error in the SMB recovery. To overcome this issue they added GPS point measurements of vertical velocity by estimating GIA from the difference between GPS velocities and computed GIA estimates. This step is applied to the last iteration of the GRACE/ICESat estimate and the thereupon obtained GIA error is used to estimate firn compaction trends, which subsequently can be used to correct the SMB estimations. In spite of their simulations being successful, their approach has not been presented with real data from actual GRACE and ICESat observations.

Table 1.1: Approximate present-day uplift rates for various locations across Antarctica in [mm yr^{-1}] as modelled by the GIA models described in the text. The data is taken from Figure 14 in Whitehouse et al. [2012], Figure 4 and 5 in Ivins and James [2013] and Figure 6 in Argus et al. [2014].

GIA model	South Pole	Mawson	Dumont D'Urville	Edward VII Land	Palmer Land	General Belgrano II
ICE-5G (Peltier)	3.7	3.3	0.5	5	7	2.4
IJ05_R2 (Ivins and James)	0	1	1	2	2.5	1.5
W12a (Whitehouse et al.)	0	1	1.4	4	0.5	0.5
ICE-6G (Peltier)	0	3	1.2	5	5	3

1.5 Antarctic Ice Sheet mass balance estimates

There are different techniques used to evaluate ice mass balance: measuring the change in mass, the change in volume, which is subsequently converted to a change in mass through firn density, and the mass budget method (MBM).

The gravimetric method is based on direct observations from the Gravity Recovery And Climate Experiment (GRACE) satellite mission, which monitors the Earth's gravity field. Mass changes within the ice sheet directly affect spatial and temporal changes in the regional gravitational field and are therefore detected by GRACE. Besides changes in ice mass it is also necessary to correct for other possible mass variations, such as ocean tides and the deformation of the Earth's crust as a response to prolonged ice loads (GIA). A more comprehensive description of the GRACE space mission, observations and the method to estimate ice sheet mass balance can be found in Chapter 2, Section 2.1.

The second method is based on using satellite altimetry to monitor temporal surface elevation changes of an ice sheet by measuring the distance between the ice surface and the satellite. A change in height can be related to a change in the volume of an ice sheet which, subsequently, can be converted into a change in ice mass if the density is known. However, surface elevation is also affected by the densification process of snow and glacial isostatic adjustment, therefore, models have to be applied to correct for both processes. This method, together with a comprehensive explanation about satellite altimetry missions and converting altimetry observations to mass changes, is described in more detail in Chapter 2, Section 2.2.

In the mass budget method the amount of accumulation, ablation and dynamic ice loss is determined individually. The difference between the sum of mass input and mass output is the mass balance of the ice sheet [e.g. Rignot, 2002; Rignot et al., 2008; Allison et al., 2009]. The main contribution to mass input in Antarctica is snowfall, which can be estimated using in-situ measurements (short-term records) or snow pits and ice core observations (long-term records). However, these methods only cover a few locations scattered across the AIS and interpolation methods such as microwave readings using satellites [Arthern et al., 2006] have to be used to fill in the gaps. More commonly used are regional atmospheric climate models that simulate near surface climate patterns across the entire ice sheet [e.g. van de Berg, et al., 2006, Lenaerts et al., 2012]. The quantity of mass output is determined by the amount of ice that discharges across the grounding-line, which can be assessed by measuring the velocity of ice flow and the ice thickness at the grounding line [e.g. Rignot, 2002]. To obtain ice velocities, interferometric synthetic aperture radar (InSAR) satellite images are used, while the ice thickness can be estimated either by using ice penetrating radar or is derived from the location of the actual grounding line [Rignot et al., 2011; Ligtenberg, 2014]. The map of ice velocities across Antarctica has been updated by Rignot et al. [2008], presenting a nearly complete map from InSAR data collected between 1992-2006 using ERS-1/2, Radarsat-1 and Japanese Advanced Land Observation Satellites. Ice velocities are presented with a precision of 5-50 m yr^{-1} and short-time variations are averaged out. The grounding line of the glaciers is mapped with a precision of 100 m all around Antarctica, derived from surface elevation under the assumption that ice is in hydrostatic equilibrium with seawater. The SMB is determined using RACMO2/ANT and averaged for the period 1980-2004 and is compared to ice flux for each glacier [Rignot et al., 2008]. In general, ice dynamics are not well known and it has been pointed out by Rignot et al. [2008] that mass budget is more complex than previously indicated and that changes in glacier dynamics may dominate ice sheet mass budget.

Another approach that has been applied to estimate present-day surface mass trends and GIA in polar regions is to combine GRACE observations with Ocean Bottom Pressure (OBP) and GPS measurements [Wu et al., 2010]. A simultaneous global inversion of derived linear trends from GRACE and OBP records, combined with surface velocities of globally distributed GPS sites is used to separate global surface mass and GIA in geodetic data. This is done by combining the geodetic data with a priori information on GIA dynamics and the spatial extent of deglaciation from glaciological and geological data [Wu et al., 2010].

Recent estimates of AIS balance vary from -69 ± 18 Gt yr^{-1} [King et al., 2012] to -147 ± 80 Gt yr^{-1} [Velicogna and Wahr, 2013] and are shown in detail in Figure 1.3. The reason for such inconsistency in estimates is largely associated with the dataset used (GRACE, altimetry, MBM) and the GIA model employed (Section 1.4). Despite such large uncertainties, there is a general consensus that overall the AIS is losing mass, a process that is likely to accelerate in the future should global temperatures continue to rise.

The overall MB estimate of the AIS is based on mass balance changes within the EAIS, the WAIS and the Antarctic Peninsula. While the MB estimates for the WAIS and the Antarctic Peninsula are well documented, large uncertainties exist for the EAIS. This is mainly due to the size and remoteness of the EAIS, with the lack of observations leading to poorly constrained geophysical models that are needed to reconstruct ice sheet and bedrock dynamics. Recent estimates for the EAIS suggest a positive mass balance as a result of positive mass and elevation anomalies detected by GRACE and altimetry (e.g. King et al., 2012; Shepherd et al., 2012; Sasgen et al., 2013; William et al., 2014). Contrarily, the WAIS (including the Antarctic Peninsula) is losing mass at a rate of -64 to -159 Gt yr^{-1} (Fig. 1.3), mainly attributed to the rapid loss around the Amundsen Sea coast [King et al., 2012]. As mentioned previously and as shown by Velicogna and Wahr [2013], SMB estimates strongly depend on the GIA model that is used to correct for bedrock movements rates. By introducing new regional ice deglaciation models (Section 1.4) that are adjusted to match a range of glaciological, geophysical and geologic observations, the estimated ice mass loss for Antarctica of -83 ± 49 Gt yr^{-1}, using the IJ05_R2 model, is less negative than when using the ICE-5G model [Velicogna and Wahr, 2013].

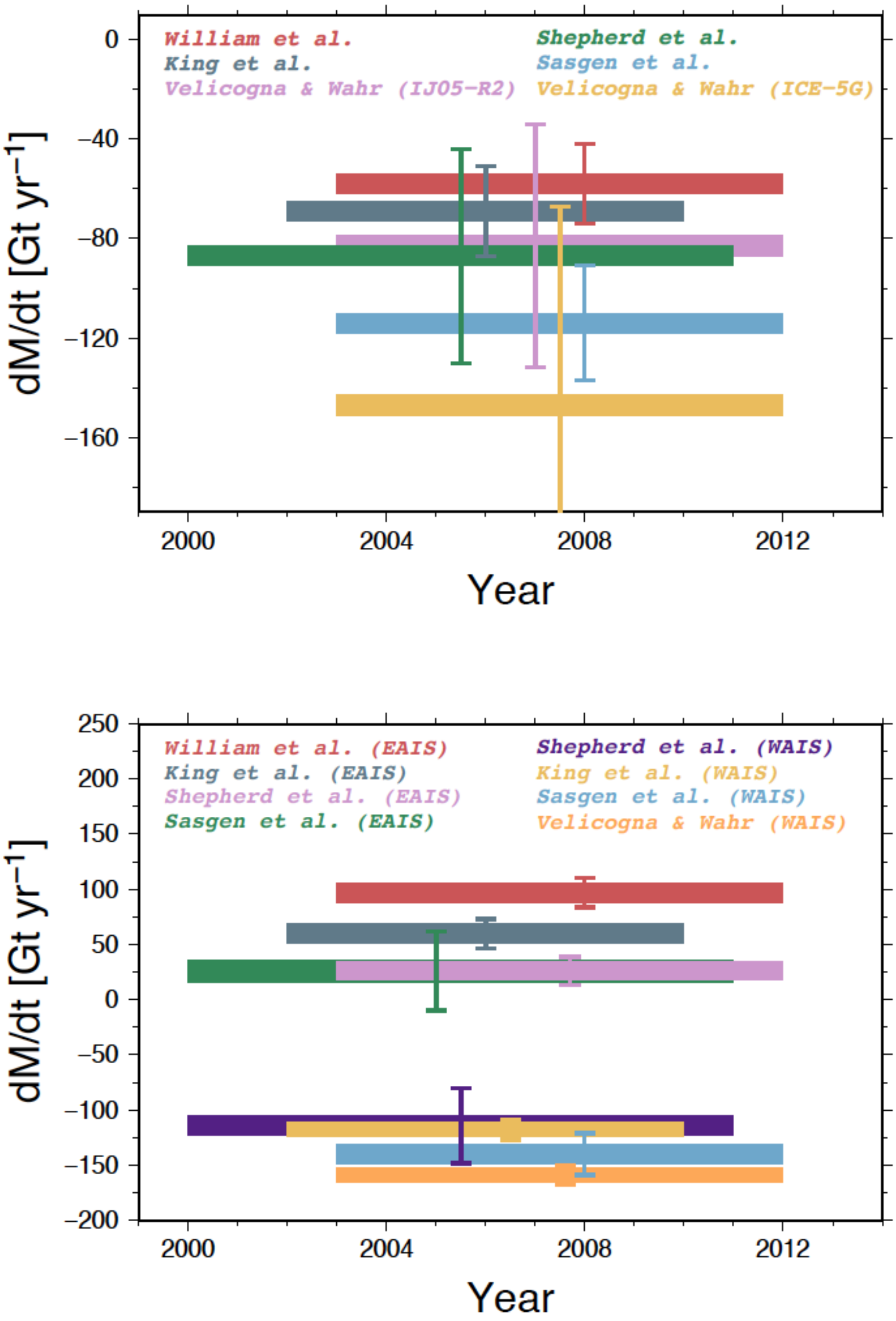

Figure 1.3a-b: Comparison of recent mass balance estimates for the AIS based on different studies and methods. a) illustrates the overall AIS mass balance and b) separates the EAIS and WAIS. Velicogna and Wahr [2013], King et al. [2012], Sasgen et al. [2013] and William et al. [2012] all use GRACE observations but employ different GIA models (ICE-5G and IJ05-R2, W12a, AGE-1b and W12a, respectively), while Shepherd et al. [2013] combined GRACE, altimetry and the mass budget method. Not all studies include individual estimates for the EAIS and WAIS.

Chapter 2

Satellite missions

2 Introduction

In recent years satellite missions have significantly contributed to and improved our understanding and knowledge of temporal and spatial variations of the Earth's atmosphere and climate, the Earth's gravity field and surface elevation. Satellites orbiting the Earth on repeat cycles help us to monitor changes that occur over time. Due to the limitation of conducting fieldwork in remote areas, scientific satellite observations in polar regions have increased our understanding on present-day ice mass variations across the polar ice sheets, providing new insights into climatic and atmospheric fluctuations near the poles, ice sheet mass balance, ice thickness and glacial isostatic adjustment.

The primary satellite missions to study changes of the polar ice sheets are the Gravity Recovery And Climate Experiment (GRACE) mission to measure variations within the Earth's gravity field, and satellite altimetry (e.g. ENVISAT, ICESat, CryoSat-2) to obtain time-series of surface elevation changes. Additionally, GPS measurements are used to detect vertical bedrock movements of the lithosphere beneath the AIS to observe the elastic and viscoelastic response of the Earth's crust.

However, there are still a number of limitations associated with satellite observations, specifically in identifying the origin of the observed signal. Gravity, altimetry and GPS observations need to be separated into components related to ice sheet mass balance variations and glacial isostatic adjustment. Altimetry observations are further sensitive to changes caused by the compaction of firn, as this leads to a reduction of the firn layer thickness that covers the ice sheet, and detected elevation changes need to be corrected for the compaction rate. This chapter focuses on the satellite missions that are used in this thesis to study present-day surface mass balance and bedrock uplift rates as monitored by the satellites. It furthermore provides a description of the regional climate model RACMO2.1, that is used to model mass and height anomalies, which are compared with gravity and altimetry observations from the GRACE and ICESat mission, respectively.

2.1 GRACE - The Gravity Recovery And Climate Experiment

The Gravity Recovery And Climate Experiment (GRACE) space mission was launched in 2002 to monitor temporal mass variations in the Earth system. It is a joint mission by NASA and the German Aerospace Centre (DLR – Deutsches Zentrum fuer Luft und Raumfahrt) and was designed to operate for five years [Tapley et al., 2004]. Currently, GRACE operates in an extended mission phase, which will hopefully continue through to 2017 when the follow-up mission is planned to be launched. Due to the fact that, even 12 years later, the GRACE satellites still provide global maps of the Earth's gravity field, the gravity experiment is one of the most successful space missions. However, battery life as well as fuel availability on GRACE A are now important issues and operation times are reduced during eclipse seasons to maximise the remaining lifetime [Kruizinga and Williams, 2015].

2.1.1. Mission overview

The GRACE mission consists of two identical satellites originally orbiting the Earth at an altitude of ~450 km (~400 km nowadays). The twin satellites are in a tandem orbit and are separated by ~200 km, circling the Earth and mapping the entire globe to measure minor variations in the Earth's gravitational field [Tapley et al., 2004]. The spatial resolution at which GRACE can map the global gravity field is 400 km to 40,000 km [Tapley et al., 2004]. Measurements of mass anomalies are made by the gravitational influence on the satellites causing a change in the distance between the two satellites. A very sensitive K/Ka-band microwave ranging system measures these fluctuations in the along-track direction of the satellites [Tapley et al., 2004]. Additionally, onboard are highly accurate accelerometers that measure non-gravitational accelerations acting on the satellites, and GPS receivers for precise positioning and time tracking. By implementing an inversion of the GRACE observations, it is possible to derive temporal global solutions of the Earth's gravitational field as monthly [e.g. Tapley et al., 2004; Ramillien et al., 2006] or 10-daily [Bruinsma et al., 2010] estimates. GRACE data are mainly utilised to study the redistribution of water in the Earth's system, including ocean circulation [e.g. Wahr et al., 1998; Janjić et al., 2012], sea-level changes [e.g. Chambers and Schröter, 2011], ice-sheet mass balance [e.g. Velicogna and Wahr, 2006; Horwath et al., 2012], continental water exchanges and storage [e.g. Ramillien et al., 2005; Swenson and Wahr, 2009], droughts and flood [e.g. Freeport et al., 2013], as well as determining glacier and ice-sheet variations and to track solid Earth density variations and crustal movement [e.g. Velicogna, 2009; Wu et al., 2010; Purcell et al., 2011; Velicogna and Wahr, 2013].

2.1.2. Gravity field solutions and errors

The raw data is collected from the satellite by the GRACE project Science Data System (SDS), which is distributed between the University of Texas Centre for Space Research (CSR), Jet Propulsion Laboratory (JPL) and the German Research Centre (GFZ). These data undergo extensive processing and are converted to edited and cleaned data products, labelled as Level-1B, before being further processed to produce monthly gravity field estimates as spherical harmonic coefficients (Level-2), which are then released to the public after validation. They can be obtained through the Physical Oceanography Distributed Active Archive Center (PO.DAAC) at JPL or via the Information System & Data Center at the German Research Center (GFZ).

The solutions are generated by taking into account gravitational variations such as Earth tides, ocean tides, atmospheric pressure fields and barotropic ocean response. However, further effects from hydrology, baroclinic oceanic signals, snow cover and glacial isostatic adjustment (GIA) are not incorporated and need to be separated individually by the user [Biancale, 2012]. It is not possible to separate these un-modelled effects from the temporal gravity signal to determine whether a change in mass is caused by variations in the Earth's crust, surface water, groundwater or atmospheric mass above the measured region, and the contributions need to be separated independently by the user [Wahr et al., 2006]. Wahr et al. [2006] distinguished two error categories: errors in the GRACE gravity field solutions including measurement and processing errors (i.e. accelerometer error, system-noise errors, orbital errors, remaining errors in forcing models) and the measured but unknown signals of surface mass balance and GIA. To remove atmospheric effects, the GRACE project uses ECWMF (European Centre for Medium-Range Weather Forecasts) meteorological fields in the reduction of the observations. This implies that the atmosphere contributes to both error sources, as there are errors in the ECWMF fields as well [Wahr et al., 2006]. Due to a roughly north-south ground track direction, the estimates of the east-west variations are less accurate, which leads to a north-south striping pattern of error, and requires the application of destriping filters to reduce north-south striping [Swenson and Wahr, 2006]. As previously mentioned, ocean tide effects are removed from the raw data, using global ocean tide models, as these affect mass variations around shorelines. However, in general not all of the signal is removed due to uncertainties in the tidal model, and the remaining tidal signals alias into longer period signals [Melachroinos et al, 2009]. The spatial accuracy of the GRACE data estimates is on a scale of a few hundred kilometres or greater, depending on the degree and order of the spherical harmonic model of the GRACE solutions. Hence, the surface mass variation is a spatial average, rather than a point measurement [Bruinsma et al., 2010]. Previously, the spatial resolution varied depending on the study and generally ranged from 400 to 600 km, using a maximum degree of around 50 [Ramillien et al., 2006; Velicogna and Wahr, 2006]. Since the release of the GRACE solutions the Stokes coefficients have been improved and are now available up to degree 80 (GRGS) and 96 (CSR) [Lemoine et al., 2013; Bouman et al., 2014]. The GRACE solutions used for this thesis are provided by the Groupe de Reserches de Géodésie Spatiale (GRGS)

Release 02

In 2009, GRGS published the second series (RL02) of gravity fields in form of 10-day gravity field models as described by Bruinsma et al. [2010]. The processing strategy employed normalised spherical harmonic coefficients up to degree and order 50 at a 10-day interval, with a spatial resolution of ~400 km. The new time-variable mean gravity field EIGEN-GRGS.RL02.mean-field was used as the reference model, the background models IERS2003, FES2004 and MOG2D were used to correct for various tidal variations, such as the gravitational potential of the Earth and that of external bodies [McCarthy and Petit, 2003], ocean tides that affect solid Earth and ocean pole tide deformations [Desai, 2002], and the global barotropic response to atmospheric forced variability of the oceans [Carrère and Lyard, 2003], respectively [Bruinsma et al., 2010]. The ECWMF climate model was used to model atmospheric effects. Due to a stabilisation process during their generation by constraining the coefficients (degree 2 to 50) to the coefficients of the static field, noise in form of North-South striping in the GRGS solutions is already reduced and subsequent filtering is not necessary for the analysis [Lemoine et al., 2007, Bruinsma et al., 2010].

Release 03

After more than ten years of successful operation, reprocessed Level-1B data (“V2”) [Lemoine et al., 2013] of the GRACE mission have been released by JPL and new release 05 solutions have been made available by JPL, CSR and GFZ, recently followed by the release 03 (RL03) solutions from GRGS. The RL03 feature monthly as well as 10-day solutions [Biancale, 2012; Lemoine et al., 2013]. These solutions have been improved by using upgraded versions of data, models and inversion procedures [Lemoine et al., 2013]. In addition to using the new Level-1B V2 data, the gravity solutions feature an improved a priori gravity model, updated and improved versions of the tide model (FES2012 in place of FES2004), the atmospheric dealiasing fields (ECMWF ERA-Interim (every 3 hours) instead of ECMWF operational model (every 6 hours)) and the ocean dealiasing fields (TUGO (every 3 hours) in replacement of MOG2D (every 6 hours). Furthermore, some changes in the K-band ranging and accelerometer parameterisation have been undertaken and the maximum degree has been extended from 50 to 80, improving the spatial resolution [Lemoine et al., 2013]. Additionally, a new “mean field” has been computed and the inversion process is now based on a truncated single value decomposition scheme [Biancale, 2012]. However, due to an error at high latitudes in the FES2012 tidal model, the GRGS RL03 solutions cannot be used in polar areas between 82 and 90 degrees at present [Biancale, 2012].

I chose to use the GRGS solutions for my research due to their stabilisation process that is applied to reduce noise in the form of North-South striping by regularising the inversion for spherical harmonic coefficients. Bruinsma et al. [2010] stated that regularising geopotential coefficients leads to “more accurate geoid difference/EWH anomaly maps than a-posteriori filtering of solutions, because the level of stabilisation of a solution depends on the sensitivity of a given spherical harmonic coefficient to the normal equation system”. Generally both signal and noise are attenuated randomly when filtering and smoothing geopotential solutions, as the data distribution and quality is not known [Lemoine et al., 2007; Bruinsma et al., 2010]. Due to their stabilisation process, the GRGS solutions are also less prone to signal contamination (leakage), which is enhanced by increasing the radius of the Gaussian smoother [Bruinsma et al., 2010; Velicogna and Wahr, 2006].

2.1.3 Relating gravity to surface mass

Transport and redistribution of mass is a recurring process in the dynamic system of the Earth, constantly causing variations in the Earth’s gravity field. The gravity field changes with location and distribution of mass and can undergo temporal changes due to different processes on or above the Earth’s surface or in its interior [Velicogna and Wahr, 2002]. Geophysical processes that induce these anomalies include mass variations that act on the Earth’s crust due to changes in surface load. This includes the distribution of mass (e.g. continent/ocean exchange of water or atmospheric mass variations), elastic deformation caused by a mass increase/decrease (surface load changes in the form of water and ice) and the displacement of mass (e.g. mantle material) inducing a viscoelastic deformation of the Earth’s crust.

The viscoelastic deformation is a long-term signal of GIA in regions that were ice covered during the last ice age [Wahr et al., 1998] whereas elastic deformation is an instantaneous effect caused by surface loads such as hydrological variations. All these gravitational changes affect the orbit of the twin satellites of the GRACE space mission [Tapley et al., 2004] and provide a measure to understand mass transport processes in the atmosphere, hydrosphere, cryosphere and geosphere.

The Earth's gravity field describes the shape of a geoid, which is the equipotential surface that approximates global mean sea level, often described as a sum of spherical harmonics [Wahr et al., 1998]. Spherical harmonics are a common approach for modelling a gravitational field of a planetary body. With Equation (2.1) we can calculate the change in the geoid [Wahr et al., 1998]:

$$U(\theta,\lambda,t) = R\sum_{n=1}^{N}\sum_{m=0}^{n} P_{nm}(\cos\theta)\times\left(\Delta C_{nm}(t)\cos m\lambda + \Delta S_{nm}(t)\sin m\lambda\right) \tag{2.1}$$

where R is the Earth's radius, P_{nm} are the fully normalized Legendre functions, n and m are degree and order of the spherical harmonic coefficients, θ and λ are colatitude and longitude, and ΔC_{nm}, ΔS_{nm} are the dimensionless Stoke's coefficients of the GRACE anomaly fields, respectively, at time t. While Equation (2.1) calculates the general change in the geoid as a function of position and time on Earth, the contribution of surface mass loads, expressed in water equivalent (w.e.), that would be necessary to cause that explicit change in the geoid can be derived [Wahr et al., 1998] using:

$$U^{w.e.}(\theta,\lambda,t) = R\sum_{n=2}^{N}\sum_{m=0}^{n} P_{nm}(\cos\theta)\frac{2n+1}{1+k_n'}\left(\Delta C_{nm}^{elast}(t)\cos m\lambda + \Delta S_{nm}^{elast}(t)\sin m\lambda\right) \tag{2.2}$$

where k_n are elastic Love loading numbers [e.g. Pagiatakis, 1990] and $\Delta C_{nm}^{elast}, \Delta S_{nm}^{elast}$ the elastic Stoke's coefficients at time t, representing the elastic component of the GRACE signal. A vertical elastic deformation is caused by the deformation of the Earth's crust as a quick response to surface load changes by losing or gaining weight and can be described with the elastic Love loading numbers h_n and k_n [Davis et al, 2004]:

$$U^{elast}(\theta,\lambda,t)=R\sum_{n=2}^{N}\sum_{m=0}^{n}P_{nm}(\cos\theta)\frac{h_n^{elast}}{1+k_n^{elast}}\left(\Delta C_{nm}^{elast}(t)\cos m\lambda+\Delta S_{nm}^{elast}(t)\sin m\lambda\right) \tag{2.3}$$

The GIA associated long-term contribution of the viscoelastic deformation can be approximated by [Purcell et al., 2011]:

$$U^{visco}(\theta,\lambda,t)=R\sum_{n=2}^{N}\sum_{m=0}^{n}P_{nm}(\cos\theta)\frac{h_n^{visco}}{k_n^{visco}}\left(\Delta C_{nm}^{visco}(t)\cos m\lambda+\Delta S_{nm}^{visco}(t)\sin m\lambda\right) \tag{2.4}$$

where $\Delta C_{nm}^{visco},\Delta S_{nm}^{visco}$ represents the viscoelastic component of the GRACE signal, and h_n and k_n the viscoelastic Love loading numbers, depending on the degree [Purcell et al., 2011].

The GRACE anomalies are a combination of both components, elastic (induced by changes in surface mass loads) and viscoelastic (GIA) effects, and the total change in the geoid is the sum of the two effects [Tregoning et al., 2009]. Therefore, to allocate the observed mass changes to the correct geophysical sources it is necessary to separate the elastic and viscoelastic components [Wahr et al., 1998]. This is not straight forward, since there is only one GRACE observation but it is a sum of the effects of two processes.

2.2 Satellite Altimetry

In the past 35 years, there has been a series of radar altimetry satellites (e.g. Geosat, TOPEX/POSEIDON, ENVISAT, CryoSat-2) launched to measure surface changes over land, ocean and ice. Satellite altimeters repeatedly orbit the Earth, measuring the distance between the satellite and the Earth's surface. The distance from the satellite to the surface is determined by the time it takes for a radar or laser pulse to leave the satellite, reflect off the Earth's surface and return to the satellite. The return travel time is converted into a distance between the satellite and Earth's surface to visualise a height of sea level and ice sheet topography [Zwally et al., 2002], and topographic variations have been monitored by satellite radar altimetry since 1978 (SEASAT). However, in regions such as Antarctica the large footprint size of conventional radar altimeters (~10 km) causes large uncertainties in the measurement of ice sheet elevation, mainly due to slope-induced errors of the polar ice sheets [Nguyen, 2006]. To overcome this issue, the altimetry mission ICESat was equipped with a Geoscience Laser Altimeter System (GLAS), the first laser altimeter that reduced the footprint size to 60 m [Zwally et al, 2002]. The main errors that are associated with altimetry observations are caused by satellite orbit determination and delays caused by the ionosphere and troposphere. To constrain orbital errors, GPS tracking devices together with ground-based laser ranging systems are used to estimate the orbit of the satellite [e.g. Zwally et al., 2002]. To reduce the error due to ionospheric delays, radar altimetry satellites generally operate using dual frequencies to remove such delays. In addition, microwave radiometers onboard the satellite measure water vapour content to correct for tropospheric delays [Nguyen, 2006]. Compared to radar altimeters, a laser altimeter has the advantage of higher accuracy and a smaller footprint, but contains additional error sources such as the determination of pointing [Nguyen, 2006]. Despite the availability of various altimetry missions, only a few mission results can be used to study the polar ice sheets due to the inclination of the satellite orbit, allowing the satellite to pass above (or nearly above) both poles. The primarily altimetry missions used to research ice sheet topography of the AIS are the missions of ENVISAT (including the former ERS-1, ERS-2), ICESat and CryoSat-2:

ERS-1, ERS-2 and ENVISAT 1991 - 2012:

The first of the European Remote Sensing satellite missions, ERS-1, was launched in 1991 and orbited the Earth on a repeated cycle of ~35 days to a latitude of about 82.4 degrees south. The footprint size of the radar altimeter was 1.7 km and the height accuracy was over 73 cm over ice sheets [Nguyen, 2006; Rémy et al., 2014]. The mission continued until 1996 when it was replaced by the follow on mission ERS-2, which continued until 2001. In 2002, ENVISAT was launched and collected surface topography observations until 2012 when, unexpectedly, contact was lost with the satellite. Both ERS-2 and ENVISAT had the same orbit and repeat cycle as ERS-1. Despite the same footprint size, height accuracy for the ENVISAT mission improved to ~35 cm compared to > 73 cm for the ERS-missions. All three missions were equipped with a Ku-Band radar altimeter and repeatedly orbited the Earth with a 98.5 inclination [Horwath et al., 2012]. Recently the REAPER (REprocessing of Altimeter Products for ERS) project has been finished, covering both ERS-1 and ERS-2 missions, providing a greatly improved dataset [Gilbert et al., 2014]. Studies using ERS data to study the AIS include work from Wingham et al. [1998], Zwally et al. [2002] and Zwally et al. [2005], studies using ENVISAT data include Horwath et al. [2012], Flament and Rémy [2012], Rémy et al. [2014], Michel et al., [2014]. The follow up mission SARAL/AltiKa was launched in February 2013, to measure the Earth's topography on exactly the same orbit, extending the previous three missions [Rémy et al., 2014; Michel et al., 2014].

ICESat 2003 - 2009:

With the launch of the Ice, Cloud and land Elevation Satellite (ICESat) in January 2003, the first laser altimeter became operational, to measure surface elevation changes primarily of ice sheets but also of land, ocean, and vegetation canopy [Zwally et al., 2002]. Despite a predicted mission life span of three years, and premature failures, ICESat operated until October 2009, collecting data for seven years. Initially ICESat had three lasers aboard, one laser operating at a time, to provide annual coverage on a 183-day repeated ground track period. With a 60 m diameter laser footprint and 172 m along-track spacing, the predicted accuracy for surface elevation measurements was 10 cm [Zwally et al., 2002]. However, due to a failure in a pump diode array of Laser 1 the decision was made to modify the operation plan by reducing the usage of the other two lasers, in order to extend the mission life [Abshire et al., 2005]. The satellite orbited the Earth at around 600 km altitude at an inclination of 94° with a modified ground track period of 91-days and provided latitudinal coverage up to 86 degrees. For a period of around 33 days the lasers were turned on up to three times a year [Schutz et al., 2005; Abshire et al., 2005] until Laser 2 failed in 2004 due to the same failure as Laser 1 [Abshire et al., 2005]. To mitigate the rapid energy decline that occurred in the first two lasers, Laser 3 was operated at a lower temperature [Abshire et al., 2005], resulting in a slower energy decline rate and thus successfully operated until 2009. Although the data quantity and spatial resolution was significantly reduced and tracks were rarely repeated precisely [Slobbe et al., 2008; Pritchard et al., 2009; Sørensen et al., 2011], the altimeter recorded ice height changes to an accuracy of < 1.5 cm yr^{-1} averaged over 100 x 100 km sections [Nguyen, 2006; Hoffmann, 2014].

ICESat carried the Geoscience Laser Altimeter System (GLAS), consisting of a 1064 nm infrared laser pulse to measure dense cloud heights and surface topography [Zwally et al., 2002; Schutz et al., 2005]. The instrument had three identical laser transmitters, a receiver telescope, a solid-state detector, a subsystem to measure the angle of the laser pulses and waveform digitisers to record the laser backscatter signal [Zwally et al., 2002]. On-board GPS receivers allowed orbit determinations to better than 5 cm. Star-trackers, measuring the position of stars, enabled pointing accuracy to locate footprints to 6 m horizontally and the spacecraft attitude controlled the laser beam to within 35 m of reference surface tracks [Zwally et al., 2002].

CryoSat-2 2010 - present:

After the first satellite (CryoSat-1) was lost in 2005 due to a launch failure the satellite was duplicated and CryoSat-2 was successfully launched in 2010. The satellite carries enhanced instruments to significantly improve data sampling and to extend the spatial coverage of previous missions to a latitudinal range of 88 degrees using an orbit inclination of 92 degrees [Wingham et al., 2006]. A synthetic aperture mode is included in the radar that improves the along-track resolution to about 250 m [Francis et al., 2010]. It includes a second antenna and receiver chain to enable interferometry to improve the localisation of the reflections. Star trackers and GPS receiver on-board measure the orientation of the interferometer and precisely determine the orbit, respectively [Francis et al., 2010]. CryoSat-2 carries the Ku-Band Synthetic Aperture Interferometric Radar Altimeter (SIRAL), which consists of an antenna subsystem, radio-frequency unit and digital processing unit. There are three different measurement modes available to choose the antenna on reception, transmitted bandwidth and timing of transmitted chirps [Wingham et al., 2006]. The low-resolution mode (LRM) is used to measure the topography of the oceans and the smooth interior of ice sheets. For improved sampling along steep ice sheet margins the higher pulse repetition frequency of the synthetic aperture mode (SARM) and synthetic aperture interferometric mode (SARInM) is used [Wingham et al., 2006].

The accuracy of the altimetry measurements is influenced by several elements including precise determination of the orbit, attitude and pointing of the radar/laser, atmospheric delay and forward scattering, ground track geometry, surface slope, saturation, and instrument bias and failure, which lead to reduced resolution. A precision orbit and attitude determination is performed to calculate the pointing of the laser and its footprint position on the surface, using onboard GPS tracking systems (orbit determination), star tracker and gyroscopes (attitude and pointing determination) [Schutz and Zwally, 2008]. The slope dependency represents the main error source, as ground tracks generally do not overlap at the same position, thus measuring topographic changes possibly due to a difference in the ice sheet terrain rather than changes in ice thickness [Pritchard et al., 2009b]. Steeper slopes near the ice sheet margins have significant impact on estimating surface elevation in regions of greater changes due to surface melt and ice discharge into the ocean. Moreover, a slope correction is further needed to correct for the footprint size of conventional radars such as ENVISAT, as the satellite return signal originates from the closest point to the satellite, rather then the point directly underneath the satellite (nadir) [Hurkmans et al., 2012].
Another issue is the penetration of the transmitted microwave radar into the snow, before it reflects back to the satellite [Arthern et al., 2001]. Not only can the radar penetrate several meters into the snowpack [Arthern et al., 2001], but the penetration can also vary through time [Pritchard et al., 2010] due to varying snow/firn conditions and densities. Although, radar penetration uncertainties are reduced using a laser altimeter (ICESat) [Pritchard et al., 2010], uncertainties in the determination of the surface elevation remain.

In addition, ocean-loading and ice shelf tidal corrections are applied to the altimetry signal, as well as atmospheric delay corrections for laser altimeters [Zwally et al., 2002]. When using laser altimeter correcting for atmospheric forward scattering and delay is important as the performance of the pulse signal can be degraded when in contact with cloud cover. When the cloud cover is extremely thick the pulse reflects of the clouds, not measuring the Earth's surface but the height of the cloud cover instead [Fricker et al., 2005].

2.2.1 Altimetry analysis techniques

Different techniques are used to analyse altimetry observations, which can be broadly broken into two categories: crossover and along-track analysis. Each method has advantages and disadvantages. A satellite that orbits the Earth covering both polar regions has an ascending (travelling south to north) and descending (travelling north to south) track. The location where both tracks intersect is called the campaign crossover [e.g. Brenner et al., 2007]. The ground track of the satellite shifts due to perturbations of the orbit, which results in varying deviations of the repeated ground track. Therefore, the surface topography needs to be determined to correct elevation changes due to surface slope rather than to changes in ice mass. Alternatively, the topography can be estimated in the same least squares inversion used to determine observed ice height changes [Flament and Rémy, 2012].

Crossovers are ideal to estimate elevation changes as the rate of change can be estimated directly from the crossover location, which is determined by obtaining the position of the intersection point of the ascending and descending track [Legrésy et al., 2005]. Different methods are used to estimate the campaign crossover position: Zwally et al. [2005] used crossovers of the ERS-1 and ERS-2 satellites that are within a 100 km circle centred on a grid point. Then they determined the elevation differences at crossovers between epoch T_1 and all successive T_i, and combined this first sequence with the second sequence of those crossings between T_2 and T_i. This is repeatedly done for all sequences, which are subsequently combined into one elevation time series [Zwally et al., 2005]. Brenner et al. [2007] introduced a polynomial fit to calculate the intersection of the ascending and descending ICESat ground track, and estimated the elevation at the crossover by interpolating available heights along the ground track closest to the crossover location. Gunter et al. [2009] used cubic spline interpolation on ICESat crossover data points within ~400 m to refine the position of the campaign crossover. A cluster of inter-campaign crossovers, using ground tracks from different laser campaigns (using the ground track of a different laser), is used to determine the height at the crossover using cubic-spine interpolation. Although the crossover analysis technique is very effective on ICESat tracks at high latitudes, it becomes less accurate towards the coastal areas of the Antarctic ice sheet, as the density of crossovers is highest near the poles and decreases from ~ 11,340 near 85.5° south to ~ 70 near 70.5° south, over an average 100 x 100 km^2 area, due to the chosen orbit of the satellite [Nguyen, 2006]. However, this method is based on the assumption that the signal of height changes is constant, which may be true in the dry interior of Antarctica but not near the coastal margins, where strong slopes impede estimations of the rate of change.

Although the crossover method is more accurate due to the direct crossing point of the tracks, possible biases between the ascending and descending tracks can influence the results using this method. Moreover, it only covers a small area, using only a small amount of available data, leaving much of the along-track coverage unused [Legrésy et al., 2005]. Therefore, using available along-track data provides a much greater spatial coverage, especially near the ice sheet margins, including around 100 times more measurements [Legrésy et al., 2005]. However, the along-track analysis is more susceptible to errors in the rate estimates due to changes in ice sheet topography. A surface slope correction is applied to remove potential bias due to topographic variations and varying positions of the measurement point over time. In terms of determining the ice sheet topography, the most prevalent method is to break the ground track into smaller segments, covering three to four data points per campaign, and to apply a parameterisation for a seasonal signal, underlying surface topography and the secular trend of elevation [e.g. Legrésy et al., 2005; Howat et al., 2008; Smith et al., 2009; Mohold et al., 2010, Zwally et al., 2011; Ewert et al., 2012]. Slobbe et al. [2008] represented a method that is based on elevation differences at crossover points and can be written as the sum of a signal, a terrain slope contribution and a noise term, which is assumed to be random. They used only overlapping footprints of the ICESat mission to eliminate the need for terrain smoothing and interpolation, which is only needed to correct the obtained elevation differences for the influence of slope. However, the centre points of the overlapping footprints generally do not overlap and a correction has to be applied to the underlying topography. Slobbe et al. [2008] used a digital elevation model published by DiMarzio et al. [2007] for their slope corrections. The digital elevation model is linearly interpolated to estimate the elevation of the ice sheet at a given location and to subtract the simulated elevation from the ICESat measurements. A trend is fit through the elevation time series at each grid node and the rates are averaged to a 1°x1° grid [Slobbe et al., 2008]. The problem with this method is that no adequate accurate high-resolution digital elevation model exists for polar ice sheets and the quality of the interpolated elevation models depends on the amount of data [Sørensen et al., 2011; Ewert et al., 2012]. This leads to uncertainties in estimating the rate of change in height from the ICESat observations.

Pritchard et al. [2009a,b] used a different method processing ICESat observations. In their procedure, Triangular Irregular Networks are used, which means all measurements have two neighbours lying within 300 m to ensure that the interpolation distance is never greater than 260 m [Pritchard et al., 2009b]. The model produces long, ribbon-like, linearly interpolated surfaces that are located between closely spaced, near parallel tracks, which represent surface heights for each epoch. Where ground-track footprints are available for an earlier or later epoch the interpolated elevation and acquisition date from the Triangular Irregular Networks is extracted to compare the measurements precisely. From that, the elevation change per epoch can be calculated, which are corrected again to limit further bias from the main error sources. Then the spatial mean of the filtered points over a radius of 10 km is taken [Pritchard et al., 2009b].

Nonetheless, all these methods are prone to surface slope bias and must be corrected for it. Sørensen et al. [2011] presented different methods to correct for surface slope, including a reference surface that is created for each along-track segment to obtain the height of the reference surface for the measurement location. This height is removed from the ICESat height to correct for the slope. However, this method is sensitive to seasonal variations and therefore at higher risk of introducing bias when there are significant changes [Sørensen et al., 2011].

Rémy et al. [2014] processed ERS-2 and ENVISAT points at 1 km intervals and considered consecutive data of three along-tracks. They performed a geometric correction for surface topography and a backscatter echo correction to correct for snowpack characteristics. The temporal trend was inverted and mean values of height, backscatter and waveform parameters were obtained. By re-trending the temporal residuals, time series for each parameter were obtained [Rémy et al., 2014].

Hoffman [2014] developed a new method to estimate the local surface slope using a digital elevation model that has been derived from gridded estimates of ice height at ICESat crossover points. Over a crossover grid, that geographically spans all campaign crossovers of a location, a static grid was created on which heights were interpolated at the epochs of all campaigns. The estimate of the elevation change over time is made by computing a weighted least-square regression to the height time series of each grid node and then computing a weighted mean value for all grid nodes to derive the "crossover" height rate [Hoffmann, 2014]. This was repeated for different interpolation techniques, with the Green's function spline interpolation found to be the most accurate method. This not only allows to assess height rates at one location over time, but also to evaluate a digital elevation model directly from the data, which is used to estimate the slope at crossovers [Hoffman, 2014]. The same approach to estimate height changes over time is applied to the along-track analysis. The slope estimates at the crossovers are then interpolated to remove the surface slope from the along-track measurements. Although the elevation change estimates from along-track measurements are naturally less precise than the rate estimates at crossovers, combining both methods significantly increases the accuracy of the slope correction. Moreover, it provides an important measure to validate the less accurate along-track estimates [Hoffman, 2014].

Similarly, Helm et al. [2014] processed CryoSat-2 observations using a re-tracking method to filter waveforms and to determine the range. A digital elevation model was generated using CryoSat-2 observations and was applied to correct for surface slope. Their method differs from previously described methods and is based on the relocation slope correction and interferometric processing. An empty grid was generated where all points within each pixel were determined. The elevation change for each pixel is estimated using a least square model fit to the points [Helm et al., 2014].

2.2.2 Converting elevation changes to volume and mass changes

To obtain variations of ice sheet mass balance, surface height observations must be converted to mass variations. Any height change in ice sheet topography is caused by one or more of the following processes: a) surface mass balance (SMB), b) firn compaction, c) ice dynamics and ice discharge, d) glacial isostatic adjustment (GIA), and the elastic response of the lithosphere to surface load. A change in surface height can be described by:

$$\frac{dH}{dt} = \frac{SMB}{\rho_s} - V_{fc} - V_{ice} - V_B + V_{GIA} + V_{elast} \qquad (2.5)$$

where SMB represents all components that affect surface mass balance (kg m^{-2} yr^{-1}), ρ_s is the density of surface snow (kg m^{-3}), and V_{fc}, V_{ice}, V_B, V_{GIA} and V_{elast} represent the vertical velocity (m yr^{-1}) of the surface due to firn compaction, ice dynamics, basal melt, GIA and elastic deformation, respectively [e.g. Helsen et al., 2008b]. The elastic deformation is only small and describes the instant response of the lithosphere to surface load changes related to SMB, ice dynamics and GIA. The goal is to separate all four signals in order to obtain ice sheet mass balance estimates. Generally, the contribution of the GIA signal (V_{GIA}) is removed using a GIA model (Chapter 1, Section 1.4).

Changes in SMB and firn compaction primarily affect the firn layer that covers the ice sheet, increasing or reducing the thickness of the firn layer. Although ice dynamics affect the entire ice sheet, the resulting ice discharge into the ocean is generally considered as a thickness change within the ice column, rather than the firn column. Therefore, in order to determine variations in the ice column, the observed elevation change (dH^{Obs}/dt) is corrected (dH^{corr}/dt) for height changes occurring within the overlying firn layer (V_{fc}), which is removed using a firn densification model (see Chapter 3):

$$\frac{dH^{corr}}{dt} = \frac{dH^{Obs}}{dt} - \frac{SMB}{\rho_s} - V_{fc} + V_{GIA} + V_{elast} \tag{2.6}$$

By removing the signal of the firn column, the corrected elevation change, dH^{corr}/dt, that is solely related to mass balance variations of the glacier ice is obtained. If there is no change within the ice, the change in elevation from the firn compaction model should match the observed altimetry observations [Ligtenberg et al., 2011; Hoffman, 2014]. The elevation estimates can now be converted into volume changes (dV/dt) for selected sections by multiplying the area size (A_{gr}) of the grounded ice by the elevation change of the basin [Helsen et al., 2008]:

$$\frac{dV}{dt} = \frac{dH^{corr}}{dt} A_{gr} \tag{2.7}$$

Subsequently, the volume estimates can be converted into mass changes (dM/dt) by multiplying the volume of the basin by the density (ρ_i) of glacier ice [Helsen et al., 2008]:

$$\frac{dM}{dt} = \frac{dV}{dt} \rho_i \; . \tag{2.8}$$

2.3 GPS – Global Positioning System

GPS systems are not only used onboard satellites to determine precise attitude or orbit positions but are also used on Earth to detect vertical bedrock movements. The concept of the Global Positioning System is a signal transfer between a GPS satellite and GPS receiver including the location, time and current satellite position at the moment the message is transmitted. This message is used to determine the transit time of the message and to calculate the distance to each satellite. In case of stationary GPS stations installed on rock outcrops, vertical movements can be observed by the GPS measurements, moving vertically and horizontally with the bedrock. Naturally, deviations will be visible due to the immediate elastic response of the Earth's crust. However, over a longer period of time trends become visible, indicating whether the lithosphere uplifts or subsides. In region where large ice sheets once covered the lithosphere, continuing uplift reflects ongoing glacial isostatic adjustment (Chapter 1, Section 1.4). Uplift rates beneath today's ice sheets remain undetermined due to the remaining ice cover, but are assumed to be present due to the more comprehensive former extent and thickness of the ice sheet.

In regions like Antarctica, ground-based GPS stations are installed on exposed bedrock locations to monitor uplift rates over a certain period [e.g. Argus et al., 2011; King et al., 2012; Whitehouse et al., 2012b]. Unfortunately, the coverage of GPS sites in Antarctica is not enough for a comprehensive network of observations, due to the limited ice-free areas, mainly located around the coastal regions, Transantarctic Mountains and the Antarctic Peninsula.

2.4. RACMO2.1/ANT – Regional Atmospheric Climate Model 2.1 / Antarctica

Climate data are taken from the regional climate model RACMO version 2.1 of the Royal Netherlands Meteorological Institute (KNMI). The model adopts the dynamical processes from the High Resolution Limited Area Model (HIRLAM) and the physical atmospheric processes from the European Centre for Medium-range Weather Forecasts (ECMWF) [Reijmer et al., 2005] and is forced by ERA-Interim re-analysis data at the lateral boundaries [e.g. Ligtenberg et al., 2011; Lenaerts and van den Broeke, 2012]. Besides the worldwide available climate model, specific polar versions have been developed by the Institute for Marine and Atmospheric research at Utrecht University (UU/IMAU) to explicitly adapt the unique climate over the polar ice sheets. RACMO data is available on a spatial resolution of 27 km and a temporal resolution of six hours for the period 1979-2012 [e.g. Ligtenberg et al., 2011; Lenaerts et al., 2012]. Climate simulations are available for liquid and solid precipitation, surface temperatures, evaporation, wind speed, surface melt as well as sea ice cover and sea surface temperatures, amongst others [Ligtenberg et al., 2011]. The RACMO2.1/ANT model is specifically adapted to climatic conditions in Antarctica and has been validated with field observations where available, providing a good representation of Antarctic's near surface climate [e.g. van den Broeke, 2008; Kuiper Munneke et al., 2011; Lenaerts et al., 2012; Lenaerts and van den Broeke, 2012]. The uncertainty in the simulated surface mass balance for the grounded ice sheet is ~7% or 144 Gt yr^{-1} [Lenaerts et al., 2012].

The most recent version available is RACMO2.3. Unfortunately, this later version of the RACMO climate model was not available at the time I obtained the dataset, and an exchange of the most recent version has not been possible to date.

Chapter 3

Modelling of firn compaction and model sensitivity to climate variations

3 Introduction

When using satellite altimetry to quantify ice mass balance it is important to correct the observations for elevation changes due to GIA and firn compaction. As described in Chapter 1, Section 1.3, firn is the intermediate product between fresh snow and glacier ice, and exhibits density values between ~350 kg m^{-3} (fresh snow), and ~900 kg m^{-3} (glacier ice). The thickness of the firn layer varies across the AIS and the densification process is strongly dependent on temperature and accumulation rates.

To take the process of firn compaction into account and to subtract it from the change in elevation from altimetry observations, several models have been established to describe the process and to quantify the rate at which firn compacts in Antarctica [e.g. Herron and Langway, 1980; Zwally and Li, 2002, 2011; Helsen et al., 2008; van den Broeke, 2008; Arthern et al., 2010; Ligtenberg et al., 2011; Simonsen et al., 2013]. The most recent densification model for Antarctica was published by Ligtenberg et al. [2011] and is an improved semi-empirical model that has been validated against 48 firn cores across the AIS.

However, with the physics behind the process of densification still not fully understood and vast areas remaining without in-situ observations, it is still not known which process has a greater impact on firn compaction rates: overburden pressure induced by accumulation or temperature variations near the surface and within the upper firn layers.

While some models suggest that accumulation is the main driver of firn compaction (e.g. Arthern and Wingham, 1998, Helsen et al., 2008), others suggest that temperature variations have a significant impact on compaction rates (e.g. Herron and Langway, 1980, Zwally and Li, 2002). More recently, this has been supported by field observations [Arthern et al., 2010], and Arthern et al. [2010] found that compaction rates are dependent on accumulation as well as temperature. Based on their findings, a dry snow densification expression was proposed that incorporates overburden pressure due to snowfall and temperature variations at the surface as well as within the firn column [Arthern et al., 2010].

Therefore two questions emerge: 1) How sensitive are the models to the input values of accumulation and temperature and, 2) how important is the accuracy of these models in terms of determining mass balance changes from altimetry observations, and thus Antarctica's contribution to sea level changes?

This is especially important as miscellaneous climate models suggest different values for accumulation and temperatures across the AIS, primarily based on the few available observations that exist for Antarctica. Not only are there differences between the proposed values of the regional climate models, with differences that may be small in some but large in other regions [Bromwich et al., 2011], but each regional climate model also contains uncertainties within the climate simulations.

To assess the importance of accurate measurements of surface temperature and accumulation rates, I developed a firn compaction model and varied the input values to study changes in the rate of the vertical velocity of the surface due to firn compaction. I applied different biases to both the accumulation rate and the surface temperature, representing differences between regional climate models as well as uncertainties within the RACMO2/ANT simulations used in this thesis.

In this chapter I first describe published firn compaction models for Antarctica before I explain my own firn compaction model and show the results of my model together with the sensitivity runs. I finish the chapter with an uncertainty estimation of my firn compaction model and the conclusions.

3.1 Firn densification models

Theories on dry snow densification have been proposed as early as the 1950s [Robin, 1958; Benson, 1957] and have been adapted and improved since then. Herron and Langway [1980] published an empirical model whose ideas are still widely used and commonly build the substructure for firn densification models. They identified different stages of densification, with the most rapid densification rate in the first stage and a much slower observed densification rate after a density of ~550 kg m^{-3}.

The parameterisation of Herron and Langway [1980] was defined using steady-state density profiles from Greenland and Antarctica, and assuming an Arrhenius relation (3.1) for temperature changes within the firn column:

$$k = K_{Ar} e^{\left(-\frac{E}{RT}\right)} \qquad (3.1)$$

The Arrhenius equation is used to calculate the dependency of the rate constant, k, to a change in temperature, T, of a chemical reaction. The exponential expression resembles the Boltzmann distribution, which defines the distribution of molecules at a particular temperature, with the activation energy, E, the gas constant, R, and the temperature T. K_{Ar} is the frequency factor or pre-exponential factor and depends on the frequency of molecule collisions on their orientations. It describes an empirical relationship between the rate constant and temperature [Bahlburg and Breitkreuz, 2004]. The Herron and Langway [1980] equation to estimate the densification rate within a firn column is given by:

$$\frac{d\rho}{dt} = k\left(\frac{A^{\alpha}}{\rho_i}\right)(\rho_i - \rho) \qquad (3.2)$$

where k represents the rate constant from the Arrhenius equation, A the accumulation rate, a a densification constant and ρ and ρ_i the local density of the firn layer and the density of ice, respectively. Substituting for k, the densification rate can be expressed as:

$$\frac{d\rho}{dt} = K_{Ar}\left(\frac{A^{\alpha}}{\rho_i}\right)(\rho_i - \rho)e^{\left(-\frac{E}{RT}\right)} \qquad (3.3)$$

To account for the different densification stages below and above 550 kg m^{-3}, Herron and Langway [1980] introduced an accumulation constant that is dependent on the different densification mechanism as well as a temperature rate constant for the Arrhenius relation. The densification rate after Herron and Langway [1980] is obtained by solving the general densification rate equation for densities below 550 kg m^{-3}:

$$\frac{d\rho}{dt} = 11\frac{A^{\alpha}}{\rho_i}e^{\left(-\frac{10160}{RT}\right)} \qquad (3.4)$$

and for densities above 550 kg m^{-3}:

$$\frac{d\rho}{dt} = 575\sqrt{\frac{A^{\beta}}{\rho_i}}e^{\left(-\frac{21400}{RT}\right)} \qquad (3.5)$$

In both expressions ρ_i represents the density of ice (kg m^{-3}), R the gas constant (=8.314 J mol^{-1} K^{-1}), T the temperature (K) and A the accumulation rate (in m w.e. yr^{-1}). α and β represent the accumulation constants that are determined by comparing accumulation rate and slopes at sites. Commonly the constants are taken as 1.1 for α, and 0.5 for β, representing average values of accumulation constants, determined by comparing slopes for each stage of densification at sites with constant temperatures but different accumulation rates [Herron and Langway, 1980]. The two numbers at the beginning of each equation are the determined Arrhenius rate constants K_{Ar}.

Arthern & Wingham [1998] developed a one-dimensional numerical model of time evolving firn densification and evaluated the impact of changes in accumulation rate, temperature and surface snow density. They found that an elevation change caused by firn compaction is significant, especially due to accumulation variations. However, their modelling showed that the impact of temperature on the densification model was relatively small.

Zwally & Li [2002] have a greater temperature sensitivity in their model and showed that variations in surface temperature are sufficiently strong to cause seasonal elevation changes. More recently, this has been strongly supported by field observations in Antarctica where Arthern et al. [2010] examined in-situ measurements at three different sites, concluding that the temperature sensitivity of snow compaction has been underestimated.

The Zwally and Li [2002] parameterisation follows the idea of Herron and Langway [1980] and was established from experiments on grain growth and a newly introduced temperature-dependent, empirical constant that accounts for differences between the grain growth rate and the densification rate. After experimental results showed that grain growth and ice creep are sensitive to temperature variations [Jacka and Li, 1994], Zwally and Li [2002] introduced a temperature-dependent activation energy $E(T)$ and rate constant $K(T)$ into the Arrhenius relation [Zwally and Li, 2002; Li and Zwally, 2004; Li and Zwally, 2011]. Moreover, they introduced a temperature-dependent adjustable parameter β that accounts for differences in the rate constant between processes of densification and grain growth:

$$\frac{d\rho}{dt} = \beta K_{Ar}(T)\left(\frac{A}{\rho_i}\right)(\rho_i - \rho)e^{\left(-\frac{E(T)}{RT}\right)} \tag{3.6}$$

Substituting their experimental results on the temperature dependence of grain growth, rate constant and activation energy, Equation (3.6) becomes:

$$\frac{d\rho}{dt} = \beta\left(\frac{A}{\rho_i}\right)(\rho_i - \rho)8.36(273.15 - T)^{-2.061}. \tag{3.7}$$

In previous calibrations it was assumed that β was a function of annual mean temperature only. However, Li & Zwally [2011] stated that new tests showed that the accumulation rate also has an influence, which is similar to the density-age relation of Herron & Langway [1980] where both temperature and accumulation rate were involved [Li and Zwally, 2011]. Therefore, present values of β are a function of annual mean temperature and accumulation rate. Li & Zwally [2011] modified their values to fit density profiles in Greenland and have furthermore considered the two different stages of densification before and after the critical density of 550 kg m^{-3}. However, the temperature range that has been proposed to express the β parameter is not large enough to cover the temperature range found in Antarctica [Helsen et al., 2008]. To adjust for the much colder temperatures, Helsen et al. [2008] established a new β-T_s relation, with T_s being the annual mean surface temperature in Kelvin:

$$\frac{d\rho}{dt}=\left(76.138-0.28965T_{av}\right)\left(\frac{A}{\rho_i}\right)\left(\rho_i-\rho\right)8.36\left(273.15-T\right)^{-2.061} \qquad (3.8)$$

with the mean annual temperature T_{av} (K) incorporated into the estimation of the β parameter. With the introduced temperature dependency, the initial Zwally and Li [2002] parameterisation (Equation 3.6) and, correspondingly the adapted parameterisation for Antarctica after Helsen et al. (2008) (Equation 3.8) leads to a greater sensitivity and faster compaction rate in response to temperature variations, compared to the original Herron and Langway [1980] parameterisation.

The influence of temperature in a firn column and the sensitivity of firn compaction rates to temperature variations have been further investigated by Arthern et al. [2010]. Following Zwally and Li [2002], a simplified version of their parameterisation and the updated Helsen et al. [2008] model has been used to establish a dry snow densification expression. A new estimate of the activation energy has been derived and laboratory experiments have shown an energy barrier for molecular diffusion through the lattice of ice crystals, known as Nabarro-Herring creep [Arthern et al., 2010]. Subsequently, they coupled the densification rate with a grain-growth rate estimation, which considers heat-conduction, snow load and normal grain-growth. However, simplifying assumptions have been made for the overburden pressure and temperature fluctuations of the grain-growth rate [Arthern et al., 2010, Appendix B]. Both equations are combined to obtain the densification rate:

$$\frac{d\rho}{dt} = CAg\left(\rho_i - \rho\right)e^{\left(\frac{-E_c}{RT}+\frac{-E_g}{RT_{av}}\right)} \tag{3.9}$$

where A is the accumulation rate (kg m^{-2} yr^{-1}), g the gravitational acceleration, and ρ and ρ_i are the local density and ice density (kg m^{-3}), respectively. The exponential term includes the activation energy constants (kJ mol^{-1}) for creep and for grain-growth, E_c and E_g, respectively, the gas constant R (J mol^{-1} K^{-1}) and the temperature (in K), likewise for creep, T, and, simplified as annual average temperature, for grain-growth, T_{av}. The grain-growth constant C (m s^2 kg $^{-1}$) is calculated for low and high density ranges and has different values below (0.07) and above (0.03) the critical density of 550 kg m^{-3}.

Built on the method of Arthern et al. [2010], the most recent firn compaction model for Antarctica has been published by Ligtenberg et al. [2011], who established a steady state and a time-dependent model version. The model not only considers ablation but also estimates melt and refreezing processes within the firn column. Equation (3.9) is used to develop the time-dependent model. Compared with 48 firn cores across Antarctica, Ligtenberg et al. [2011] found that Equation (3.9) over-predicts the rate of densification for most regions in Antarctica. In comparison with the observed density depths they found that the effect of the average annual accumulation on the densification rate is too large. To modify the densification rate for the correct accumulation dependence, they obtained a ratio of modelled to observed depths (MO), and multiplied the relation of the regression with the densification expression in Equation (3.9):

$$\begin{aligned} MO_{550} &= 1.435 - 0.151\ln\left(A\right) \\ MO_{830} &= 2.366 - 0.293\ln\left(A\right) \end{aligned} \tag{3.10}$$

After introducing the accumulation dependence into Equation (3.9) the firn densification model is found to be in agreement with 48 steady state firn profiles [Ligtenberg et al., 2011].

Once the densification rate is estimated, the vertical velocity of the surface due to firn compaction (V_{fc}) can be assessed. At depth, z, the velocity of firn compaction is given by the density $\rho(z)$ and the compaction rate $d\rho(z)/dt$, and is obtained by integrating the displacement of the compacted firn layer over the length of the firn column below the surface (z=0):

$$V_{fc}(z,t)=\int_{z_i}^{z}\frac{1}{\rho(z)}\frac{d\rho(z)}{dt}dz \tag{3.11}$$

with depth z, density ρ and densification rate $d\rho(z)/dt$ [Helsen et al., 2008; Li and Zwally, 2011]. The value of the vertical displacement of the surface can now be subtracted from surface elevation measurements to calculate the rate of change in surface height.

My model is described in the next section and is set up following the firn compaction model of Ligtenberg et al. [2011]. The idea of developing my own firn compaction model was not to improve existing models, but to investigate the importance of the process of firn compaction and its sensitivity to variations in the input values that represent the near-surface climate. More importantly, I wanted to employ my own model to my modelled surface height and surface mass balance estimations in Chapter 4.

3.2 Model input and method

3.2.1 Atmospheric forcing

My firn compaction model is forced using the surface temperature, near-surface wind speed and surface mass balance, taken from the regional atmospheric climate model RACMO2/ANT, which is specifically adapted to the Antarctic climate [e.g. van den Broeke, 2008; Kuiper Munneke et al., 2011; Lenaerts et al., 2012]. The horizontal resolution of RACMO2/ANT is 27 km and data availability is provided from 1979–2011 at a temporal resolution of 6 hours [Ligtenberg et al., 2011].

3.2.1 Firn compaction model

My firn compaction model is based on the basic principle of a one-dimensional time-dependent model that estimates density and temperature individually for each layer and at each time step in a vertical firn column. At each location, newly added snowfall is considered as the new surface layer that is based on the amount of accumulation and the surface temperature. The accumulation, provided in mass (kg m^{-2}), is converted into snow equivalent (in m) using modelled surface snow densities. This provides me with the initial thickness and density of the layer at the surface. At each time step a new layer forms on top, burying previous layers, both moving and compacting each layer downwards in the firn column until it becomes glacier ice. The density of each layer in the firn column is recalculated at each time step by calculating the densification rate of each layer. Also recalculated at each time step is the new thickness of the compacted layer, the new density and the local temperature, providing temperature-depth and density-depth profiles through the firn column. To create the initial firn layer the model requires a spin-up period that refreshes the entire firn layer individually at each location. This is done by repeating the time series of the input values long enough for the firn layer to reach steady state.

The surface snow density is determined using a parameterisation of Kaspers et al. [2004], with an introduced slope correction for Antarctica by Helsen et al. [2008]:

$$\rho_s = -151.94 + 1.4266\left(73.6 + 1.06T + 0.0669A + 4.77W\right) \tag{3.12}$$

where T is the annual average surface temperature (K), A the average annual accumulation rate (mm w.e. yr^{-1}) and W the average annual wind speed (m s^{-1}) at 10 m above the surface [Kaspers et al., 2004]. With the surface snow density being largely dependent on near surface climate, the sensitivity of the snow density parameterisation and its implications for firn compaction rates are assessed in Section 3.3 of this chapter.

To calculate the densification rate of the firn column I use the dry snow densification expression of Arthern et al. [2010] as previously described in Equation (3.9):

$$\frac{d\rho}{dt} = CAg(\rho_i - \rho)e^{\left(\frac{-E_c}{RT}+\frac{-E_g}{RT_{av}}\right)} \tag{3.13}$$

where A is the average annual accumulation (mm w.e. yr^{-1}), T is the local temperature within the firn column (K), T_{av} is the annual average surface temperature (K) and ρ and ρ_i the local density and the ice density (kg m^{-3}), respectively. R is the gas constant (8.314 J mol^{-1} K^{-1}), g the gravitational acceleration (9.806 m s^{-1}) and E_c, E_g and C are constants for the activation energy for self-diffusion of water molecules (60 kJ mol^{-1}), the activation energy for grain growth (42.4 kJ mol^{-1}) and the rate coefficient for grain growths (0.07 and 0.03 m s^{-1}), respectively. Note that the constant C has different values above and below the critical density value of 550 kg m^{-3}, to account for faster densification near the surface [Arthern et al, 2010; Ligtenberg et al., 2011]. Following Ligtenberg et al. [2011] I apply the accumulation factor, suggested in their paper, to correct for accumulation rates:

$$\begin{aligned} \alpha_{550} &= 1.435 - 0.151\ln(A) \\ \alpha_{830} &= 2.366 - 0.293\ln(A) \end{aligned} \tag{3.14}$$

The temperature throughout the firn column usually shows seasonal fluctuations in the upper part of the firn column and settles around the annual mean temperature at a depth of 10-15 m [e.g. Cuffey and Paterson, 2010]. To account for temperature variations throughout the firn column the heat transport is solved explicitly, using the one-dimensional heat-transfer equation [Cuffey and Paterson, 2010]:

$$\frac{dT}{dt} = \kappa \frac{d^2T}{dz^2} \tag{3.15}$$

with the thermal diffusivity κ and the depth *z*. Initially, the heat-transfer equation consisted of a term for heat conduction, advection and internal heating. However, internal heating is small within the firn layer and therefore neglected and the contribution of heat advection is taken into account by the downward motion of the ice flow [Cuffey and Paterson, 2010; Ligtenberg et al., 2011]. This method allows the temperature to be calculated individually for each layer at each time step.

Calculating the temperature explicitly is also necessary when incorporating the process of snowmelt and meltwater percolation, as heat is transported through the firn column [Ligtenberg et al., 2011]. Occasional snowmelt events may have a significant impact on the temperature and densification rate, as the freezing of liquid water fills up available pore space within the firn layer with the density of ice (917 kg m^{-3}). The amount of snowmelt, as taken from the RACMO2.1/ANT, is removed from the surface layer and percolated through the firn column. It refreezes in any layer with sufficiently cold temperatures and available pore space. This is modelled based on the "tipping-bucket" method, where water tips from one layer to the next [e.g. Kuipers Munneke et al., 2015] until it finds a layer with the required properties. The maximum pore space to store liquid water L_w is calculated as a function of snow porosity P_S and density, taken from Coléou and Lesaffre [1998] [Ligtenberg et al., 2011; Kuipers Munneke et al., 2015]:

$$L_w = 1.7 + 5.7\left(\frac{P_S}{1-P_S}\right) \tag{3.16}$$

with the snow porosity:

$$P_S = 1 - \left(\frac{\rho}{\rho_i}\right) \tag{3.17}$$

where ρ is the density of the layer and ρ_i the density of ice.

Finally, the vertical velocity, V_{fc}, of the surface due to firn compaction can be obtained (Equation 3.11) by integrating over the densification rate for the firn column [Helsen et al., 2008]:

$$V_{fc}(z,t) = \int_{z_i}^{z} \frac{1}{\rho(z)} \frac{d\rho(z)}{dt} dz. \tag{3.18}$$

3.3 Results

The initial model run is set up as described in the previous section. The results of my vertical velocity rates have been compared with the results of Ligtenberg et al. [2011] [Ligtenberg pers. comm., 2014] and show a very similar outcome, with some small differences primarily in the Antarctic Peninsula and along the east coast of Wilhelm II Land. With the densification rate depending on temperature and accumulation it is important to understand the sensitivity of both the densification process and the employed parameterisation to variations in the input values. This is especially important under the consideration that climate models predict different temperatures and accumulation rates across the ice sheet. By applying a bias to the input values used for the initial model run, the sensitivity of the firn compaction model, and thus of the rate of compaction, is studied, and conclusions on the impact of different firn compaction rates can be drawn.

The different biases I applied to the input values have been chosen based on research that has been undertaken to compare miscellaneous regional climate models with each other, as well as the validation of the RACMO2/ANT simulations with available observations. Bromwich et al. [2011] compared SMB simulations over Antarctica as simulated by various climate models. Differences of up to 30 mm yr^{-1} in the interior and up to 400 mm yr^{-1} in coastal areas have been found between the different models [Figure 2 in Bromwich et al., 2011]. The uncertainty of the SMB estimates of the RACMO2/ANT simulations are estimated to be 10 % [King pers. comm., 2015]. Therefore, I ran my sensitivity tests of the accumulation rate with a maximum bias of 10 %, and a smaller bias of 1 % and 5 %. The choice of applying a 1 % and 5 % bias was based on testing just how the model reacts to minimal fluctuations in the employed accumulation rate, while the maximum bias of 10 % will provide an understanding on the effect a large bias has on the model. The uncertainty for temperature simulations of the RACMO2/ANT model are found to be largely within ±10° K [Reijmer et al., 2005; Maris et al., 2012], while differences between the RACMO2/ANT simulations and other climate models differ by as much as ±12° K [Maris et al., 2012]. Therefore, I have chosen to run my temperature sensitivity test with an introduced bias of 1° K, 5° K and 10° K. The variable of near surface wind speed is only needed to estimate surface snow densities. However, simulating wind speed is challenging due to the strong katabatic and the RACMO2/ANT model is found to underestimate high and overestimate low wind speeds [Van den Broeke, 2008]. Compared to available observations across Antarctica the uncertainty of the simulated wind speed is found to be ±50 % for some observations [Reijmer et al., 2005; Lenaerts et al., 2012a]. However, the majority of the simulated values seems to be within ±10-20 % [Figure 4 in Lenaerts et al., 2012a]. Therefore, I only introduced a bias of 10 % to the near surface wind speed, to account for a more averaged uncertainty.

This section consists of four different parts. First I look at the sensitivity of the surface snow density parameterisation, which is estimated using near surface climate and provides the surface density of the top layer, which is used to begin the densification process. Afterwards I compare the results of the accumulation sensitivity test with the results of my initial model run and subsequently do the same with the temperature sensitivity test. The chapter is completed with an uncertainty estimation of the firn compaction model and a concluding discussion.

Surface snow density

At the surface, the density of freshly fallen snow varies with near surface temperatures, wind speed and accumulation rate, and is obtained using Equation (3.12). Figure 3.1 shows the spatial distribution of the modelled surface snow densities across the AIS. As the density depends on accumulation, temperature and wind speed, high densities are found along the ice sheet margins, where temperatures and accumulation rates are highest, gradually decreasing inland with the lowest densities found on the East Antarctic plateau.

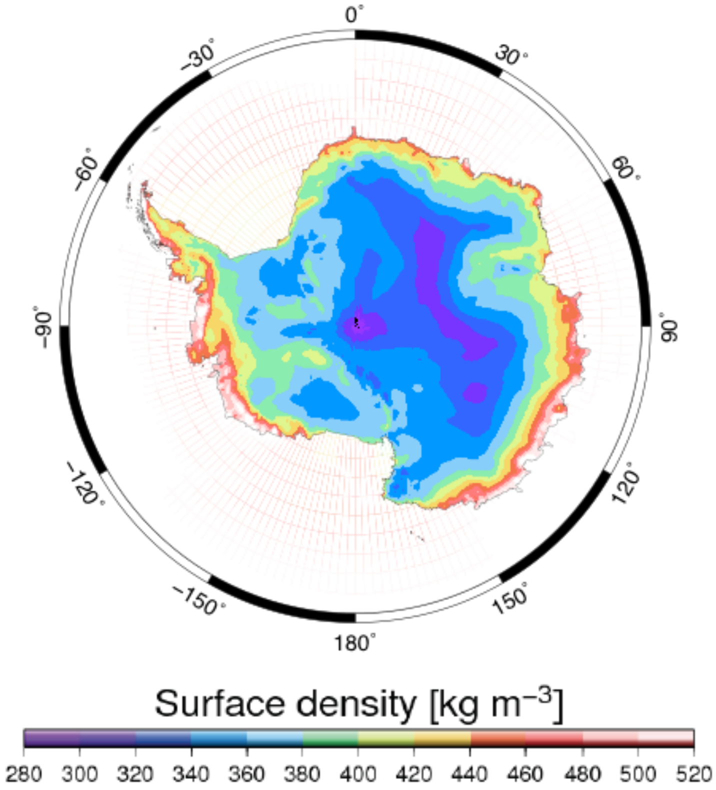

Figure 3.1: Spatial distribution of the modelled surface snow densities across Antarctica, based on the parameterisation of Kaspers et al. [2004].

With the surface snow density being dependent on average annual accumulation, average annual temperature and average annual wind speed, the computation is sensitive to variations of these input values. To obtain a better understanding of the sensitivity I applied a bias to each of the three variables, represented in Figure 3.2. Figure 3.2a shows the spatial distribution of the modelled surface snow density after applying a bias of 10 % to the average annual accumulation. Altogether density values across the ice sheet vary only slightly, with a small increase in surface snow densities mainly visible in the Antarctic Peninsula and along the margins of the WAIS and EAIS. Changes across the interior are not visible. Although accumulation rates generally have a great impact on surface snow densities, with high accumulation rates resulting in great densities, the modelled densities show little effect, with a slightly higher accumulation rate producing almost no changes across most of the interior. Figure 3.2b illustrates the sensitivity of the parameterisation to a bias in surface temperatures. I applied a bias of 10 K based on the findings of Reijmer et al.

[2005]. Likewise, this results in an increase of snow densities across the ice sheet but showing a much greater effect than variations in accumulation. Snow densities increase homogeneously by 15.12 kg m^{-3}, introduced by the parameterisation proposed by Kaspers et al [2004]. This not only shows that a bias in the mean temperature strongly affects the modelled snow densities, but also that seasonal temperature variations must have a significant impact on the surface snow densities throughout the year. Figure 3.2c shows the sensitivity of the modelled snow density to a bias applied to the average wind speed, where I employed a bias of 10 % to the input data. This results in slightly higher snow density values across most of the continent, with a smaller effect than a temperature bias, but a larger effect than the accumulation bias across the interior. Figure 3.2d shows the uncertainty in the modelled surface snow densities when all three biases are applied simultaneously. As expected, surface snow densities are higher everywhere, increasing by at least 20 kg m^{-3} in the interior and up to 40 kg m^{-3} in some areas at the ice sheet margins. In summary, larger snow densities are modelled across the ice sheet when applying a positive bias to the input values, while a negative bias applied to the input data results in a decrease of the density values of similar amplitude (not shown here). The sensitivity of the surface snow parameterisation is important, as this is the initial density that is used to start the density profile of the firn compaction model. While introducing a bias to the input values seem to have a rather small effect I will show later how important the modelled surface snow densities are when estimating the rate of firn compaction.

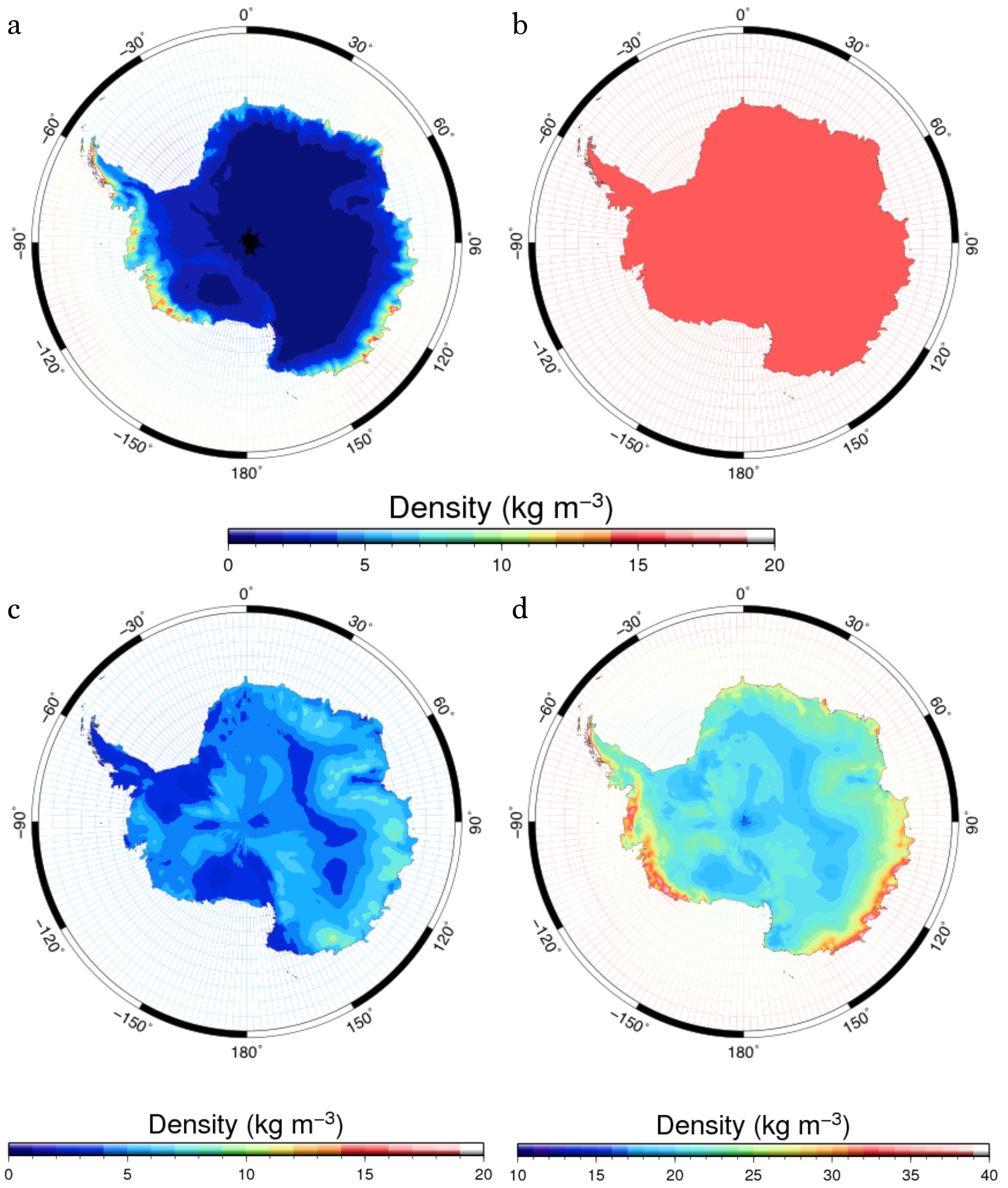

Figure 3.2a-d: Differences in the spatial distribution of the modelled surface snow density after introducing a bias of a) 10 % to the average annual accumulation, b) 10° K to the average annual temperature, c) 10 % to the average annual surface wind speed and d) all biases simultaneously. Note that the scale for d) is different.

In the following section I show the results of my firn compaction model (hereafter referred to as the initial model run), and compare the result of my initial model run with the model runs where I added biases to the accumulation and the temperature. Figure 3.3 illustrates the sensitivity of the model to changes in the accumulation rates and surface temperatures, showing density-depth profiles for two locations, a location in Marie Byrd Land and for the South Pole.

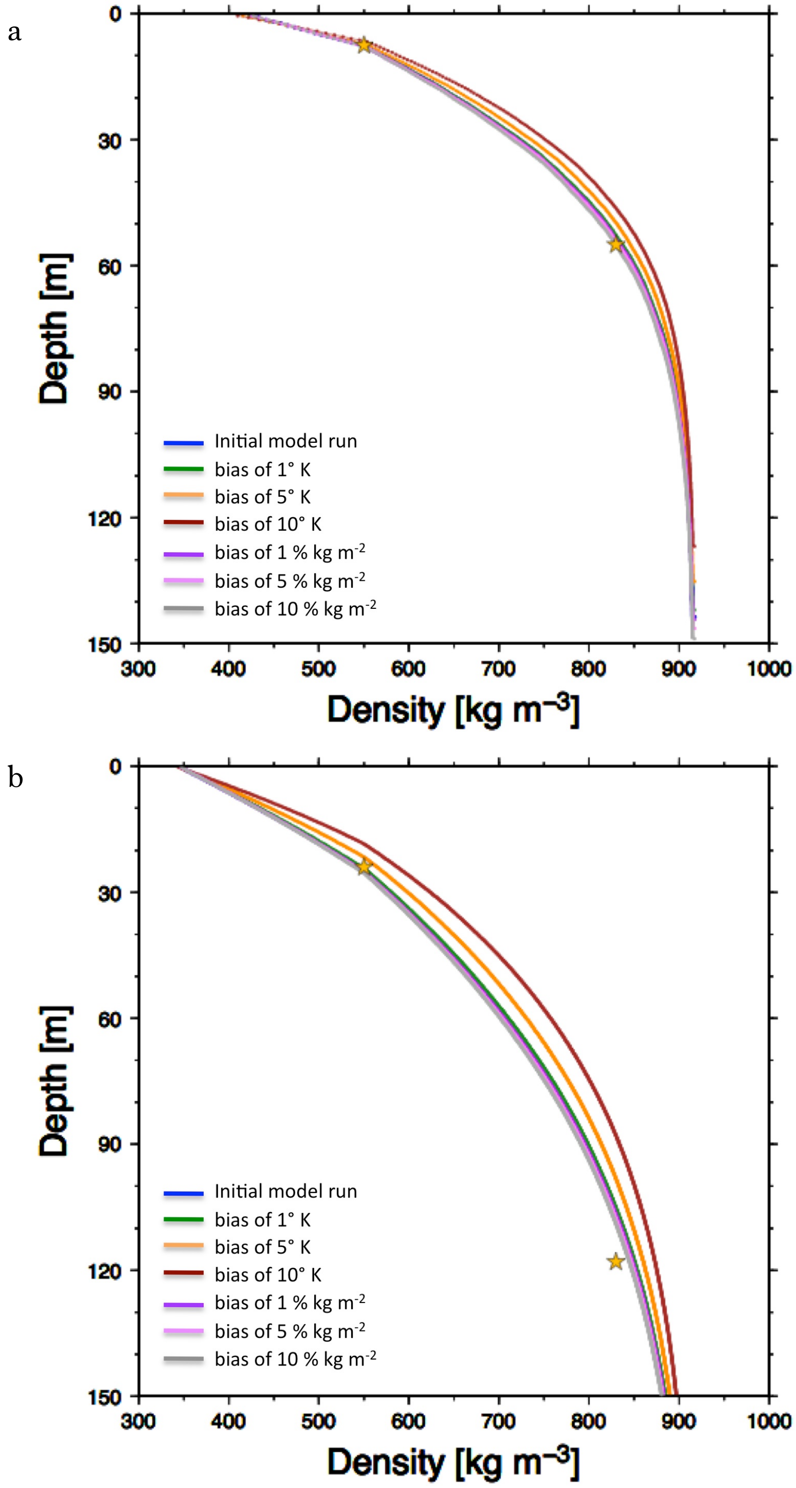

Figure 3.3: Firn density profiles for all models for a location in a) Marie Byrd Land and b) South Pole. The stars indicate the observed depth of the two critical densities of 550 and 830 kg m^{-3}.

The two locations have been chosen in order to compare with Ligtenberg et al. [2011], who presented those two locations [Figure 2.2 in Ligtenberg et al, 2011]. The figure includes the observed depths for the two critical densities of 550 and 830 kg m^{-3}, which are depicted by the two stars in Figure 3.3. Only small deviations can be observed for the location in Marie Byrd Land, with the greatest difference seen by the temperature deviations of 5° and 10° K. Greater differences are visible in the colder and drier climate of the South Pole, especially evident in the two temperature deviations of 5° and 10° K. On the other hand, variations in the accumulation rate seem to have no great effect on the densification rate in either locations.

Accumulation bias

In this section I assess the sensitivity of the firn compaction model to variations in the accumulation rate that is used to force the model, adding new layers at the surface and representing the weight of the overlying layers. As described earlier in this chapter, I apply a bias of 1 %, 5 % and 10 % to the accumulation rate. The maximal bias is chosen based on the uncertainty estimated for the SMB simulations of the RACMO2/ANT model [King pers. comm., 2015], while the smaller biases are chosen to investigate how sensitive the model reacts to fairly small changes that are quite likely to be present within climate model simulations. Figure 3.4a-d shows the average depth of the critical density of 550 kg m^{-3} for a) the initial model run and the accumulation variations of b) 1 %, c) 5 % and d) 10 %, and likewise for the critical density of 830 kg m^{-3} in Figure 3.5a-d. Only very small changes are visible between the initial model run in Figure 3.4a and the variated model runs in Figure 3.4b-d, showing a slight increase in the average depth of the critical density, best visible on the Antarctic Plateau. In Figure 3.5a-d, changes can be seen across the Antarctic Plateau, along the coastline of Terre Adelie and Wilkes Land, as well as along the margins of the WAIS. As for the depth of the 550 kg m^{-3} density, the depth of the 830 kg m^{-3} density slightly increased in most regions. This means that a slightly higher accumulation rate results in greater depths for the two critical densities.

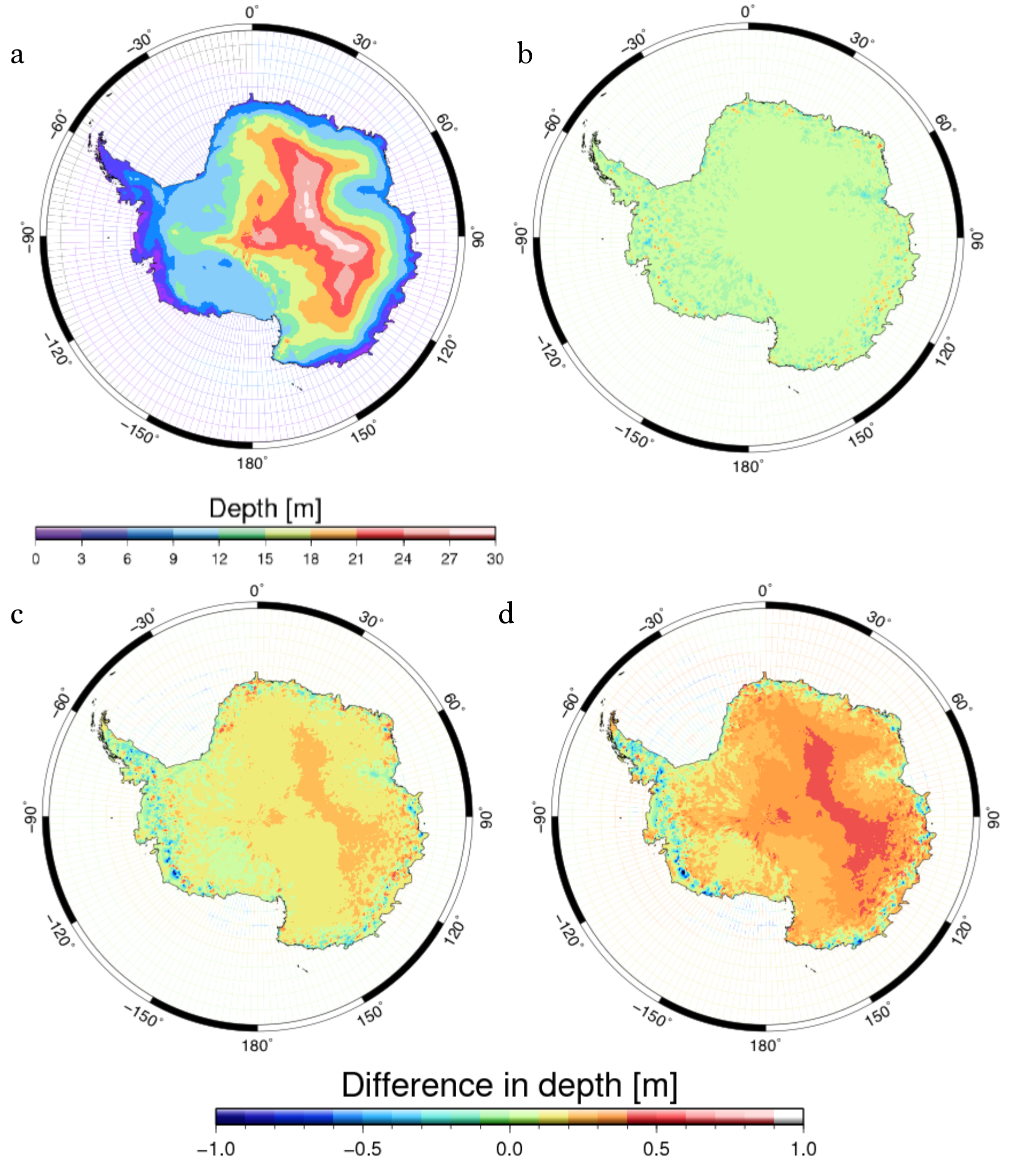

Figure 3.4a-d: Spatial distribution of the average depth of the 550 kg m^{-3} density for a) the initial model run and the differences from the initial model run for an accumulation variation of b) 1 % c) 5 % and d) 10 %.

While the greater surface load results in a faster densification, the added amount of material that is deposited results in thicker firn layers that bury previous layers faster, moving them to greater depths. This suggests that the effect that the accumulation has on the densification rate is offset by the added material, and that the depth of the critical densities solely increases because of the added layer thickness due to higher accumulation rates.

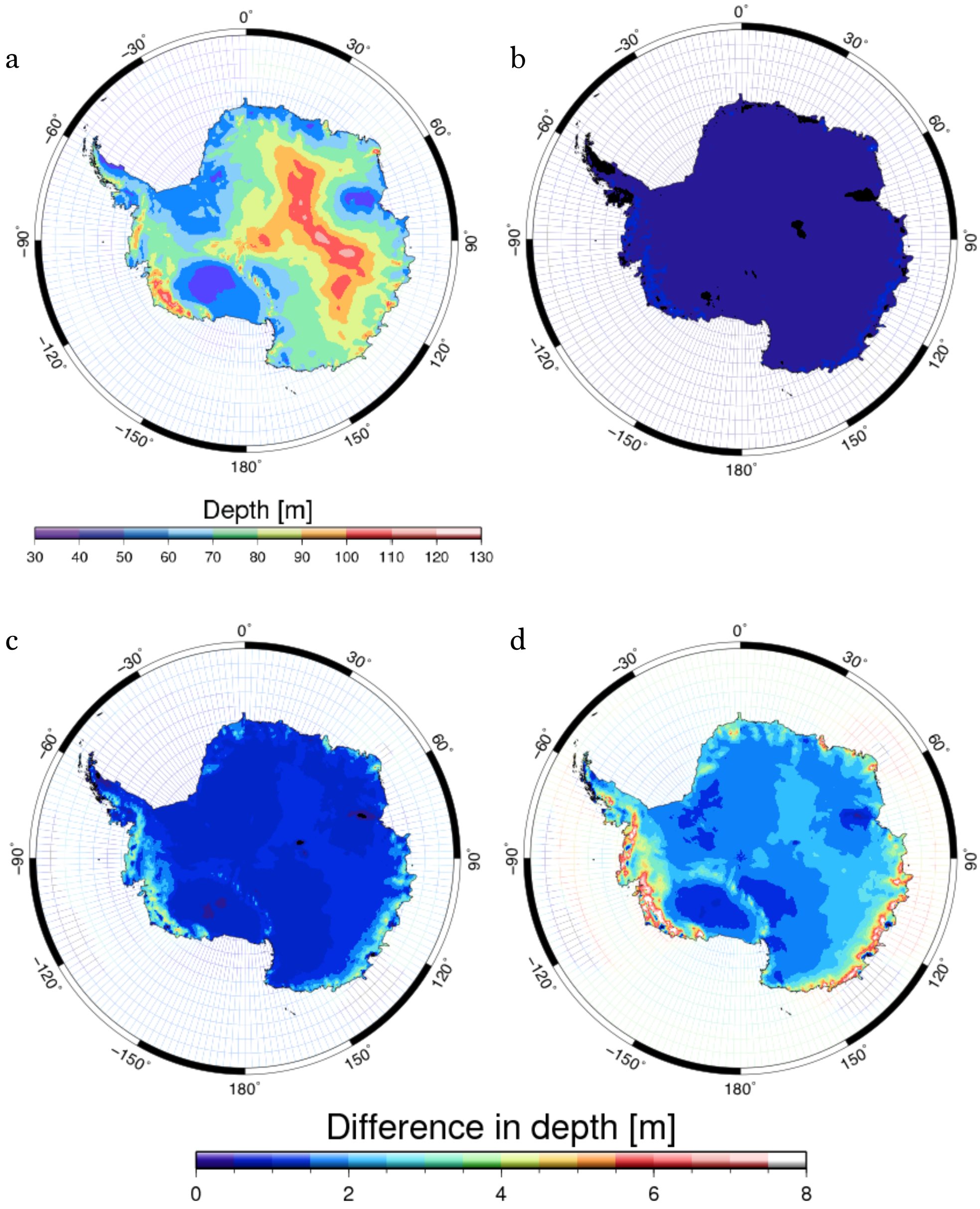

Figure 3.5a-d: Spatial distribution of the average depth of the 830 kg m^{-3} density for a) the initial model run and the differences from the initial model run for an accumulation variation of b) 1 % c) 5 % and d) 10 %.

Figure 3.6a shows the firn compaction velocity rate for the initial model run compared with the differences for each model run including an accumulation bias (Fig. 3.6b-d). For a bias of 1% and 5%, differences are primarily visible along the coastal margins of the WAIS and of the EAIS between 110° and 150° east (Fig. 3.6b-c), while differences of 5 cm yr^{-1} and more are observed along the ice sheet margins of the entire AIS for a bias of 10% (Fig. 3.6d).

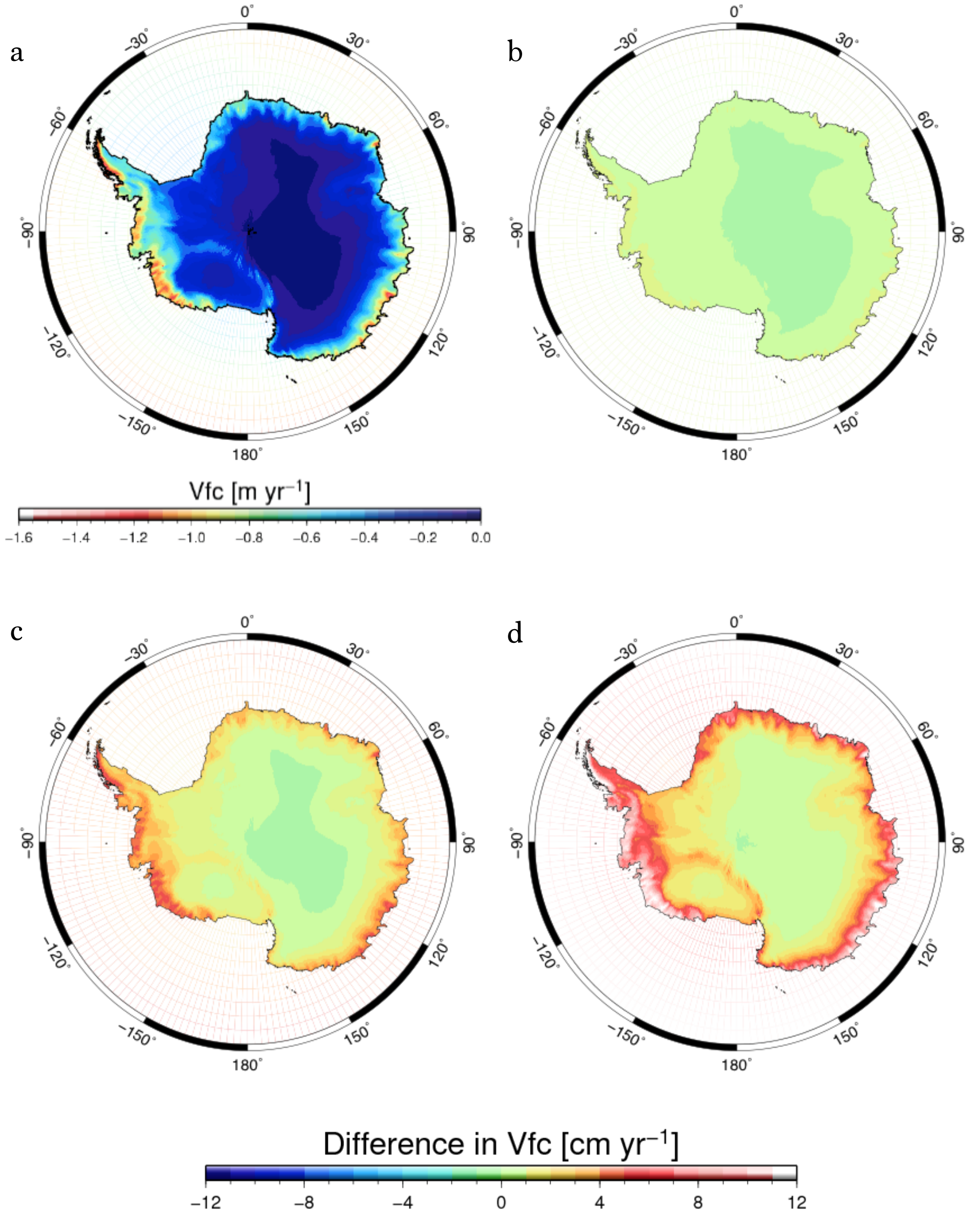

Figure 3.6a-d: Spatial distribution of a) the rate of the vertical velocity of the surface due to firn compaction as estimated with the initial model run, and the differences in the vertical velocity between the initial model-run and the accumulation variations of b) 1 % c) 5 % and d) 10 %. Note that the scale for a) is different to the scale used to represent the differences in b)-d).

Despite only minor changes in the spatial distribution in the depth of the two critical densities, surprisingly large discrepancies are seen in the vertical velocity of the surface due to firn compaction. While a bias of 1 % shows only small differences ranging between ±2 cm yr^{-1}, the differences become considerably larger with a 5 % and 10 % bias. The largest difference in

Figure 3.6c can be found at the ice sheet margins of the WAIS, showing differences of more than 12 cm yr^{-1}, with a maximum deviation of nearly 15 cm yr^{-1}. Thus, introducing a positive bias in the accumulation rate results in a larger vertical velocity of the surface than modelled in the initial model run. This confirms the assumption that the modelled depths of the critical densities solely increase due the added mass and not a slower densification rate. Contrarily, applying a negative bias to the accumulation rate would lead to the opposite effect, reducing the rate of firn compaction by a similar amount (not shown here).

Temperature Bias

Similar to assessing the model sensitivity to the accumulation rate, I assessed its sensitivity to temperature variations. As described earlier, I have chosen a maximum bias of 10° K based on the uncertainty findings of Reijmer et al. [2005] and Maris et al. [2012], who found that by RACMO2/ANT simulated temperatures are largely between ±10° K when compared to observations, and that the simulations differ by approximately ±12° K compared to miscellaneous climate models, respectively. To account for possible smaller temperature discrepancies, I also use two smaller biases, 1° K and 5° K.
Figure 3.7a-d shows the average depth of the critical density of 550 kg m^{-3} for a) the initial model run and the temperature deviations of b) 1° K, c) 5° K and d) 10° K, and likewise for the critical density of 830 kg m^{-3} in Figure 3.8a-d. It is clearly visible that there are differences in the spatial distribution of the critical depths because of the introduced bias. While a temperature difference of only 1° K results in similar densification rates for most of the ice sheet, some discrepancies are found on the Antarctic Plateau in East Antarctica, resulting in a faster densification rate and thus a shallower depths of the 550 kg m^{-3} density. A temperature bias of 5° K and 10° K (Fig. 3.7c and 3.7d) show a much faster densification rate across the entire ice sheet. This leads to a shallower depth distribution of the 550 kg m^{-3} density, showing a difference of more than ten metres in the interior and around three metres along coastal areas.

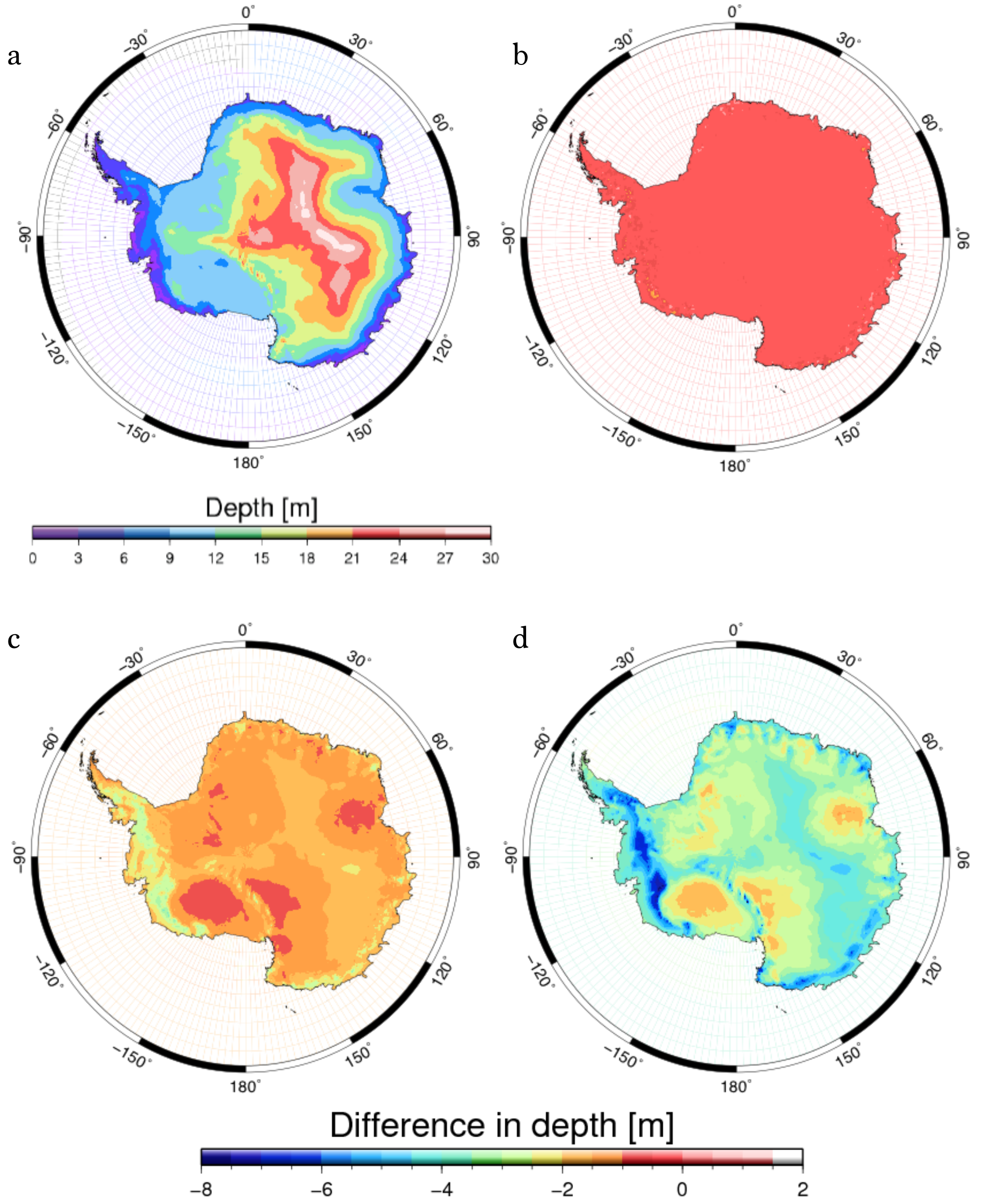

Figure 3.7a-d: Spatial distribution of the average depth of the 550 density for a) the initial model run and the differences from the initial model run for the temperature variations of b) 1° K, c) 5° K and d) 10° K.

A similar picture is found modelling the average depth distribution of the 830 kg m^{-3} density in Figure 3.8a-d, with variations in the distribution of the depth of up to 50 m in the cold interior and some parts of the ice sheet margin. Altogether, no depth greater than 60 m is found in Figure 3.8d, in comparison to 120 m in the initial model run. This agrees with Herron and Langway [1980], that firn densification occurs more quickly with warmer temperatures, and further verifies that the dry snow densification after Arthern et al. [2010] is sensitive to temperature variations.

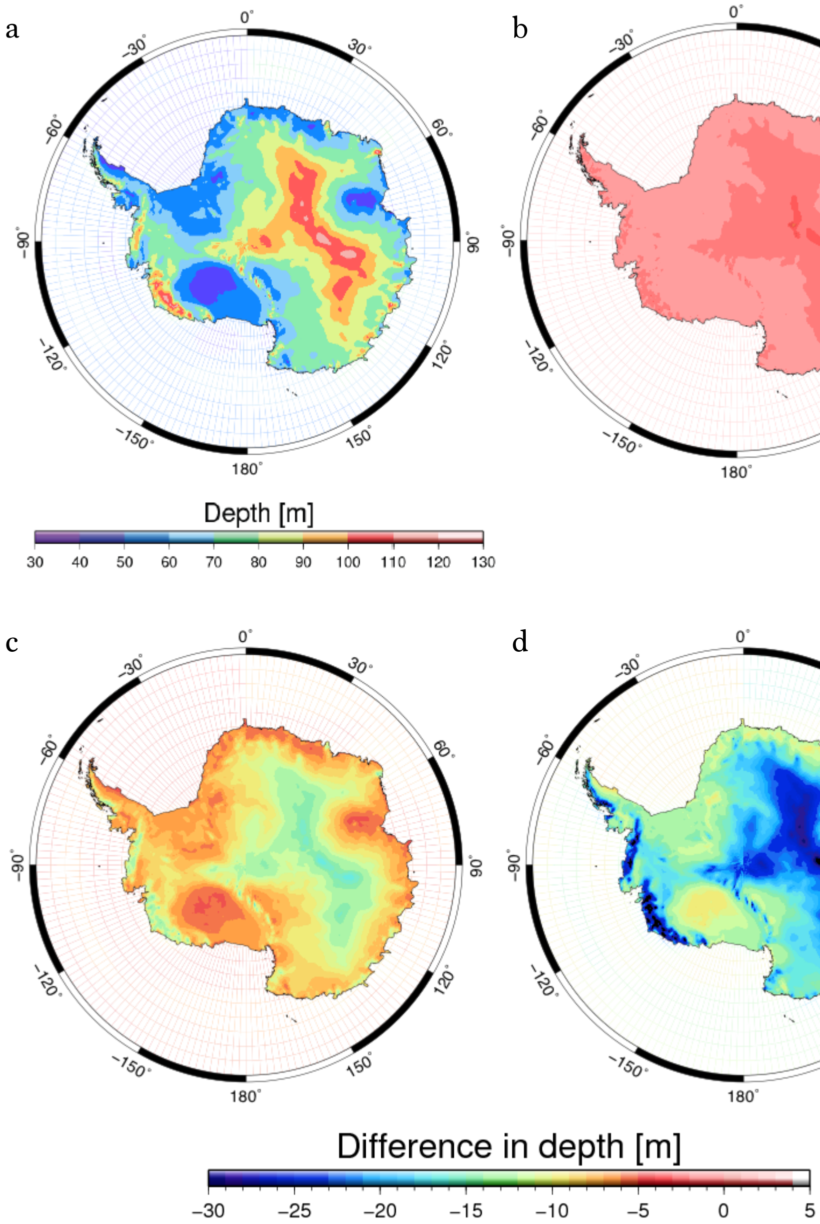

Figure 3.8a-d: Spatial distribution of the average depth of the 830 density for a) the initial model run and the differences from the initial model run for the temperature variations of b) 1° K, c) 5° K and d) 10° K.

Figure 3.9a-d compares the firn compaction velocity rate of the initial model-run with the differences of the temperature deviations, showing only small differences mainly between the initial model run and a temperature bias of 10° K (Fig. 3.9a and 3.9d). Although applying a temperature bias can alter the amount of snow melt as provided by RACMO2, it is found that adjusting the amount of snow melt has an insignificant effect on the final firn compaction rates, as melting events are rare.

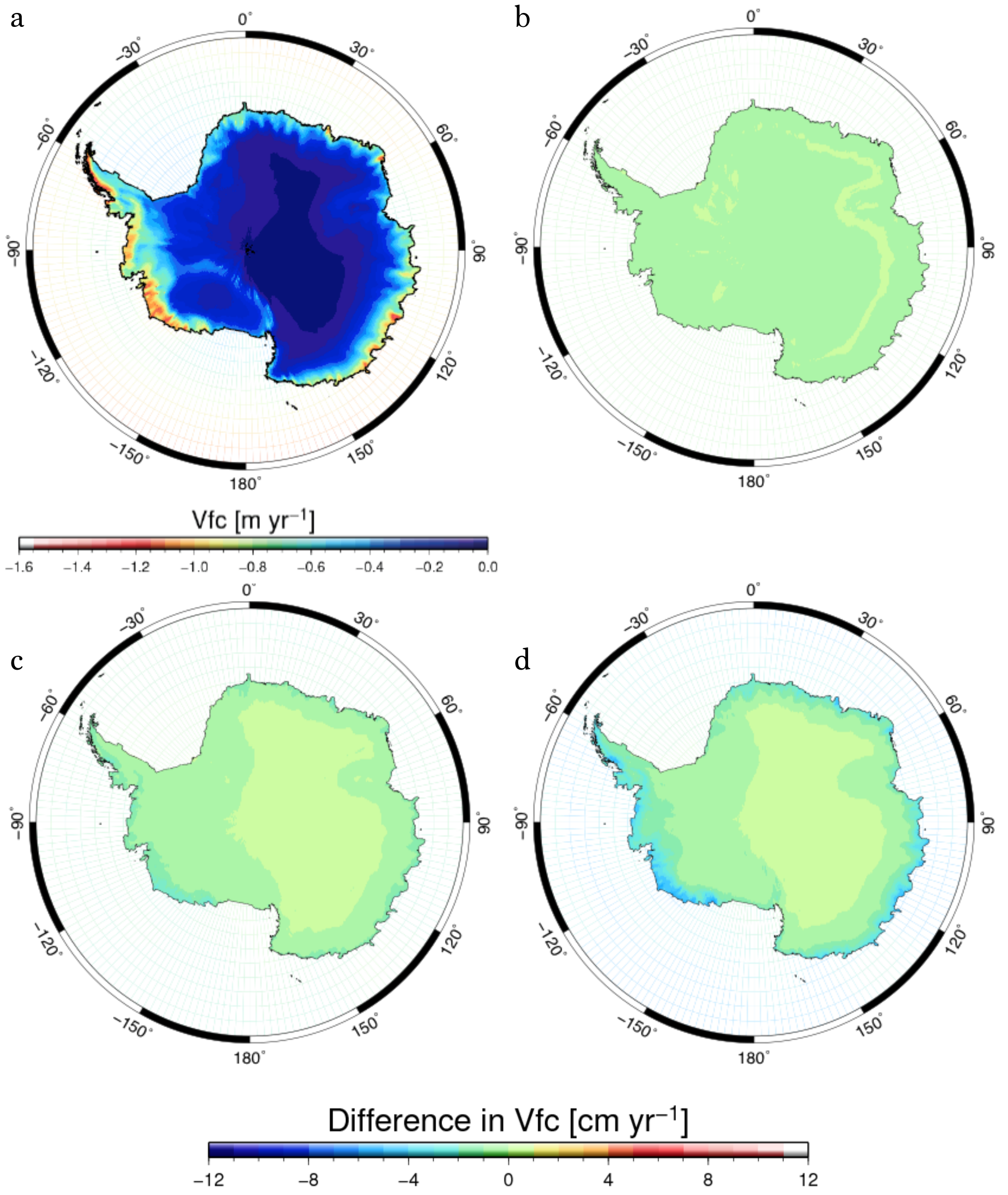

Figure 3.9a-d: Spatial distribution of a) the rate of the vertical velocity of the surface due to firn compaction as estimated with the initial model run, and the differences in the vertical velocity between the initial model-run and the temperature variations of b) 1 K c) 5 K and d) 10 K. Note that the scale for a) is different from the scale used to represent the differences in b-d), while the scale for b-d) is kept identical to the scale in Figure 3.6b-d to illustrate the variation in the differences.

The differences in the rate of the vertical velocity between the initial model run and a 1° K temperature variation is small and ranges between ±1 cm yr^{-1}. For the 5° K temperature variation the deviation gets larger and seems to get slightly faster in the interior (1 cm yr^{-1}) but decreases towards the coast, with a slower velocity rate of approximately -4 cm yr^{-1} at the coast of Marie Byrd Land in West Antarctica.

The largest discrepancies can be found between the 10° K temperature variation and the initial model run, ranging from +1 cm yr^{-1} in the East Antarctic interior, to -6 cm yr^{-1} along the coast of Marie Byrd Land. Interestingly, generally slower velocity rates are found, primarily along the ice sheet margins, despite a faster densification seen in the density-depth profiles (Fig. 3.3) and the spatial distribution of the two critical densities (Fig. 3.7 and 3.8). This can be explained by the fact that the faster densification rate leads to such fast compaction of the firn layers, that higher densities are reached quicker, resulting in more layers with high densities and therefore more layers with a slow densification rate.

The availability of augmented high-density layers may counteract the higher densification rate within the top layers when integrated over the entire firn column, thus resulting in overall slower firn compaction rates. This can also be seen in Figure 3.10, showing the average densification rate with depth for the same two locations shown in Figure 3.3. As expected, densification rates are largest in the top layers, and significantly greater when a positive temperature bias is applied. However, higher densities are reached faster for the model runs with an applied temperature bias. In particular, the model run with a bias of 10° K shows a very fast densification rate in the first 20 m for the location in Marie Byrd Land (Fig. 3.11a), before it reaches the first critical density of 550 kg m^{-3} and densification subsequently slows down. This is shown by the sharp drop in the densification rate, seen as a straight line. The model run with the 10° K bias is the first to reach the critical density, thus reaching a slower densification rate earlier than the other model runs. The depth difference between the 10° K bias run and the result of the initial model run is around ten metres for the critical density of 550 kg m^{-3} in Marie Byrd Land, and around 20 m at the South Pole (Fig. 3.10b). The densification rate at the South Pole also reflects a much faster rate within the top layers, with a generally fast drop to slower densification rates for all model runs simultaneously. Again, the rate for the model run with a 10° K bias shows a larger densification rate in the top layers before it reaches the 550 kg m^{-3} critical density much earlier than the other model runs, leading to a slower densification rate for most of the firn column. Naturally, the effect is greater in warmer regions near the ice sheet margins than in the cold interior, as the firn column builds up faster due to higher accumulation rates, simultaneously increasing compaction. This explains that, despite a faster compaction induced by warmer temperatures, the overall vertical velocity of the surface is smaller along the ice sheet margins for the model runs using a positive temperature bias, than for the initial model run estimates.

Uncertainty estimate

Modelling errors and uncertainties in the input data are the main error sources within the firn compaction model. The widely used regional climate model RACMO2/ANT is validated with observations where available; however, due to vast areas of Antarctica remaining unsampled by measurements, uncertainties remain in the model simulations. For SMB simulations, the uncertainty is estimated to be around 10 % [King, pers. comm. 2015], for temperature 10° K [Reijmer et al., 2005] and for wind speed 10-20 % [Lenaerts et al., 2012a]. Although Ligtenberg et al. [2011] validated their firn compaction model with 48 firn cores, uncertainties have not been addressed in their model.

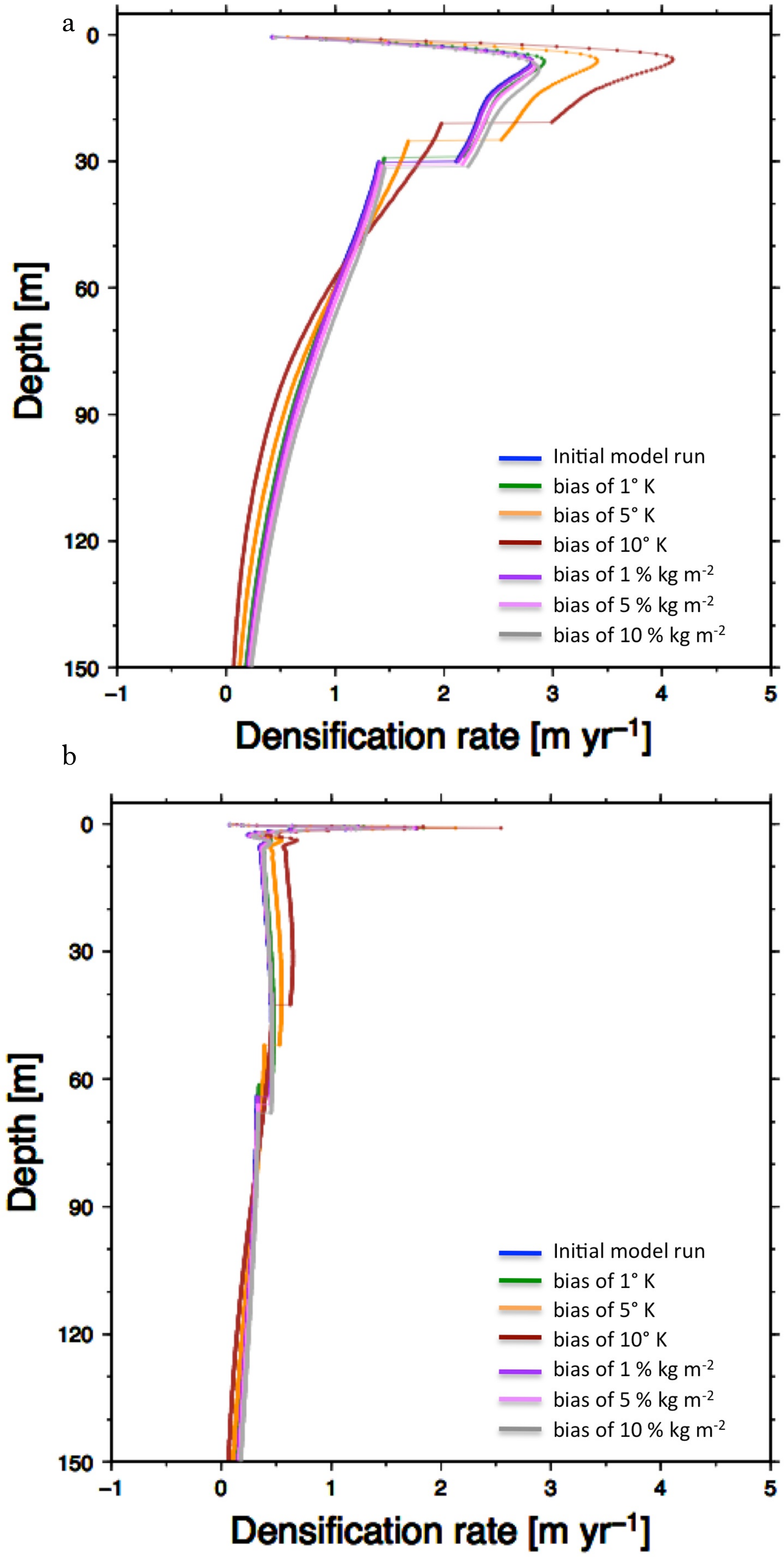

Figure 3.10a-b: Average densification rates for all models for a location in a) Marie Byrd Land and b) South Pole.

To represent variations of my firn compaction model results with regards to uncertainties within one regional climate model, and between different climate models, I apply a bias to the input values to assess the impact such differences have on the outcome of modelled firn compaction rates. In order to assess the uncertainties of my model I assume that these differences can be used to represent the uncertainty of my firn compaction model.

I use the results of my model runs with an applied bias of 1, 5 and 10 % to the accumulation rate and 1, 5 and 10° K to the temperature. Additionally, I include model runs using a bias of 1, -5 and -10 % and -1, -5 and -10° K, respectively. Furthermore, I applied a bias of 5, 10 and 20 kg m^{-3} and -5, -10 and -20 kg m^{-3} to the surface snow density. The maximal error for the snow density is taken as an average error from the sensitivity results of the surface snow parameterisation earlier in this section. The error introduced by near surface wind speed has been assessed within the uncertainty estimate of the surface snow density, as wind does not affect firn compaction. The results of the uncertainty estimates using the largest biases are shown in Figure 3.11a-f.

For each error source (accumulation, temperature and surface snow density) the standard deviation of all error runs is assessed individually, and shown in Figure 3.12a-c together with the propagation of the errors, to assess the total uncertainty estimate of the firn compaction model (Fig. 3.12d). Uncertainties are greatest along the ice sheet margins, with only minor differences across most of the interior. For the accumulation rate, the uncertainties range between ±12 cm yr^{-1}, with large differences visible across the Antarctic Peninsula and along the ice sheet margin of the WAIS and the EAIS, especially between 90°E and 150°E. For a positive accumulation bias a faster densification rate is observe, while a negative bias results in a lower densification rate.

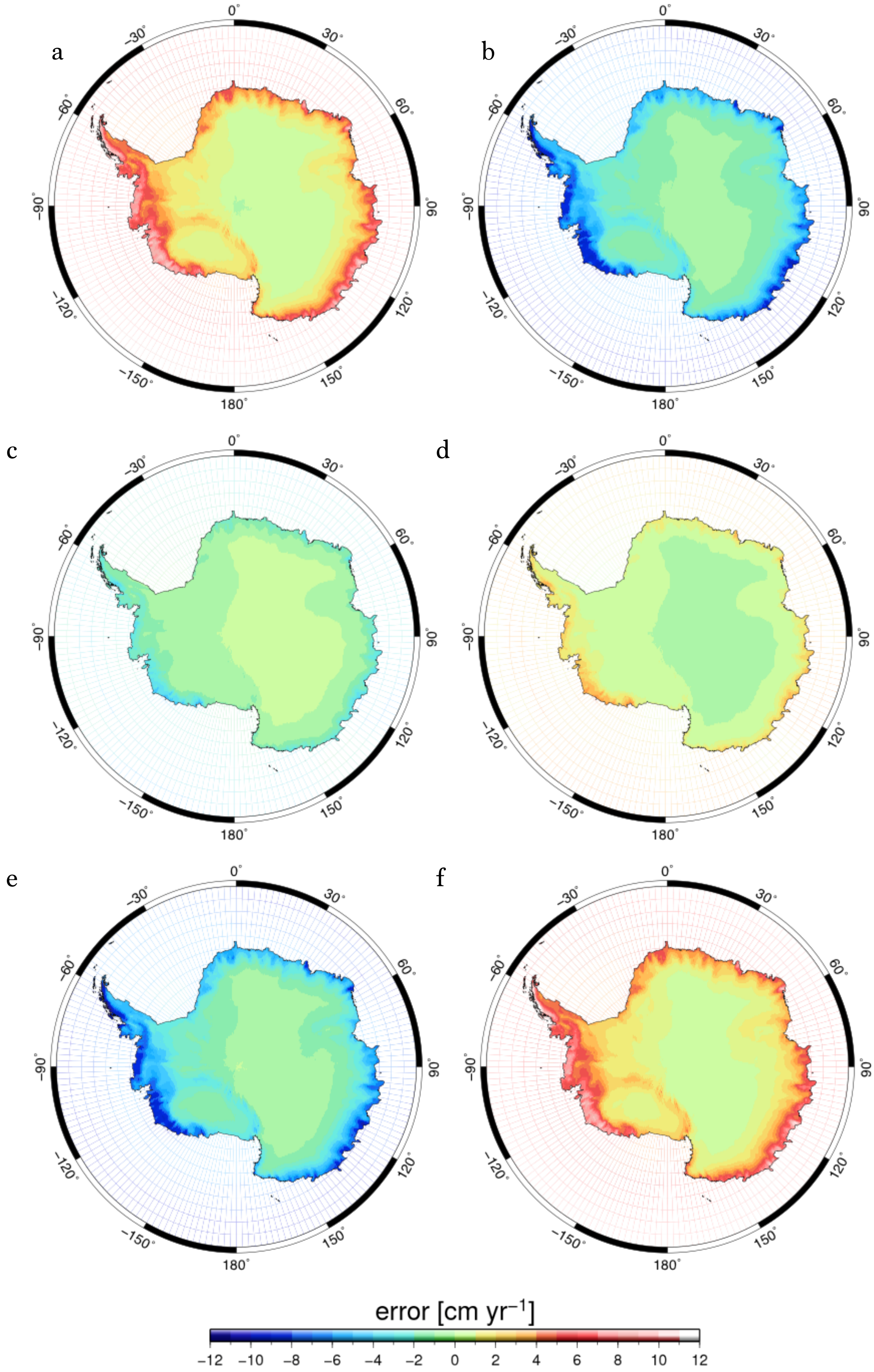

Figure 3.11a-f: Error estimates in regards to the initial model run for an introduced bias to the accumulation of a) 10 % and b) -10 %, an introduced bias to the temperature of c) 10° K and d) -10° K, and an introduced bias to the surface snow density parameterisation of e) 20 kg m^{-3} and f) -20 kg m^{-3}.

For the temperature and surface snow bias the result is reversed, with slower densifications rates found for a positive bias. The error of the temperature variations is smallest, with an uncertainty of ±4 cm yr^{-1}, while the error for the surface snow density is of a similar magnitude as for the accumulation, ranging between ±12 cm yr^{-1}.

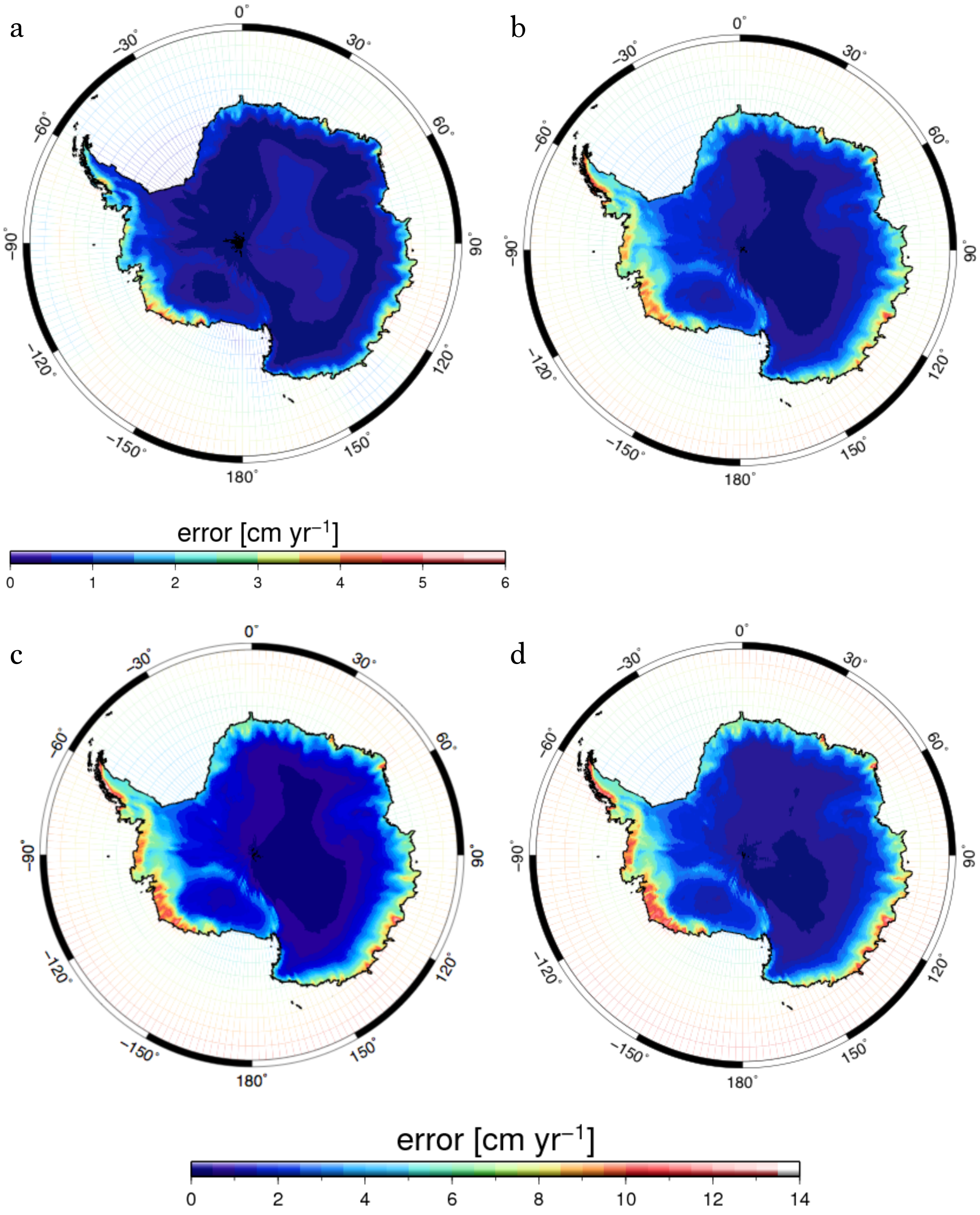

Figure 3.12a-d: Standard deviations of a) temperature, b) accumulation, c) surface snow density and d) the total error for the modelled firn compaction rates. Note the different scale for the temperature plot in a), due to it's smaller change.

The uncertainties shown in Figure 3.12a-c compare the estimated uncertainties of the individual error sources, with the largest errors found for the accumulation and surface snow density bias. In order to fully illustrate the range of the differences, a different scale is used than for the temperature bias, which shows a smaller deviation of 5 cm yr^{-1}. Generally, largest deviation are found along the ice sheet margins of Marie Byrd Land and at Law Dome in Wilkes Land near 112°E. Large areas along the WAIS and between 90° and 150°E of the EAIS show a standard deviation of 8 cm yr^{-1} or greater. The total error estimate in modelled firn compaction rates, as shown in Figure 3.12d, is greatest, with 13 cm yr^{-1}, at the Antarctic Peninsula along Graham Land (60°-70°W), along Marie Byrd Land in West Antarctica (100°-150°W) as well as around Law Dome and along the coast of Wilkes Land (110°-140°E).

3.4 Conclusion

The process of densification reduces the height of the firn layer that covers the ice sheet without there being any change in mass. This must be considered when interpreting satellite altimetry observations as a change in height might be simply due to compaction. However, modelling firn compaction is complex and the physical processes are still not fully understood. To investigate the importance of the densification process, I have developed a firn compaction model based on the numerical model scheme of Ligtenberg et al. [2011], using the dry snow densification expression of Arthern et al. [2010]. The surface layer of the firn column is driven by near surface climate simulated by the RACMO2.1/ANT regional climate model and the surface density is estimated by a parameterisation after Kaspers et al. [2004]. I used different accumulation and temperature sensitivities to model densification rates in the firn column and to assess the resulting differences in the vertical displacement of the surface. The accumulation rate is used to build up the firn layers at each time step and to represent the weight of the overlying layers pressing on the firn. The local temperature in each layer is calculated using a one-dimensional heat-transfer equation (3.15) to estimate temperature changes throughout the firn column. Subsequently, the initial model run was modified by applying a bias to the accumulation rate and surface temperature, adding 1, 5 and 10 % and 1, 5 and 10° K, respectively. Comparing the impacts of these variations on the densification rate provides a better understanding on the sensitivity of firn compaction models to the accumulation and temperature. This provides crucial information on the impact various firn compaction models have on analysing elevation observations and thus assessing ice sheet mass balance.

Significant differences can be found in the spatial distribution of the critical depths of the 550 kg m^{-3} and 830 kg m^{-3} densities, representing both faster and slower densification rates. Generally, the highest values are found in the cold interior of East Antarctica, where firn densification is a slower process due to the low temperatures and low accumulation rates. At the coastal regions the depth distribution is shallower due to a faster densification and higher surface densities. In West Antarctica and the Antarctic Peninsula, the 550 kg m^{-3} density levels are shallow, while the depth of the 830 kg m^{-3} density shows high values. This is due to the warmer and wetter climate with higher annual accumulation values and higher surface densities. The surface snow density along West Antarctica's coastline can reach up to 500 kg m^{-3} and is quickly buried due to regular snowfall, resulting in a slower densification with greater depth.

Running my firn compaction model with a temperature bias of up to 10° K demonstrates that the process of firn compaction is highly sensitive to surface temperature. This implies that estimating surface temperatures and understanding the temperature evolution throughout the firn layer is essential in order to accurately simulate firn compaction rates. Adding a positive degree bias to the initial temperature results in a faster densification rate, reaching the two critical densities quicker and therefore at shallower depths. On the contrary, reducing the initial temperature leads to a slower densification rate, increasing the depths at which the two critical densities are reached. Nevertheless, despite a faster densification rate the overall vertical velocity of the surface is actually lower than obtained in the initial model run. This can be explained by a fast densification rate leading to more layers of high densities with slower densification rates. Therefore, integrated over the entire firn column the overall rate of firn compaction is decreased for higher temperatures.

On the other hand, applying a bias to the accumulation rate shows the opposite effect, where the depths in which the critical densities are found increase slightly, suggesting a slower densification rate. However, integrated over the entire firn column the modelled vertical velocity of the surface indicates a faster densification rate by up to 12 cm yr^{-1}. This is likely to be because of the increased load of surface mass. Higher accumulation rates result in thicker layers that bury the firn layers quicker and move them into greater depths faster. Meanwhile, the overburden pressure results in a faster densification thereby offsetting the increased layer thickness. Integrated over the entire firn column the general densification increased. Understanding the effect a 10 % larger accumulation rate has on the densification rate demonstrates how large uncertainties might be if differences in the accumulation rate would be even greater. This is significant if we consider that some climate models simulate an accumulation that is ~50 % different compared to the RACMO2/ANT simulations [Bromwich et al., 2011; Maris et al., 2012].

In addition to the effects of temperature and accumulation on the firn compaction model, they also affect the estimates of the surface snow density. Together with a bias applied to the near surface wind speed, I tested the sensitivity of the surface snow density parameterisation. Individual variations are small, with the greatest impact caused by a temperature bias, which results in larger surface snow densities with differences of 15.12 kg m^{-3}. The effect this has on the densification rate estimates is considerable, with a slower densification rate of around ±12 cm yr^{-1}. This is similar to the difference found with the accumulation, which is likewise ±12 cm yr^{-1} depending on a positive or negative bias. The uncertainty obtained from the temperature variation is significantly smaller, ranging between ±5 cm yr^{-1}.

The uncertainty estimate of the modelled firn compaction rates was assessed by obtaining the propagated error of the standard deviations of the model differences based on accumulation, temperature and surface snow density. The greatest individual error source is the accumulation rate with a standard deviation of ±12 cm yr^{-1}. Together with smaller deviations for temperature and surface snow densities (~6 cm yr^{-1}), the total uncertainty of my modelled firn compaction rates is estimated to be between ±1 cm yr^{-1} in the interior and up to ±13 cm yr^{-1} in some coastal regions.

Chapter 4

Comparison of modelled and observed ice height and ice mass anomalies in Enderby Land, East Antarctica, and implications for ice dynamic rates

4 Introduction

Due to the continental size, isolated location and the surrounding ocean, the Antarctic continent has a strong impact on its own climate. Strong westerly winds and the Antarctic Circumpolar Current isolate the continent, leading to extreme climatic conditions. On average, Antarctica is the driest, windiest and coldest continent on Earth, where surface temperatures vary across the continent with a difference of 50-60 degrees Celsius between coastal areas and the interior. Typically, only the Antarctic Peninsula and coastal regions experience occasional melting events during the warmer months, while temperatures remain below freezing for most of Antarctica, throughout the entire year. Due to these low temperatures the interior does not receive much snowfall, while highest snowfall rates are recorded on the Antarctic Peninsula and along ice sheet margins. Despite low precipitation rates, snow regularly accumulates in many parts of the continent due to snow distribution as a result of the strong katabatic wind.

As described in Chapter 3, the AIS is covered by a firn layer up to 100 m thick in some regions of the ice sheet, consisting of annual layers of snowfall that accumulate on the ice sheet, constantly adding mass to the surface and compacting former layers beneath. The mass exchanges at the surface govern the budget of most glaciers and ice sheets [Cuffey and Paterson, 2010], with the ice body being in balance if mass input equals mass output. Therefore, the firn layer plays an important part when estimating ice sheet mass balance with the processes of mass accumulation, mass removal and displacement occurring on top of the firn column, and the processes of densification (compaction), meltwater percolation and refreezing inside the firn column.

Despite its own climate, rising global temperatures and warming oceans also have a large impact on the ice sheet, with current ongoing changes likely to increase in the future [e.g. Shepherd et al., 2012]. Therefore, understanding surface mass balance and ice dynamics is essential when estimating present-day ice mass balance. While the overall mass balance of the AIS is declining, with the West Antarctic Ice Sheet and the Antarctic Peninsula showing accelerating losses in ice mass, the East Antarctic Ice Sheet appears to be largely in balance [e.g. Shepherd et al., 2012].

Assessing and understanding surface mass balance of the AIS is challenging due to the remoteness and extensive ice cover of the continent, together with its harsh climate. The sparse network of atmospheric observations to provide a sound knowledge about the present-day climate, and the lack of field observations to provide information about present-day and past climate, make it difficult to establish well constrained models for Antarctica. Despite an increasing availability and improving analyses of satellite observations to obtain temporal spatial changes in ice mass and ice volume, large uncertainties remain when interpreting the signals and assigning the origin of the change. Both altimetry and GRACE observations detect signals from variations in surface mass balance as well as crustal movements due to glacial isostatic adjustment (GIA). Moreover, topographic changes are also induced by the densification of snow, causing a change in ice height seen by altimeters, without an actual change in mass. Without well constrained models the challenge remains to correctly interpret the satellite measurements, relying on a sparse network of in-situ measurements and model simulations to assign recorded changes in elevation and mass to the correct process.

The aim of this Chapter is to compare GRACE and ICESat altimetry observations using the regional climate model RACMO2/ANT to model surface mass balance (SMB) and firn compaction rates and, consequently, to obtain ice dynamic rates.

Due to the different spatial resolutions of the two geodetic techniques, a direct comparison is difficult. While the altimetry observations have a high resolution (~60 m laser footprint and 172 m along-track spacing), different techniques are used to interpolate between the altimeter tracks and to incorporate a slope correction for the ice sheet topography. For this study the ICESat estimates of Hoffmann [2014] are used (see Chapter 2, Section 2.2 for a detailed description). On the other hand, the mass variations derived from GRACE observations are represented using spherical harmonics up to degree and order 80 and the satellite footprint is ~250 km, resulting in a smoother signal on a wider scale. Here I use the release 3 solutions from GRGS (see Chapter 2, Section 2.1 for a detailed description).

By comparing my modelled rates of elevation change with observations from ICESat I obtain an estimate for ice dynamic rates (V_{ice}^{ICESat}). I repeat this step for ice mass measurements, using my modelled SMB estimates to obtain ice dynamic rates from the GRACE measurements (V_{ice}^{GRACE}). Subsequently I use my obtained ice dynamic rates, V_{ice}^{ICESat} and V_{ice}^{GRACE}, to model height and mass anomalies, thus comparing the ICESat and GRACE observations with my modelled anomalies.

4.2 Study site

As mentioned earlier, an increase in mass has been recorded along most of the East Antarctic coast, with the strongest signal being observed in Enderby Land, between 30°E and 70°E. The recorded mass anomaly is of interest not only because of its strong positive signal but also due to its time series that shows a discontinuity in the positive mass trend (see Section 4.4.1) and the question arising whether this was due to changes in SMB rates, GIA uplift rates or, potentially, a combination of both.
Unfortunately, field observations to validate these findings or to support available models (e.g. regional climate models, GIA models) are very sparse in this region. A GPS station has been installed at Richardson Lake in Enderby Land (Figure 4.1), however, observations spanned only a period of 1.2 years (2007.0-2008.2) before the equipment failed [Tregoning et al., 2009]. During the 1.2 years of available GPS measurements no significant uplift or subsidence was recorded by the GPS station. The question about the potential source of the gravity anomaly signal remains.

Although my study area includes Kemp Land and Mac. Robertson Land and parts of Donning Maud Land and Princess Elizabeth Land, the region is hereafter referred to as Enderby Land for simplicity (Figure 4.1). In this region, the AIS is predominantly located on bedrock above sea level, and surface elevation and ice thickness range from zero to approximately 3000 m [Fretwell et al., 2013]. The only research stations in this area are Syowa (Japan), Molodezhnaya (Russia) and Mawson (Australia) (Figure 4.1) and in-situ observations on surface climate, snowpack and ice flow are extremely sparse [e.g. Ligtenberg et al., 2011; Lenaerts et al., 2012]. The lack of in-situ geological measurements also affects the prediction of GIA uplift rates. Estimates across the regions vary from ~1 to 3 mm yr^{-1} (Chapter 1, Section 1.4) [Whitehouse et al., 2012b; Ivins and James, 2013; Peltier et al., 2015].

Apart from the Lambert and Fisher glaciers at the Amery Ice Shelf, only small glaciers are found along the Enderby Land coast. Previous research found that ice velocity rates are rather small for most of the area (Figure 4.1), with the ice sheet found to be largely in balance around Enderby Land [Rignot et al., 2008; Allison et al., 2009]. Rignot [2002] found that the condition of the Shirase Glacier, the largest within my study region besides the Lamber Glacier, is close to mass balance. Near the grounding line, the glacier flows down a narrow trench at 2400 m yr^{-1} and discharges around 15.1 ± 3 km^3 ice yr^{-1}, only 1.8 ± 3 km^3 yr^{-1} less ice than the calculated balance flux [Rignot, 2002]. The Rayner and Thyer Glaciers to the east are found to be in balance (+0) and the Lambert Glacier is slightly negative with an average snowfall of ~54.5 km^3 yr^{-1} integrated over the area around the glacier, and a cumulative outflow of ~57.5 km^3 ice yr^{-1} (-3) [Rignot and Thomas, 2002]. These findings are supported by former altimeter observations from ESA-1/2, with no significant elevation changes observed between 1992-1996 [Wingham et al., 1998; Rignot, 2006].

Rignot [2006] also found no change in ice velocity during 1996-2000 for the Lambert-Mellor-Fischer Glaciers (hereafter combined as Lambert Glacier). The updated map of ice velocities by Rignot et al. [2008] now includes the main glaciers of Enderby Land and, overall, East Antarctica is found to have a near zero mass balance. The Lambert basin, including the Lambert glaciers, the American Highland glaciers and Scylla Glacier, is found to remain in near balance. The glaciers Shirase, Rayner and Thyer, and Robert are combined in the sector for Enderby Land, likewise showing a net balance, possibly even slight thickening in this area. The Shirase Glacier accounts for most of the ice discharge in the Enderby Land sector, with an estimated outflow exceeding accumulation by 7 Gt yr^{-1}. However, for the Robert, Rayner and Thyer Glaciers, mass input exceeds ice discharge, resulting in the overall balance being near zero in the sector for Enderby Land [Rignot et al., 2008].

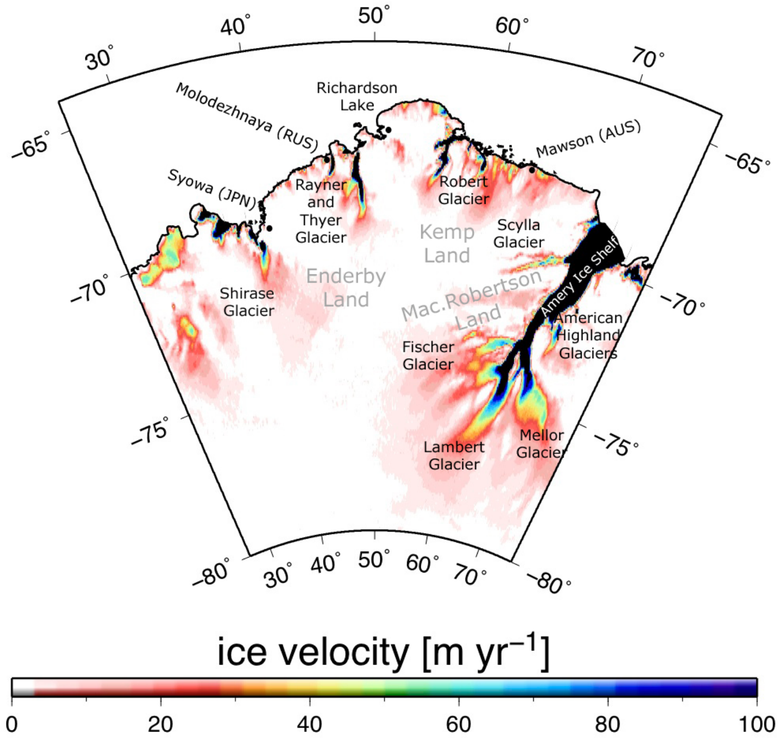

Figure 4.1: Regional map showing the study site in Enderby Land and important locations and glaciers. Ice velocities sourced from the NASA MEaSUREs program [Rignot et al., 2011; Mouginot et al., 2012] are plotted.

4.3 Method

Elevation changes and mass changes as seen across an ice sheet are primarily affected by surface mass balance, ice dynamics and ice discharge processes, but also by isostatic adjustment of the lithosphere due to the redistribution of mantle material as well as the initial elastic response of the lithosphere to changing loads. While only SMB and ice discharge affect changes in ice mass, the process of firn compaction can have a strong effect on surface elevation changes, as described in Chapter 3. As previously shown in Chapter 2 (Eq. 2.5), the general change in height at the surface can be expressed as:

$$\frac{dH}{dt}=\frac{dH^{SMB}}{dt}+\frac{dH^{fc}}{dt}+\frac{dH^{ice}}{dt}+\frac{dH^{GIA}}{dt}+\frac{dH^{elast}}{dt} \tag{4.1}$$

where dH^{SMB}/dt represents the change in elevation due to the components that affect surface mass balance, divided by the density of snow to obtain the rate of change in snow height equivalent. dH^{fc}/dt is the change in elevation due to firn compaction, dH^{ice}/dt ice dynamics, dH^{GIA}/dt GIA and dH^{elast}/dt the elastic deformation of the lithosphere. The process of firn compaction only affects ice thickness but not ice mass, and is therefore not relevant for mass variations. Thus, the general change in mass can be expressed as:

$$\frac{dM}{dt}=\frac{dM^{SMB}}{dt}+\frac{dM^{ice}}{dt}+\frac{dM^{GIA}}{dt}+\frac{dM^{elast}}{dt} \tag{4.2}$$

with the change in mass due to SMB (dM^{SMB}/dt), ice dynamics (dM^{ice}/dt), GIA (dM^{GIA}/dt), and the elastic deformation (dM^{elast}/dt) respectively.

If the assumption is made that elevation and gravity changes observed by satellites only contain ice sheet mass balance variations, and the effects of firn compaction and GIA have no effect on the observations, the recorded change in height and mass would be related only to snowfall (mass input in the form of SMB) and ice dynamics (mass output in the form of ice discharge). When SMB and ice dynamics are of the same magnitude, the ice sheet is in balance and GRACE would not detect a change in mass. However, if the amount of snowfall is larger than ice discharge GRACE would observe an increase in mass, and vice versa if ice discharge is greater than accumulation. Although the same principle applies to the altimetry observations, the contribution of surface elevation changes due to firn compaction can contaminate the signal and a positive mass balance can be detected as a negative change in elevation due to the compaction of the firn layer.

The final process that affects elevation change and mass variations is the vertical movement of the lithosphere due to the distribution of mantle material as a result of GIA. In Enderby Land estimated GIA rates are small at ~1-3 mm yr^{-1} [Whitehouse et al., 2012; Ivins and James, 2013; Peltier et al., 2015], with a total uplift of 7-20 mm during 2003-2009 (Chapter 1, Section 1.4). GIA may have a negligible effect on altimetry measurements, where height uncertainties can reach up to ~200 mm yr^{-1} near ice sheet margins, but has a significant effect on GRACE-derived mass anomaly estimates. Nevertheless, both GRACE and ICESat observations are corrected for GIA uplift rates using the ICE-6G_C (VM5a) model of Peltier et al. [2015] (hereafter referred to as ICE-6G).

4.3.1 Estimating V_{ice} from ICESat measurements

With SMB estimates provided by the RACMO2/ANT simulations, firn compaction rates obtained with my semi-empirical firn compaction model, and GIA uplift rates taken into account using the ICE-6G model, the remaining unknown in mass balance is the variable of ice dynamics. With ice dynamic rates found to be largely in balance across the Enderby Land region [Rignot, 2006; Rignot et al., 2008], elevation changes due to ice dynamic rates should equal elevation changes due to SMB, and would reveal any positive or negative SMB anomalies should a positive or negative signal remain. The approach suggested here is to compare the modelled trend in elevation due to SMB and firn compaction with the observed elevation rates obtained with ICESat, thus obtaining the rate of elevation change due to ice dynamics.

In order to model the change in elevation (dH^{SMB}/dt) over the period 2003-2010, I first combine monthly accumulation, sublimation, evaporation, snowdrift and snowmelt events from the RACMO2/ANT model (in mm w.e. yr^{-1}), to obtain the actual change in surface mass balance. I then estimate the surface snow density using the parameterisation after Kaspers et al. [2004] in combination with the slope correction after Helsen et al. [2008] (Equation 3.12), and divide the monthly SMB by the density of snow to convert to snow equivalent (m mth^{-1}). I obtain monthly elevation changes based on SMB and firn compaction by subtracting the vertical displacement of the surface due to compaction (dH^{fc}/dt) from the snow layer.

The trend of the cumulated monthly changes in elevation is calculated over the period 2003-2010 to obtain the rate of elevation change due to variations in SMB and firn compaction.

I now remove my modelled elevation change from the uncorrected ICESat observations (dH^{ICESat}/dt) to obtain an estimate of ice dynamic rates (V_{ice}^{ICESat}):

$$V_{ice}^{ICESat} = \frac{dH^{ice}}{dt} = \frac{dH^{ICESat}}{dt} - \frac{dH^{SMB}}{dt} - \frac{dH^{fc}}{dt} - \frac{dH^{GIA}}{dt} \quad . \tag{4.3}$$

If ice sheet mass balance indeed has not changed in Enderby Land since 2006, as previously proposed by Rignot et al., [2008], and the ice sheet is still in near balance (SMB ≈ V_{ice}), V_{ice} should correlate with the average annual SMB and allow to obtain elevation anomalies:

$$\frac{dH^{anomaly}}{dt} = \frac{dH^{SMB}}{dt} - \frac{dH^{ice}}{dt} . \tag{4.4}$$

4.3.2 Converting V_{ice}^{ICESat} into mass equivalent

To be able to assess ice sheet mass balance variations, observed elevation changes need to be converted into mass changes using the density of the ice sheet at each location. The general equation to convert from elevation changes (dH/dt) into mass changes (dM/dt) is given by:

$$\frac{dM}{dt} = \frac{dH}{dt} \rho_{AV} \tag{4.5}$$

where ρ_{AV} represents the average density of the firn/ice column [Zwally et al., 2005]. Helsen et al. [2008b] used the same equation, selecting the density value depending on whether the volume changes are due to accumulation (surface snow density) or due to ice discharge (glacier ice density). Apart from a few locations in West Antarctica they primarily used snow densities and found that the snow density leads to an underestimation of dM/dt, while the density of ice leads to an overestimate. Moreover, with the density evolution not well known, large uncertainties can be introduced when converting dH/dt to dM/dt [Sutterley et al., 2014]. Here I use an average density of the firn and ice column at each location, which I obtained during the spin-up of my firn compaction model (see Chapter 3), and multiply this density by dH/dt. The process of obtaining my ice dynamic rates is shown diagrammatically in Figure 4.2.

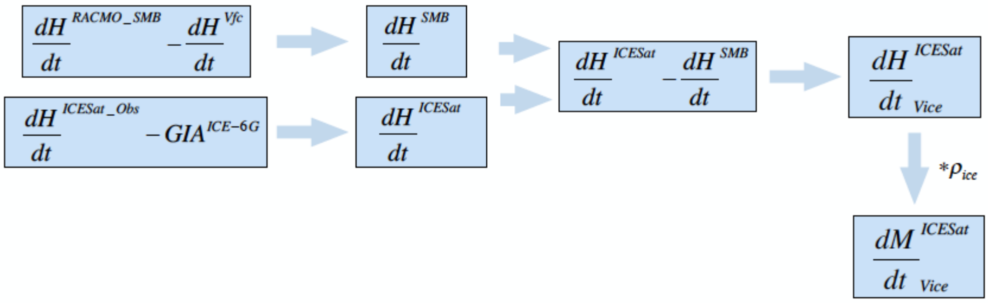

Figure 4.2: Flow chart to illustrate the individual steps to obtain ice dynamic rates from ICESat observations and modelled SMB and firn compaction rates.

4.3.3 Estimating V_{ice} from GRACE measurements

The GRACE mission monitors spatial and temporal variations in mass between the satellite and the centre of the Earth. Recorded changes in mass can be related to SMB, ice discharge over the grounding line (thereafter, the floating ice is isostatically compensated by the ocean, having no effect on the gravity field) and GIA due to the redistribution of mantle material. The process of firn compaction only affects ice thickness but not ice mass, and is therefore not relevant for GRACE. With the GRACE signal primarily representing ice sheet mass balance variations and GIA, removing GIA and the change in SMB from the GRACE observations should yield ice dynamic rates, comparable to the method applied to the ICESat observations:

$$V_{ice}^{GRACE} = \frac{dM^{ice}}{dt} = \frac{dM^{GRACE}}{dt} - \frac{dM^{SMB}}{dt} - \frac{dM^{GIA}}{dt}. \tag{4.6}$$

In order to obtain dM^{ice}/dt from the GRACE observations, I modelled the trend in SMB over the same duration as taken previously: 2003-2010, covering the ICESat observational period. The GRACE mass anomalies are calculated using Equation 2.2 in Section 2.1.3, and are expressed in equivalent water height to represent surface mass balance. To compare surface mass balance as simulated by the RACMO model, the trend of cumulated monthly SMB estimates is obtained. The SMB components are provided in kg m^{-2} yr^{-1}, which is equivalent to mm yr^{-1} in water equivalent (when divided by the density of water: 1000 kg m^{-3}). Finally, I remove the GIA component from the GRACE observations using the ICE-6G deglaciation model [Peltier, et al., 2015] and repeat my previous steps to obtain an estimated change in mass due to ice dynamic rates, after correcting mass anomalies for isostatic adjustment.

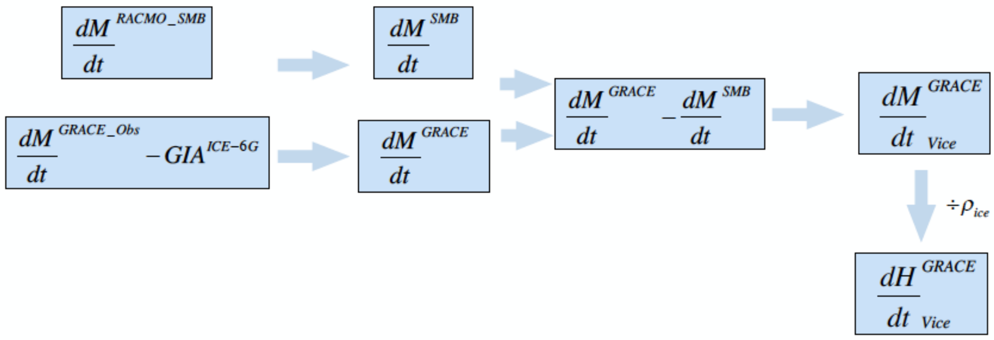

Figure 4.3: Flow chart to illustrate the individual steps to obtain ice dynamic rates from GRACE observations and modelled SMB rates, and converted into a change in height.

4.3.4 Comparing ICESat and GRACE trends

If altimetry and GRACE record the same signal, detecting positive or negative height and mass anomalies, respectively, the obtained V_{ice}^{ICESat} estimates should correlate after converting from height to mass using density values. Moreover, removing ice dynamic estimates, derived from the surface elevation model, from the modelled SMB trend should approximate the GRACE observations:

$$\frac{dM^{GRACE}}{dt} = \frac{dM^{SMB}}{dt} + \left(V_{ice}^{ICESat}\rho_i\right) \tag{4.7}$$

with the ice dynamic rates V_{ice}^{ICESat} obtained from dH^{ICESat}/dt and ρ_i the density of ice. Consequently, dividing V_{ice}^{GRACE} by the ice density, V_{ice}^{GRACE} should correlate with my V_{ice}^{ICESat} estimates, and result in similar height anomalies:

$$\frac{dH^{ICESat}}{dt} = \frac{dH^{SMB}}{dt} - \frac{V_{ice}^{GRACE}}{\rho_i}. \tag{4.8}$$

The results of my obtained ice dynamic rates from GRACE and ICESat, and the comparison, are given in Section 4.4.

4.3.5 Uncertainties

Measurement and processing errors remain in the GRACE solutions, along with propagating formal errors in the mathematical equation that is used to estimate the Stokes coefficients [Bruinsma et al., 2010]. Moreover, errors remain in the correction of the solutions for the effects of ocean tides, atmospheric pressure fields and barotropic ocean response (Chapter 2, Section 2.1). When represented in equivalent water height, the error of the GRACE signal is expected to reduce towards the polar regions due to denser ground track coverage and is estimated to be around 8 mm yr^{-1} in water equivalent [Wahr et al., 2006]. The root mean square error of the GRACE mass estimate is calculated using the provided errors in the Stokes coefficients in the GRGS solutions, following the proposed method by Wahr et al. [2006]:

$$\sigma = \sqrt{\sum_{n,m}\left(F_{nm}^{2}\left[\sum_{i=1}^{N}\frac{\delta C_{nm}^{2}}{N}\right]+G_{nm}^{2}\left[\sum_{i=1}^{N}\frac{\delta S_{nm}^{2}}{N}\right]\right)} \qquad (4.9)$$

where F_{nm} and G_{nm} are coefficients defining the averaging kernel, n and m are degree and order, respectively, and δC_{nm} and δS_{nm} represent the error in the Stokes coefficients C and S, respectively [Wahr et al., 2006].

For ICESat measurements, uncertainties are near zero in the interior of the ice sheet, where a dense network of laser ground-tracks exists. However, along the ice sheet margins the error is estimated to range between 0.15 and 0.3 m yr^{-1} [Hoffmann, 2014]. This is due to greater distances between the laser ground-tracks and, additionally, steeper slopes along the margins. Furthermore, laser penetration errors occur where the surface snow is soft (usually in warmer coastal regions), allowing the laser to penetrate deeper into the top layer (Chapter 2, Section 2.2). Here the uncertainty estimates are taken from the provided ICESat results as obtained by Hoffmann [2014].

GIA models in Antarctica generally contain large uncertainties due to the paucity of observations as a result of the permanent ice coverage that still exists. Furthermore, uncertainties remain in the knowledge of former ice sheet extent, deglaciation history and mantle viscosity [e.g. Argus et al., 2014]. In the Enderby Land region an uncertainty of ±1.2 mm yr^{-1} in the uplift rate is estimated near Mawson Station and around ±2 mm yr^{-1} for Syowa Station (Figure 4.1), with no observations available between these two stations to verify uplift rates [Argus et al., 2014].

The regional climate model RACMO2/ANT is specifically adapted to the climatic conditions in Antarctica and has been validated with field observations, where available. The overall uncertainty for SMB is estimated to be 10 %, however, no observations are available for most of Enderby Land [Lenaerts et al., 2012]. In order to obtain an uncertainty estimate of the RACMO data I calculate the 10 % error of the SMB and take this as the uncertainty for the SMB estimates.

The firn compaction model contains several error sources. Firstly, the input values are taken from the RACMO2/ANT climate model and are used to represent the initial density and thickness of the top layer. Secondly, the density of surface snow is estimated based on a parameterisation after Kaspers et al. [2004] and the densification rate with depth and time after the dry snow parameterisation of Arthern et al. [2010]. The uncertainty estimates of my firn compaction model have been obtained by assessing the propagation of the major error sources that affect firn compaction rates and are estimated to be ±6 cm yr^{-1}. However, only few observations are available to validate density estimates, and propositions on the physical processes that govern densification rely on empirical calibrations and laboratory experiments (Chapter 3, Section 3.1). In general, the complex physics of firn densification is still not fully understood, and the density of snow and firn is not well known, thus introducing large uncertainties into the computations [Sutterley et al., 2014].

The total uncertainty of each method is estimated by calculating the propagation of errors of the individual uncertainties of the employed input fields.

4.4 Results

4.4.1 GRACE observations in Enderby Land

The area around Enderby Land is of great interest largely because the GRACE observations recorded an increase in mass between 2003-2014 (Figure 4.4). Mass variations in the interior are in balance, while a positive mass anomaly between 20-60 mm w.e. yr^{-1} is detected along the Enderby Land coast, most pronounced between 30°E and 60°E. I have derived the mass anomaly using the GRACE solutions RL03 provided by the Groupe de Recherche de Géodésie Spatial (GRGS) (Chapter 2, Section 2.1).

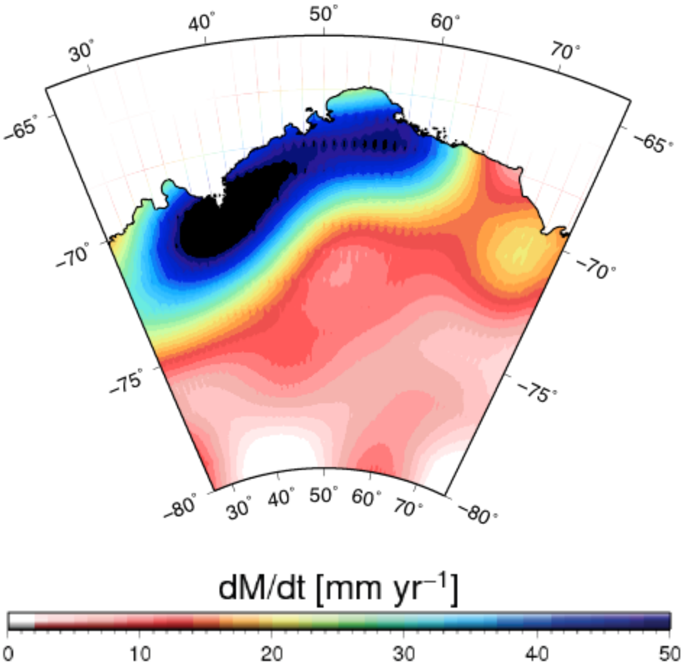

Figure 4.4: Mass anomaly detected by GRACE between 2003-2014 expressed in water equivalent to represent surface mass variations.

The time series for the location 66.6°S and 54.1°E in the Enderby Land region reveals discontinuities in the positive mass signal between 2006 and 2009 (Figure 4.5). Although it is not known whether the change is solely due to SMB or a combination of SMB and GIA uplift, it is suggested that the cause for the anomaly is due to increased snowfall in this region [e.g. Tregoning et al., 2009; Boening et al., 2012; Shepherd et al., 2012]. An increase in mass is visible until late 2005 (Figure 4.5), and again from late 2008 continuing, while the signal slightly decreases between 2006-2009. Altogether, this particular region in Enderby Land experienced a mass gain of approximately 650 mm of water (Figure 4.5, blue line) over a decade, assuming the change in mass is solely due to accumulation. Whereas, if the gravitational signal is caused by GIA (Figure 4.5, pink line), the total uplift of the bedrock over one decade would be almost 150 mm. The mass anomaly expressed in water equivalent is calculated using Equation 2.2, the anomaly representing GIA using Equation 2.4 in Section 2.1.3.

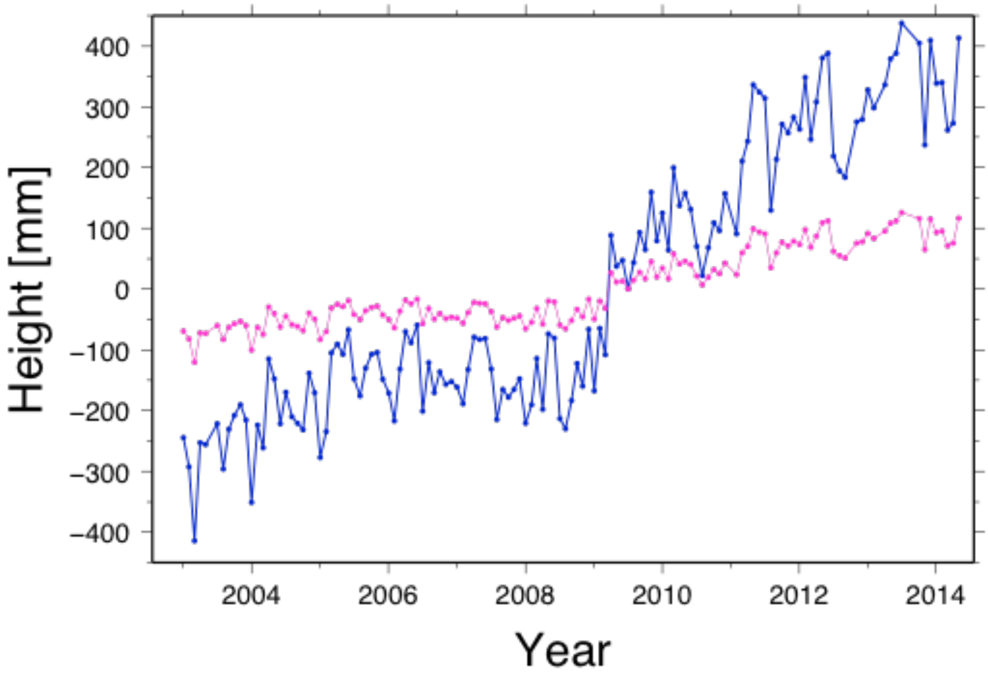

Figure 4.5: Time series for a location in Enderby Land for the GRACE observation period 2003-2014. In blue the GRACE signal is expressed in water equivalent, representing surface mass balance and in pink the signal is shown as the viscoelastic deformation of the lithosphere as a result of glacial isostatic adjustment.

4.4.2 Correcting GRACE observations for GIA

Despite large uncertainties in available GIA models for the Enderby Land region it is important to correct the GRACE observations for existing GIA uplift rates. To correct for the effect of isostatic compensation I remove the GIA component from the GRACE observations, using estimated GIA uplift rates as proposed by the ICE-6G model (Chapter 1, Section 1.4) [Peltier et al., 2015]. The following figure, Figure 4.6, shows predicted GIA uplift rates in Enderby Land as modelled by Peltier et al. [2015].

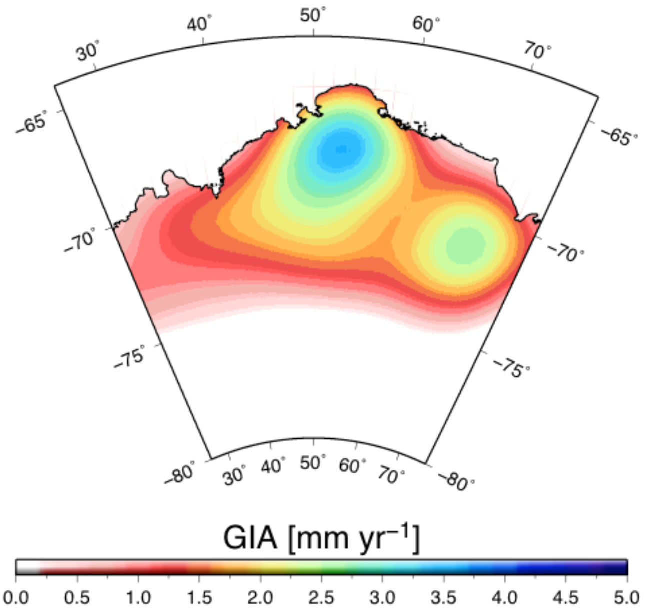

Figure 4.6: GIA uplift rates estimated by the ICE-6G model from Peltier et al. [2015].

According to the ICE-6G model, the largest uplift rates are found in the centre of Enderby Land, between 50 and 60°E, predicting a vertical uplift of ~3.5 mm yr^{-1}. The ICE-6G model is used to remove GIA uplift rates from the GRACE signal to derive GRACE anomalies solely due to SMB variations. After removing the GIA component the GRACE signal, obtained during 2003-2009, is considerably smaller (Figure 4.7b). It still contains the two strong positive mass anomaly locations but with a maximum trend of ~35 mm yr^{-1} near 42°E and 60°E, instead of ~40-45 mm yr^{-1} (Figure 4.7a). The obtained error of the GRACE mass values are approximately 8.25 mm yr^{-1}, which conforms with the estimated uncertainties of Wahr et al. [2006].

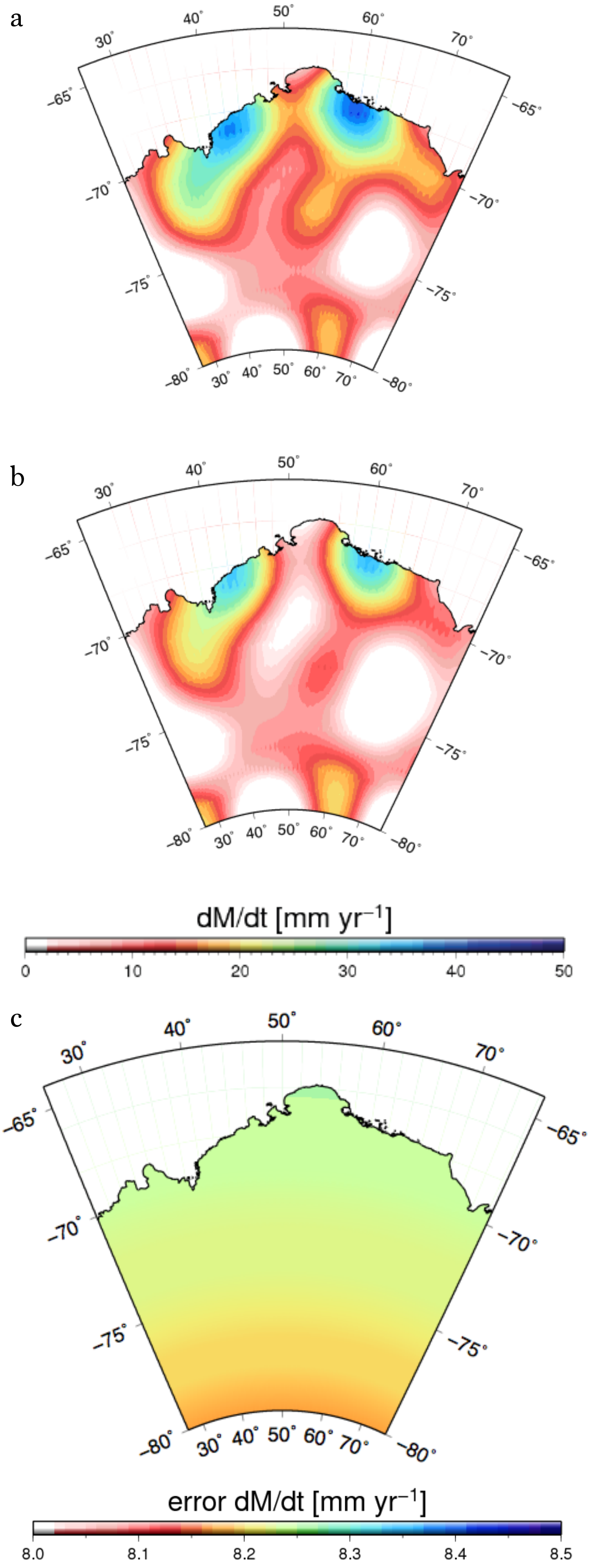

Figure 4.7a-c: GRACE anomaly between 2003-2009 a) before and b) after removing the bedrock uplift rates using the deglaciation model ICE-6G from Peltier et al. [2015]. c) is the uncertainty of the mass estimate.

4.4.3 Estimating V_{ice} from GRACE measurements

Figure 4.8a and 4.9a illustrate the modelled trend in monthly SMB from the RACMO climate model and the same transformed into spherical harmonics of degree and order 80. Representing the trend in SMB using spherical harmonics illustrates the smearing effects that occur when using spherical harmonics to represent the GRACE signal. As the simulated SMB trend is solely based on the processes occurring at the surface of the ice sheet, including snowfall, sublimation, evaporation, snowdrift and snowmelt, and Fig. 4.8a and Fig. 4.9a do not include ice dynamic processes, the trend in SMB is much higher than found in the GRACE observations and is not directly comparable at this stage. However, assuming that the GRACE signal only contains ice mass variations, after being corrected for GIA uplift rates, removing the modelled SMB amount from the GRACE data should yield an estimate of present-day ice dynamic rates.

The result is shown in Figure 4.10, where Fig. 4.10a represents the change in mass due to V_{ice}^{GRACE} for the uncorrected GRACE observations and Fig. 4.10b for the GIA corrected GRACE observations. In Figure 4.10c the obtained uncertainties for V_{ice}^{GRACE} are illustrated. The trend in V_{ice}^{GRACE} is larger after GIA is removed, resulting in a general greater signal across the ice sheet margins in Enderby Land. The largest ice dynamic rates are obtained across the ice sheet margin between 30°E and 50°E and near 70°E, with a rate of more than -130 mm yr^{-1}. The difference between the modelled ice dynamic rates before and after correcting the GRACE observations for GIA is approximately 10 mm yr^{-1}, most noticeable between 40°E and 60°E, with greater ice dynamic rates obtained further inland.

The spherical harmonic smearing effect of ice dynamic rates plotted in Figure 4.10 show a very similar picture to the smearing effects of the SMB uncertainties transformed into spherical harmonics (Fig. 4.9b), with the largest uncertainties located near 35°E and 56°E, and some smaller uncertainties between 44°E and 50°E, and near 70°E. Transformed into spherical harmonics these four regions result in a signal covering the ice sheet margin between 30°E and 48°E and around 70°E. This reveals a very similar picture to the result obtained in Figure 4.10b, suggesting that the regions with the greatest ice dynamic rates obtained by the GRACE observations are near 35°E, 56°E and 70°E, and between 44°E and 50°E.

The estimated uncertainties for the modelled ice dynamic rates are ±6 mm yr^{-1} across most of the ice sheet margin, and ±8 mm yr^{-1} between 35°E and 46°E.

Figure 4.11a-b compares the estimated trend in V_{ice}^{GRACE} after dividing by the density of ice in order to obtain the rate of height change, dH/dt, of V_{ice}^{GRACE}. Similar to the Figures 4.10a-b the trend in dH/dt of V_{ice}^{GRACE} is greater for the GIA corrected GRACE observations. Converted into a rate of change in elevation the modelled ice dynamic rates are around -20 cm yr^{-1} between 30°E and 50°E, and near 70°E, and -14 cm yr^{-1} across most of the coastal regions of Enderby Land. The estimated uncertainties of the converted ice dynamic rates are of similar magnitude with an estimated uncertainty of ±15 cm yr^{-1} between 30°E and 50°E, and near 70°E, and approximately ±11 cm yr^{-1} across the coastal regions.

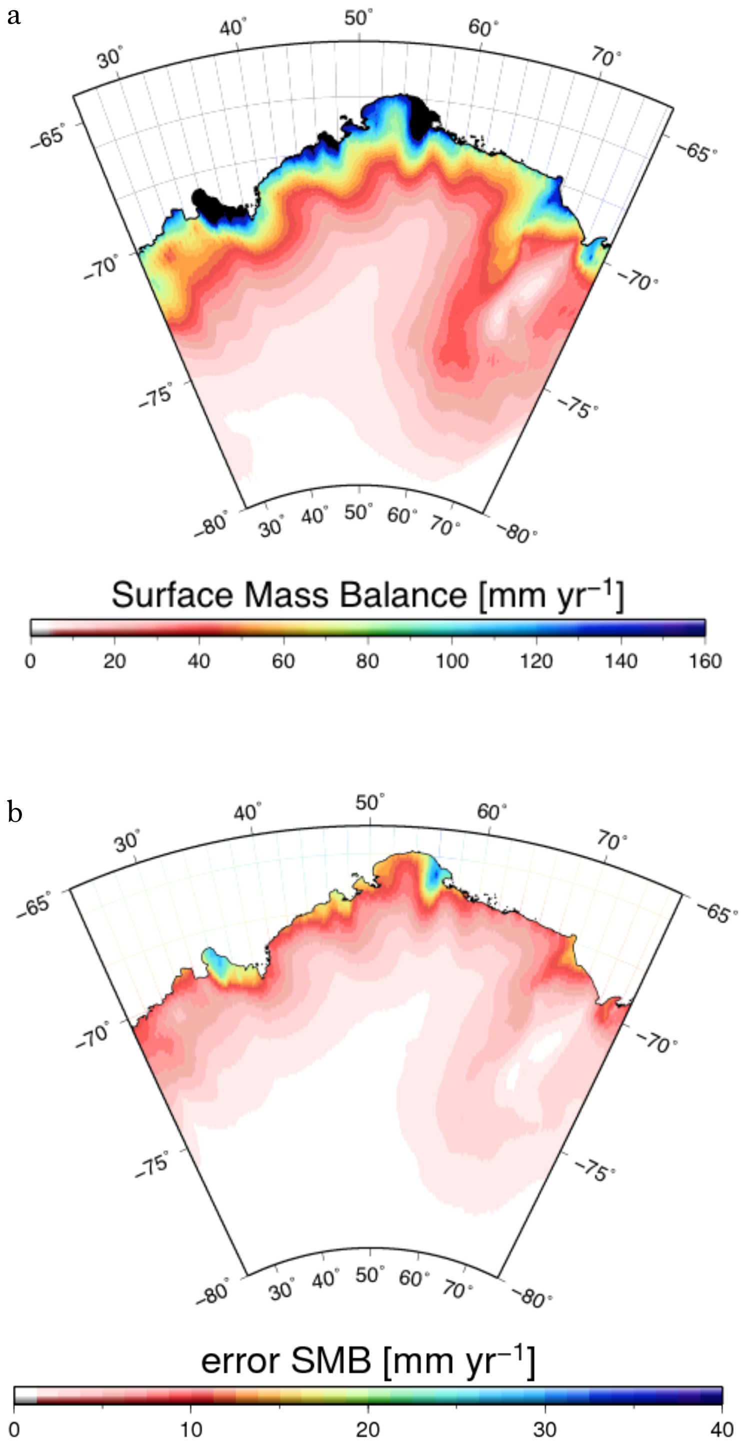

Figure 4.8a-b: This figure represents a) the modelled trend in monthly SMB as obtained from the RACMO2/ANT climate model and b) the uncertainty estimate.

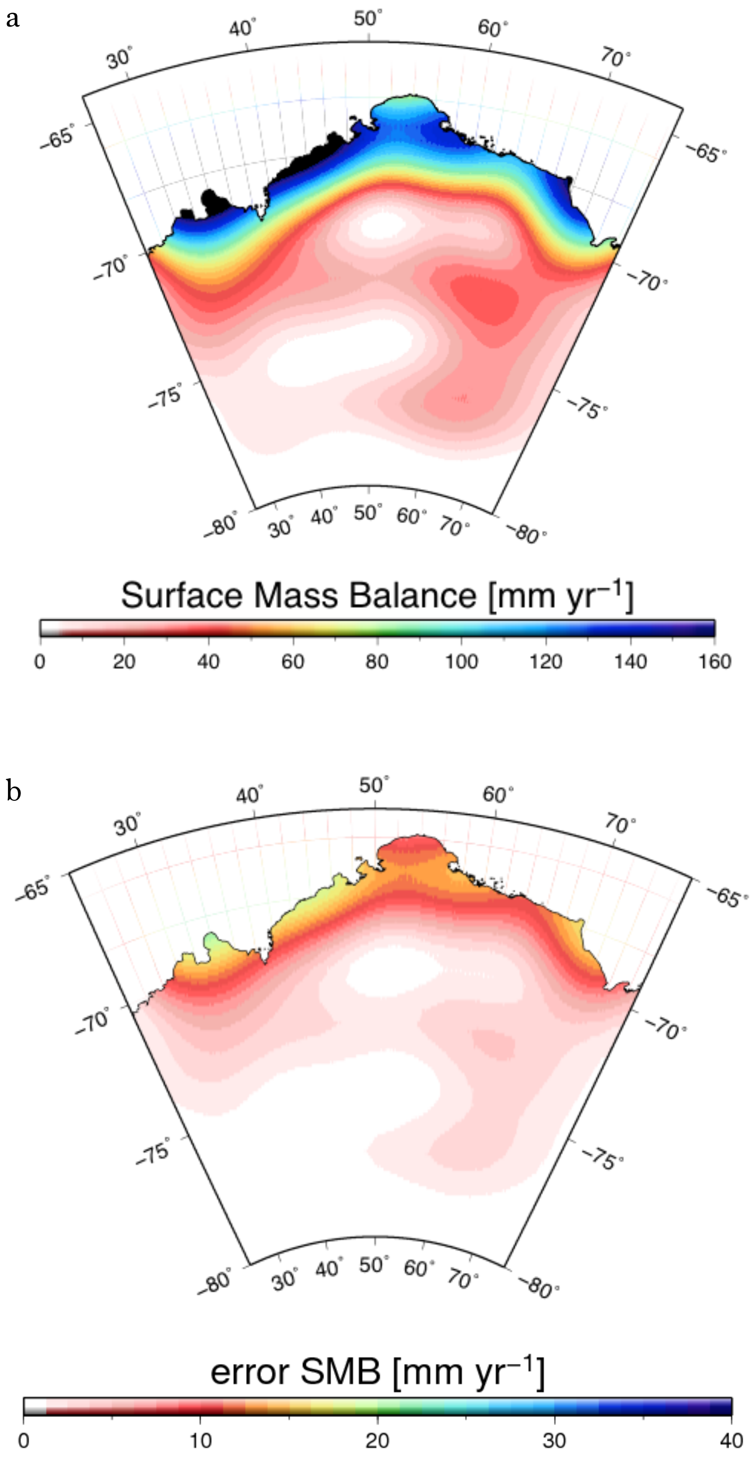

Figure 4.9a-b: This figure represents a) the modelled trend in monthly SMB transformed into spherical harmonics and b) the uncertainty estimates, likewise transformed into spherical harmonics.

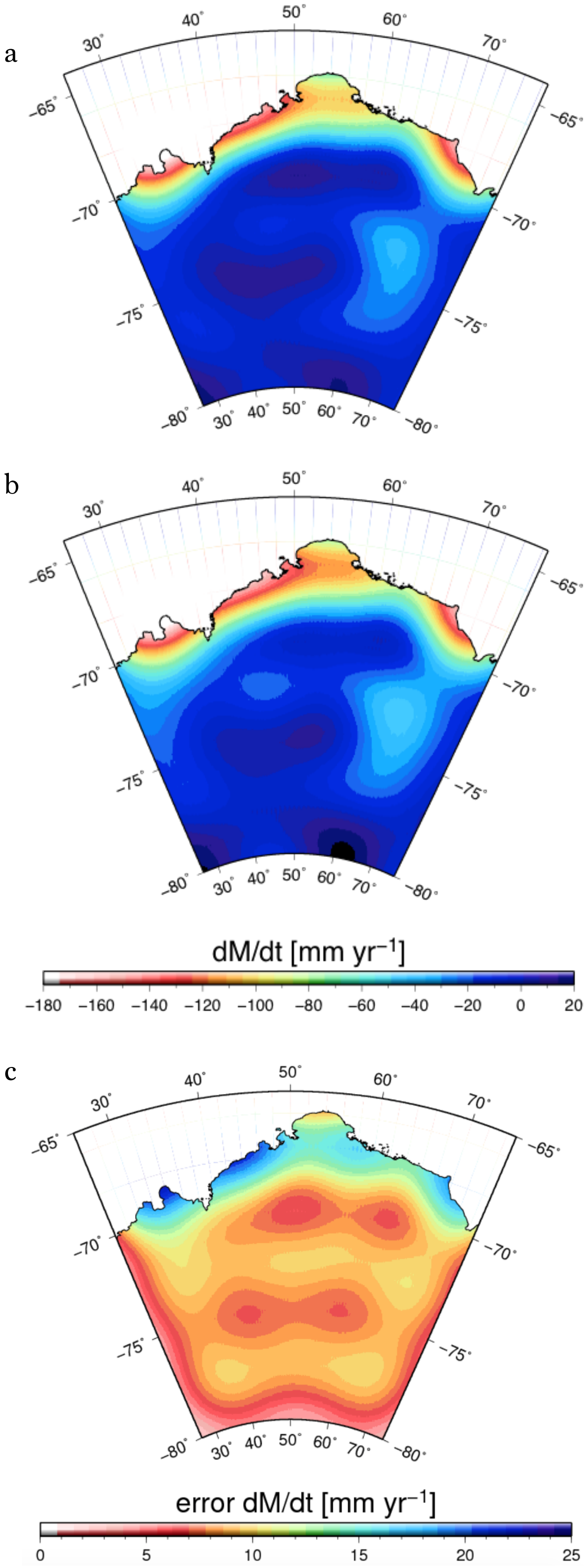

Figure 4.10a-c: dM/dt rates of V_{ice}^{GRACE} obtained from a) the actual GRACE signal and b) the GRACE signal after removing the contribution of GIA, and c) the dM/dt error estimates.

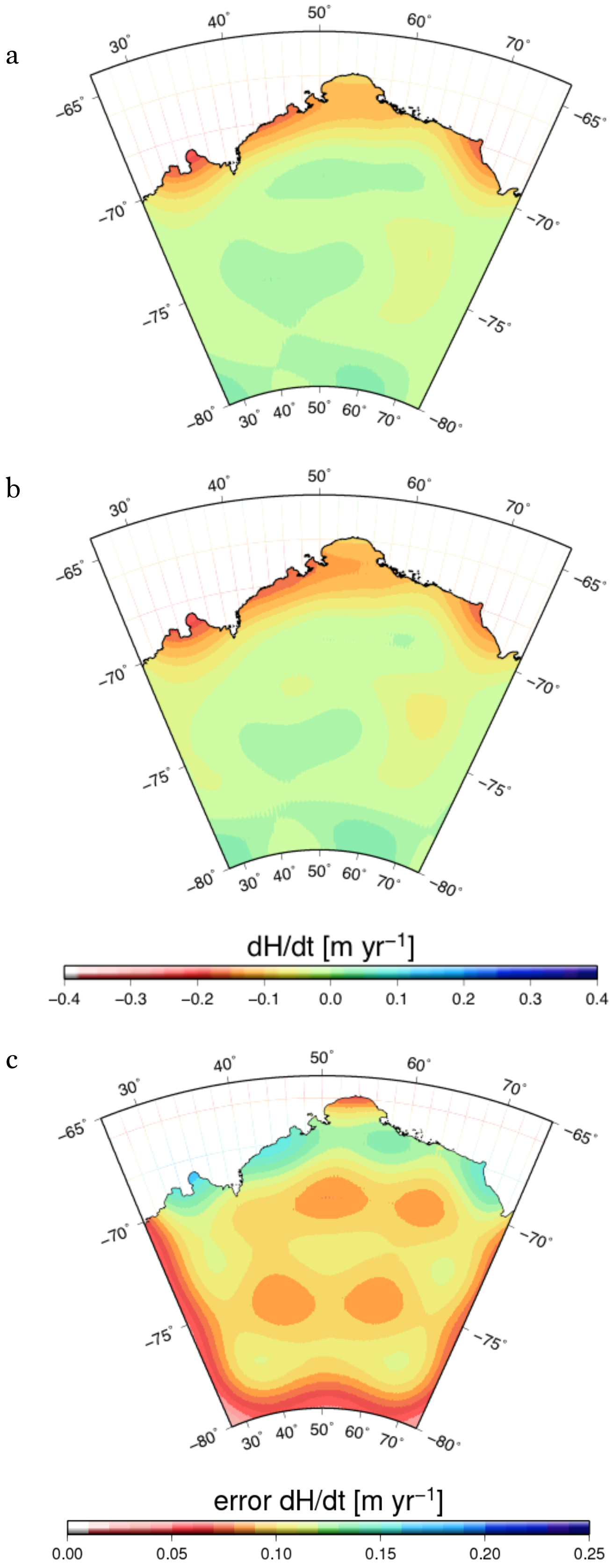

Figure 4.11a-c: dH/dt rates of V_{ice}^{GRACE} obtained from a) the actual GRACE signal and b) the GRACE signal after removing the contribution of GIA, and c) the dH/dt uncertainty estimates.

4.4.4 Surface elevation changes and estimating V_{ice}^{ICESat}

Figure 4.12 represents an example of ice sheet elevation changes due to surface mass, firn compaction and ice dynamics. The seasonal cycle of the individual processes together with the total change in surface elevation over the period 2003-2010 is shown for one location (66.6°S, 54.1°E) in Enderby Land. These monthly changes are modelled from SMB estimates of the RACMO climate model and my firn compaction model. A monthly average of ice dynamic rates is estimated by removing modelled changes in surface elevation due to SMB and firn compaction from altimetry observations (Section 4.2.1) (GIA is neglected).

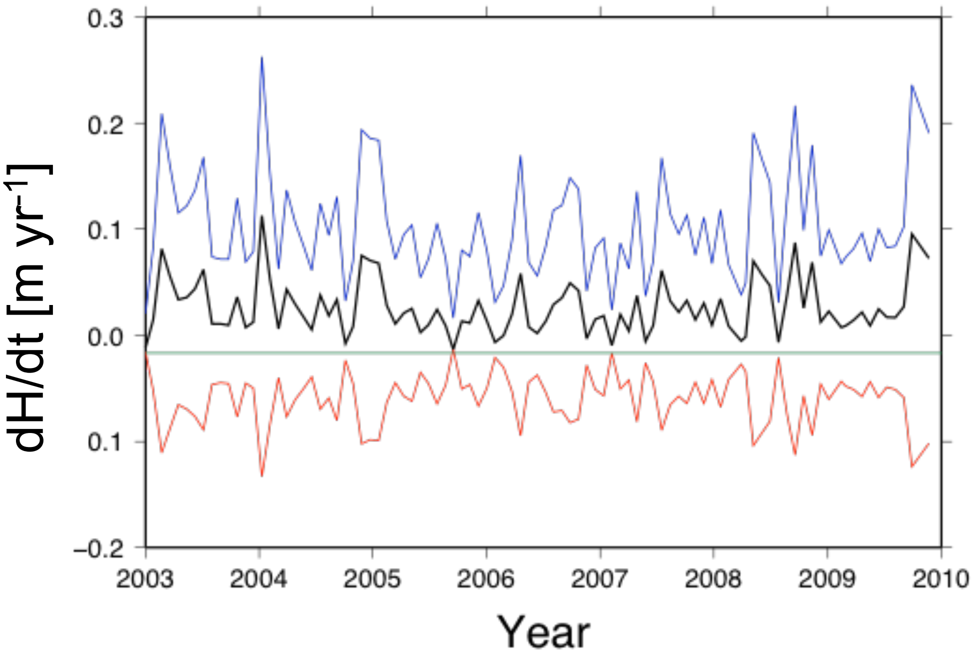

Figure 4.12: Processes that affect surface elevation over time for a location in Enderby Land. The total change in monthly elevation (black) is a combination of surface mass balance (blue), firn compaction (red) and a constant monthly mean ice dynamics rate (green).

Figure 4.13 shows the trends of the individual forcing fields that are used to estimate SMB in Antarctica, composed of accumulation, evaporation and sublimation, and snowmelt, covering the period of 2003-2009.

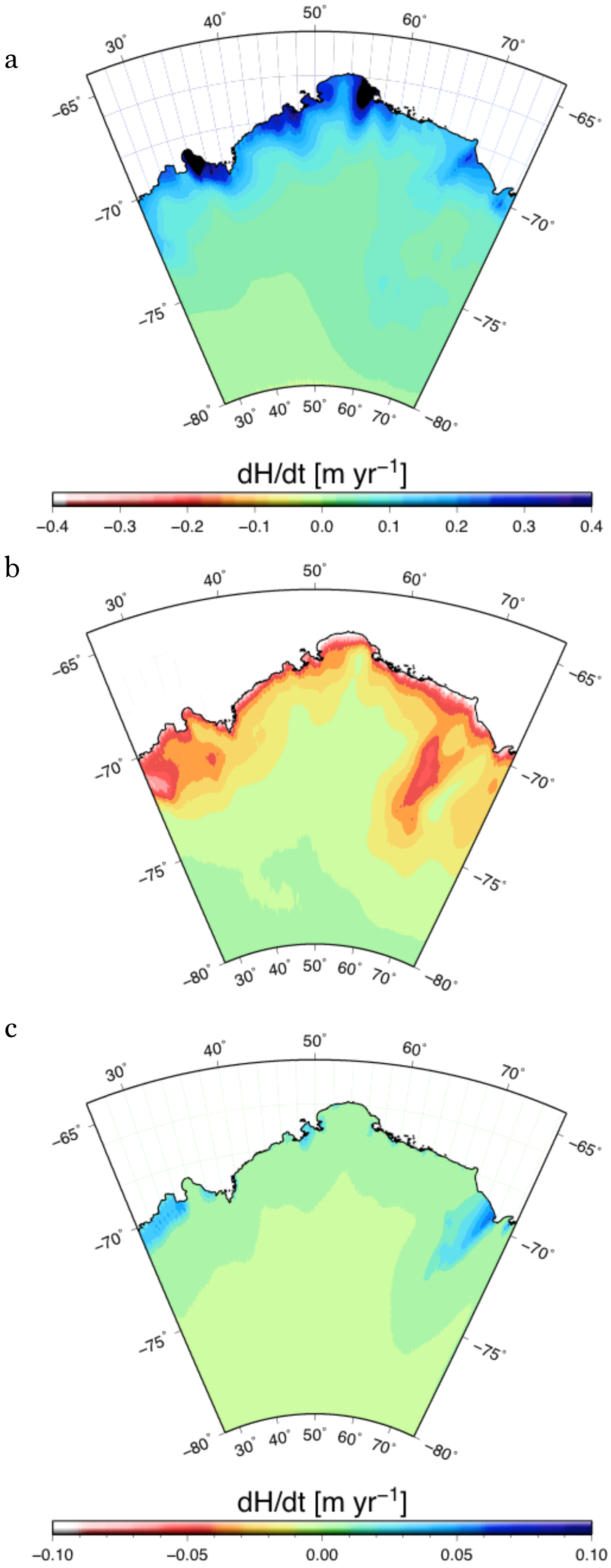

Figure 4.13a-c: Trend across Enderby Land in the RACMO forcing fields used to estimate SMB trends, for the period 2003-2009. a) snowfall, b) the combined processes of evaporation and sublimation and c) snowmelt rates. Note, b) and c) are the same scale, while a) has a different scale.

In the following figures I compare altimetry results obtained by Hoffmann [2014] to my modelled SMB results and extract the component of ice dynamic rates. Figure 4.14a shows the rate of change of elevation derived from the ICESat observations, showing variable behaviour across the Enderby Land region, with some reductions in height occurring along the coastal regions and other parts showing a gain in elevation. In terms of height gain three areas stand out, recording an elevation increase up to 140 cm yr^{-1} near 35°E, 55°E and 70°E, whereas elevation loss is observed along the ice sheet margin between 40°E and 52°E. The uncertainties of the ICESat observations are greatest at the margins, reaching up to 30 cm yr^{-1}, especially in the regions that show a decrease in elevation between 40°E and 52°E. The error estimates reduce gradually further inland. Here, the ICESat observations have not been corrected for firn compaction or GIA.

I compare the ICESat observations with the trend in elevation change solely due to SMB (Figure 4.15a) and after correcting for firn compaction (Figure 4.16a). Despite the difference in the resolution of the two datasets the comparison exemplifies that the regions with high rates of elevation gain in the altimetry observations can also be identified as high surface mass areas within the RACMO model. This is mainly due to high snowfall rates, supported by a positive deposition of snow due to drifting snow events (Chapter 1, Figure 1.c). The difference between the modelled elevation trend in SMB before and after correcting for the process of firn compaction is significant, especially along the ice sheet margin, and demonstrates the importance of the densification process within the firn layer.

If the topographic change observed by altimetry was due to variations within the firn layer and no changes existed within the ice column, the modelled change in elevation should match the ICESat observations. Consistent patterns of increase in height between the modelled and observed elevation change are distinguishable near 35°E and 56°E, both showing an increase in elevation of around 40 cm yr^{-1}. However, none of the negative elevation trends observed by ICESat are present in the modelled elevation trend solely due to firn compaction rates. Just as comparing modelled SMB trends with GRACE observations in the previous section, a direct comparison between the altimetry observations and the modelled elevation change is not possible at this stage, as ice dynamic rates have not been included yet. This leaves the assumption that ice dynamic processes are present in regions where ICESat detects a decrease in surface elevation and mass loss outweigh mass input.

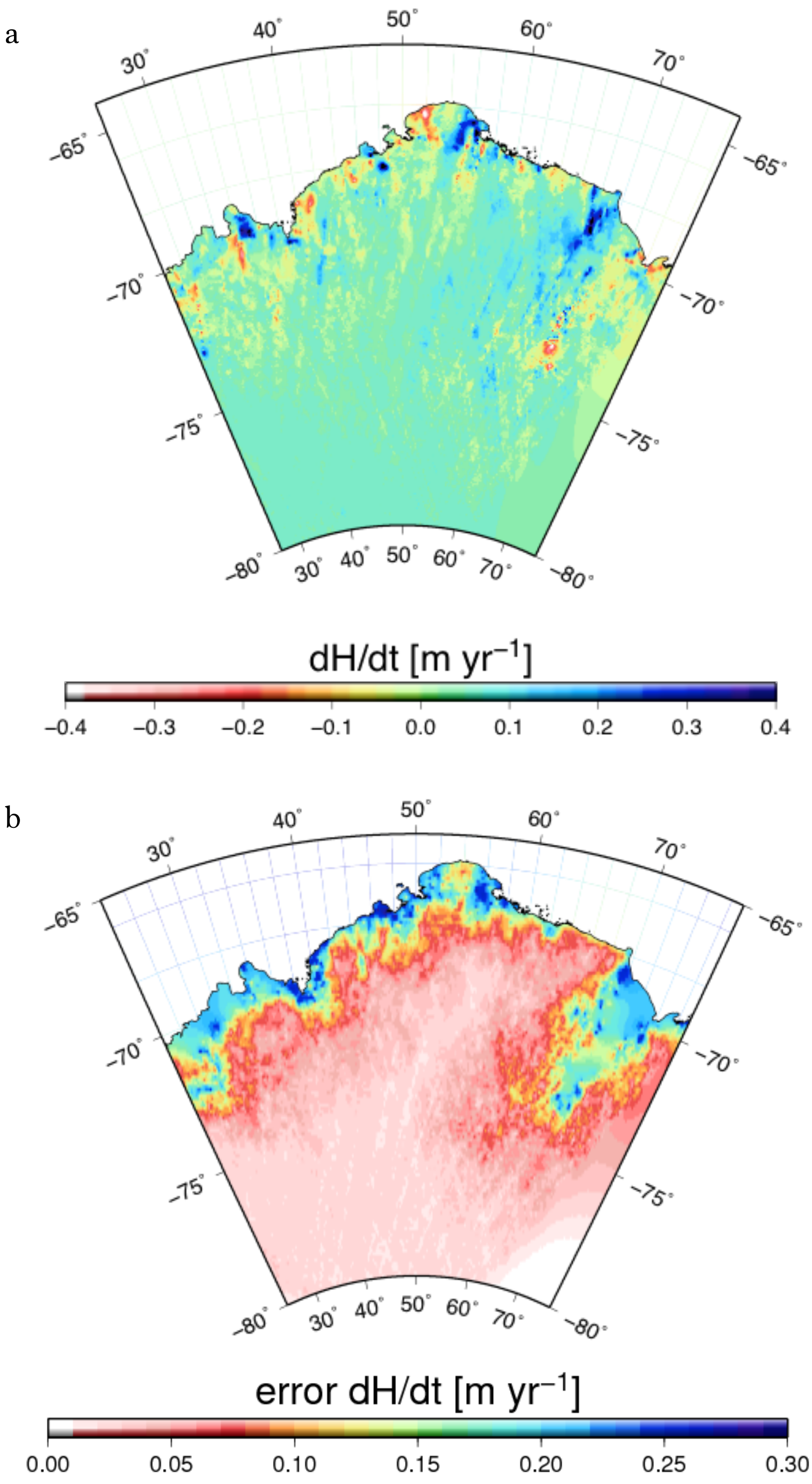

Figure 4.14a-b: a) ICESat altimetry observations over the period 2003-2009 across the study site and b) its error estimates. Data provided by Hofmann [2014].

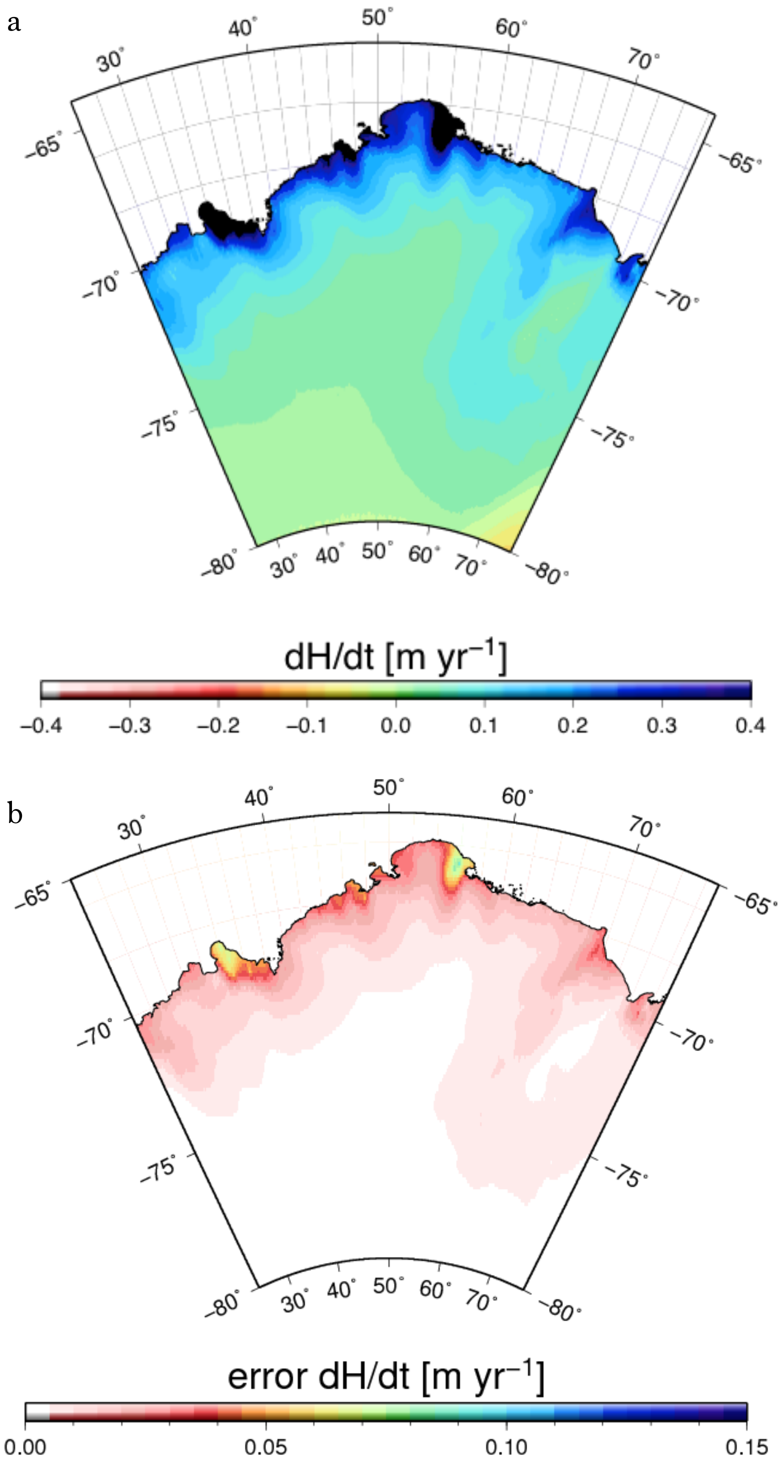

Figure 4.15a-b: a) Modelled trend in elevation change using SMB simulations of the RACMO2/ANT climate model uncorrected for firn compaction and b) a 10 % uncertainty estimate.

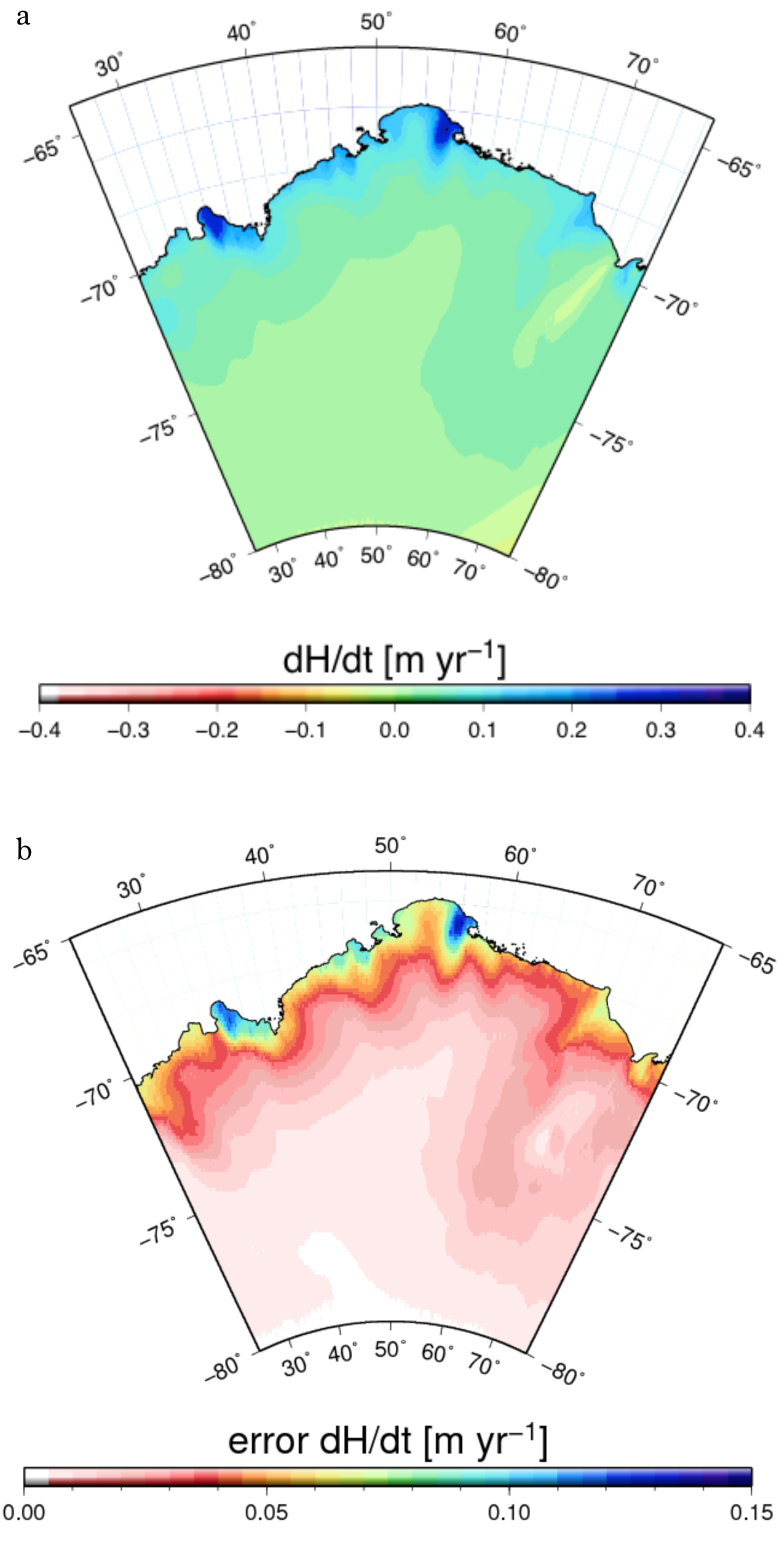

Figure 4.16a-b: a) Modelled trend in elevation change after removing the rate of firn compaction from the modelled SMB trend and b) its error estimate.

Under the assumption that the SMB and firn compaction models successfully represents the complex processes within the firn layer, I remove the modelled change in elevation caused by SMB and firn compaction from the ICESat observations, to obtain a rate for ice dynamic (V_{ice}^{ICESat}) (Fig. 4.17a). If the ice sheet is in balance in Enderby Land [Rignot et al., 2008], the rate of change of elevation due to ice dynamics should match the annual trend in SMB (Fig. 4.18).

The greatest values of the modelled ice dynamic rates are obtained along the coastal margins between 40°E and 55°E, as well as near 34°E, with the mean annual rate exceeding 20 cm yr^{-1}. While the high ice dynamic rates obtained near 34°E do not conform with any main outlet glaciers, it does fall into a region that has large uncertainties primarily due to the firn compaction modelling and the RACMO2/ANT simulations (Fig. 4.15b and 4.16b), with an estimated uncertainty of approximately ±22 cm yr^{-1} (Fig. 4.17b). The larger ice dynamic rates near 46°E coincide with the Rayner and Thyer Glacier, and also the ice dynamic rates to the west of the Rayner and Thyer Glacier fall into a region of higher ice dynamic rates (Fig. 4.1). While estimated uncertainties are greatest in the areas near 40°E and 46°E, both areas with the highest modelled ice dynamic rates, the region between 41°E and 44°E shows a rate of near zero. This region coincides with an area of one of the lowest uncertainty estimates. The high ice dynamic rates found around 50°E and 52°E occur in a region that shows no significant ice velocity rates (Fig. 4.1), however, ICESat uncertainties are ±20-25 cm yr^{-1} and nearly ±10 cm yr^{-1} for my modelled elevation change. The high ice dynamic rates found between 56°E and 64°E coincide with the Robert Glacier and faster ice dynamic rates along the coast (Fig. 4.1). Likewise, the high modelled rates near 75°E match a major outlet glacier east of the Amery Ice Shelf (Fig. 4.1).

Figure 4.18 shows the modelled mass anomaly for Enderby Land, showing an ice sheet that is largely in balance across the interior, with a slightly negative height change of approximately 6 cm yr^{-1} south of 75°S and a slightly positive height change of approximately 4 cm yr^{-1} north of 75°S. Along the margins a positive (+30 cm yr^{-1}) SMB rate is obtained, and there are some areas with high SMB rates of more than 40 cm yr^{-1}, located near 35°E, 45°E, 52°E and 56°E.

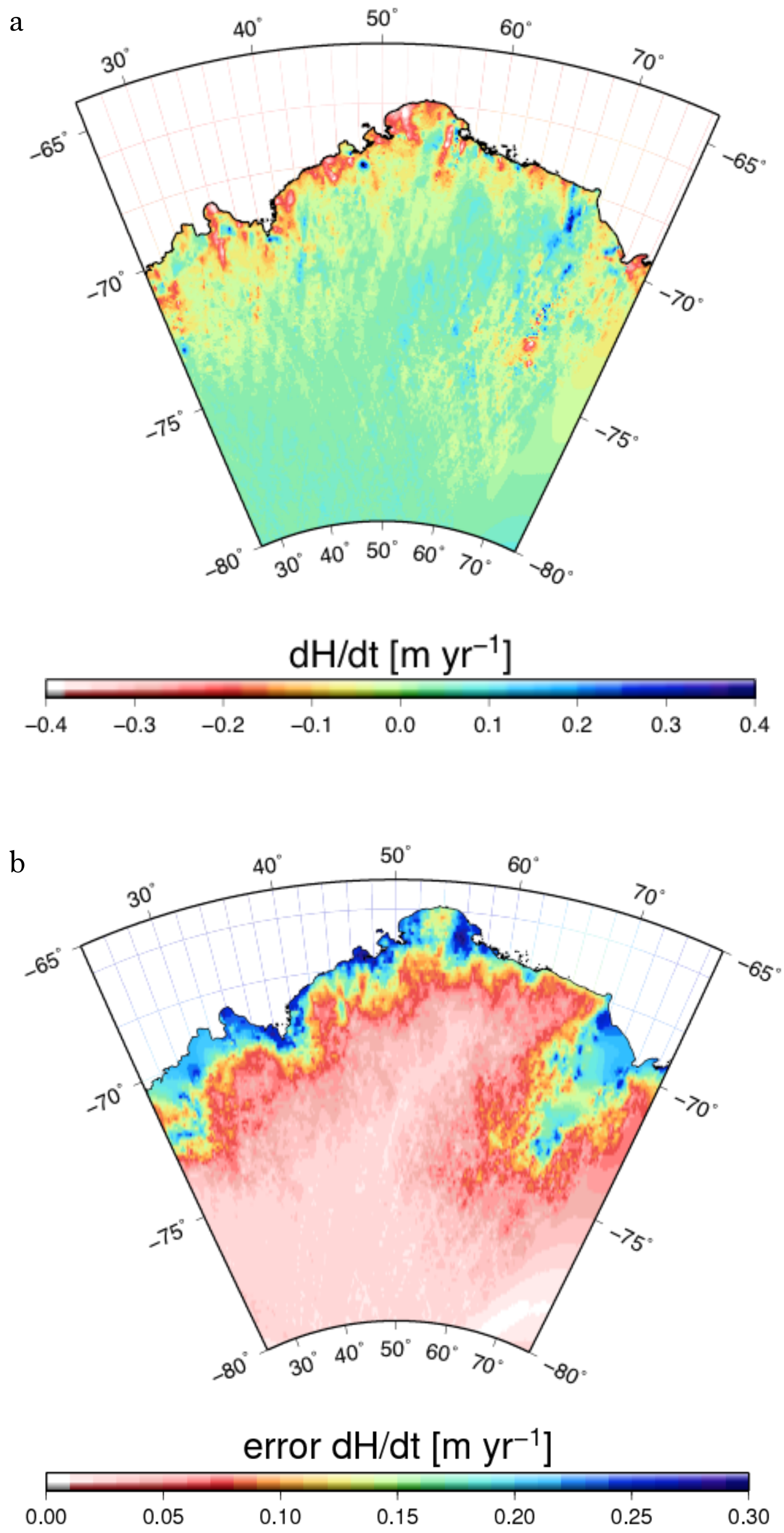

Figure 4.17a-b: a) dH/dt rates of V_{ice}^{ICESat} obtained by removing the signal of the firn layer from the ICESat observations, and b) the uncertainty estimate.

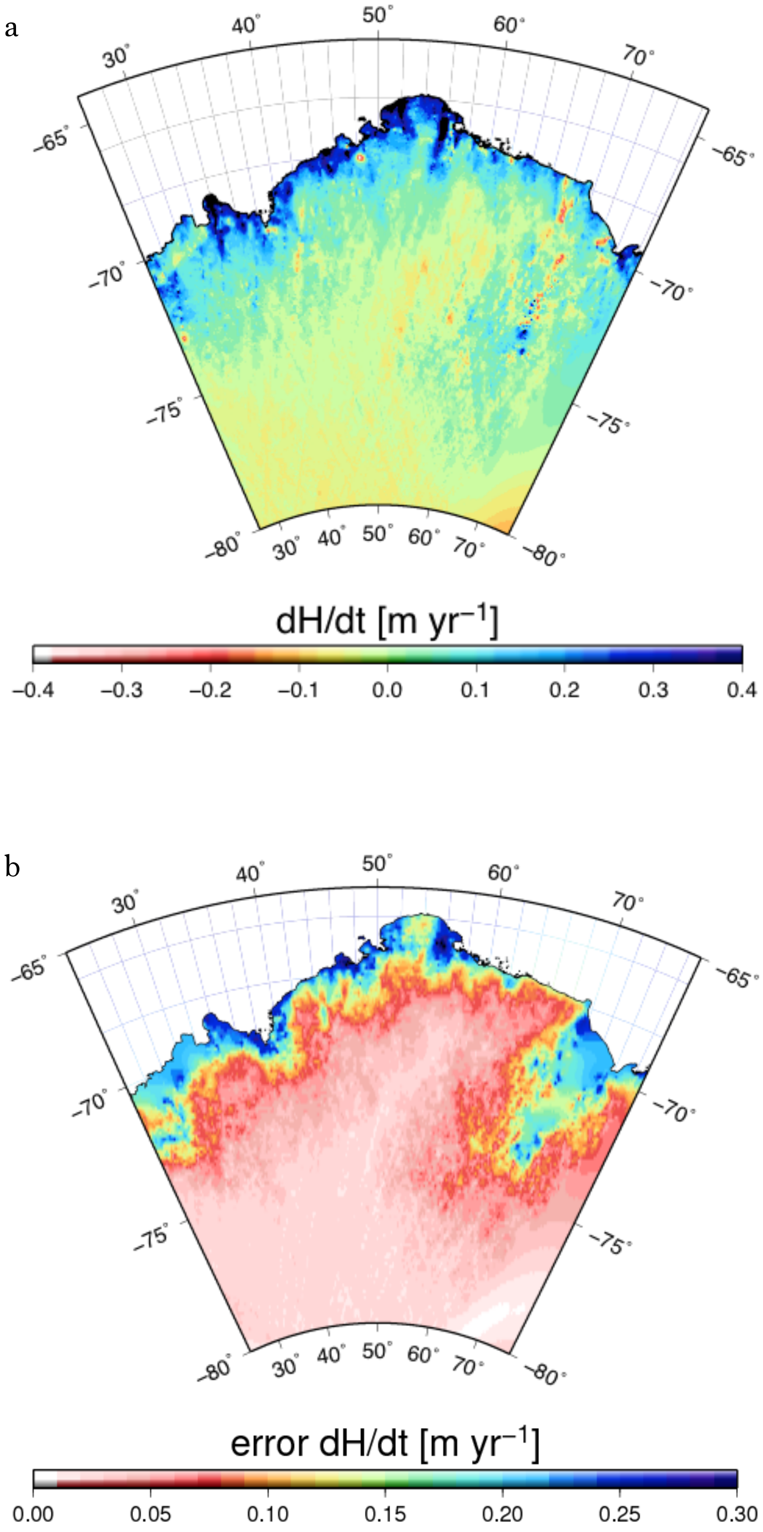

Figure 4.18a-b: a) Discrepancies between the annual surface mass balance trend and the obtained ice dynamic rates, representing surface mass balance anomalies and b) the estimated uncertainties.

4.4.5 Comparison of estimated ice dynamic rates obtained from ICESat and GRACE observations

Previously, I have obtained estimates on ice dynamic rates, assuming that my modelled elevation change due to SMB and firn compaction accurately represents the evolution of surface elevation. Once removed from the ICESat observations, I presume that the remaining signal represents the effect of ice dynamic. Similarly, I obtained ice dynamic rates from the GRACE observations by removing the SMB signal. Figures 4.19a and 4.20a compare the estimated ice dynamic rates expressed in water equivalent obtained from ICESat and GRACE corrected for GIA. The obtained V_{ice}^{ICESat} rates from the ICESat observations were converted into mass by multiplying with the density of glacier ice (917 kg m^{-3}).

Likewise, I converted my V_{ice}^{GRACE} estimates into a rate of change of elevation by dividing the estimates by the density of ice. The result is compared to the estimated V_{ice}^{ICESat} rates in the Figures 4.21a and 4.22a.

In Figure 4.19, dM/dt for V_{ice}^{ICESat} is shown in equivalent water height, after multiplying the obtained dH/dt V_{ice}^{ICESat} rates with the average density of the firn column. The estimated ice dynamic rates range between -20 cm yr^{-1} at the ice sheet margins between 30°E and 50°E, and +7 cm yr^{-1} near 65°E. The rate of dM/dt for V_{ice}^{GRACE} is illustrated in Figure 4.20 and shows a similar rate of the ice dynamic rates between 30°E and 50°E, with an estimated ice dynamic rate of -2 cm yr^{-1}. However, generally higher rates are found between 50°E and 60°E and around 70°E with estimated rates of around -11-13 cm yr^{-1} compared to -7-9 cm yr^{-1} for dM/dt V_{ice}^{ICESat}. On the other hand, for most of the interior ice dynamic rates are greater for V_{ice}^{ICESat} with positive rate estimates of more than +1 cm yr^{-1}, while V_{ice}^{GRACE} is slightly negative for most of the interior, with only a few locations showing a slightly positive rate estimate of +1 cm yr^{-1}.

This result is identical for the dH/dt estimates of V_{ice}^{ICESat} and V_{ice}^{GRACE}.

V_{ice}^{ICESat} rates are more than -10 cm yr $^{-1}$ for the ice margin between 30°E and 50°E but less than -10 cm yr^{-1} east of 55°E. However, V_{ice}^{GRACE} is similar between 30°E and 50°E but more than -10 cm yr^{-1} across most of the coastal region east of 55°E. Once again, ice dynamic rates are higher in the interior for V_{ice}^{ICESat} showing a positive rate of +5-10 cm yr^{-1}, whereas dH/dt of V_{ice}^{GRACE} is around 0 cm yr^{-1} or less. However, overall the signal of the modelled ice dynamic rates compare well between the altimetry and gravity observations, considering the different spatial resolutions between ICESat, GRACE and the RACMO model.

The uncertainties for V_{ice}^{ICESat} are largest between 30°E and 50°E, and above the Amery Ice Shelf between 70°E and 74°E, and generally above ±0.5 cm yr^{-1} for dM/dt (Fig. 4.19b) and ±15 cm yr^{-1} for dH/dt (Fig. 4.21b). For V_{ice}^{GRACE} the uncertainties are likewise greatest between 30°E and 50°E, and near 70°E, with more than ±1.3 cm yr^{-1} for dM/dt (Fig. 4.20b) and more than ±10 cm yr^{-1} for dH/dt (Fig. 4.22b).

Finally, with the ice dynamic rates obtained from both satellite missions and general agreement found between the ice dynamic trends, the final step is to combine my modelled SMB trends and my V_{ice}^{ICESat} estimates, to obtain mass balance anomalies, and vice versa, to obtain height anomalies, by combining modelled elevation trends and V_{ice}^{GRACE} .

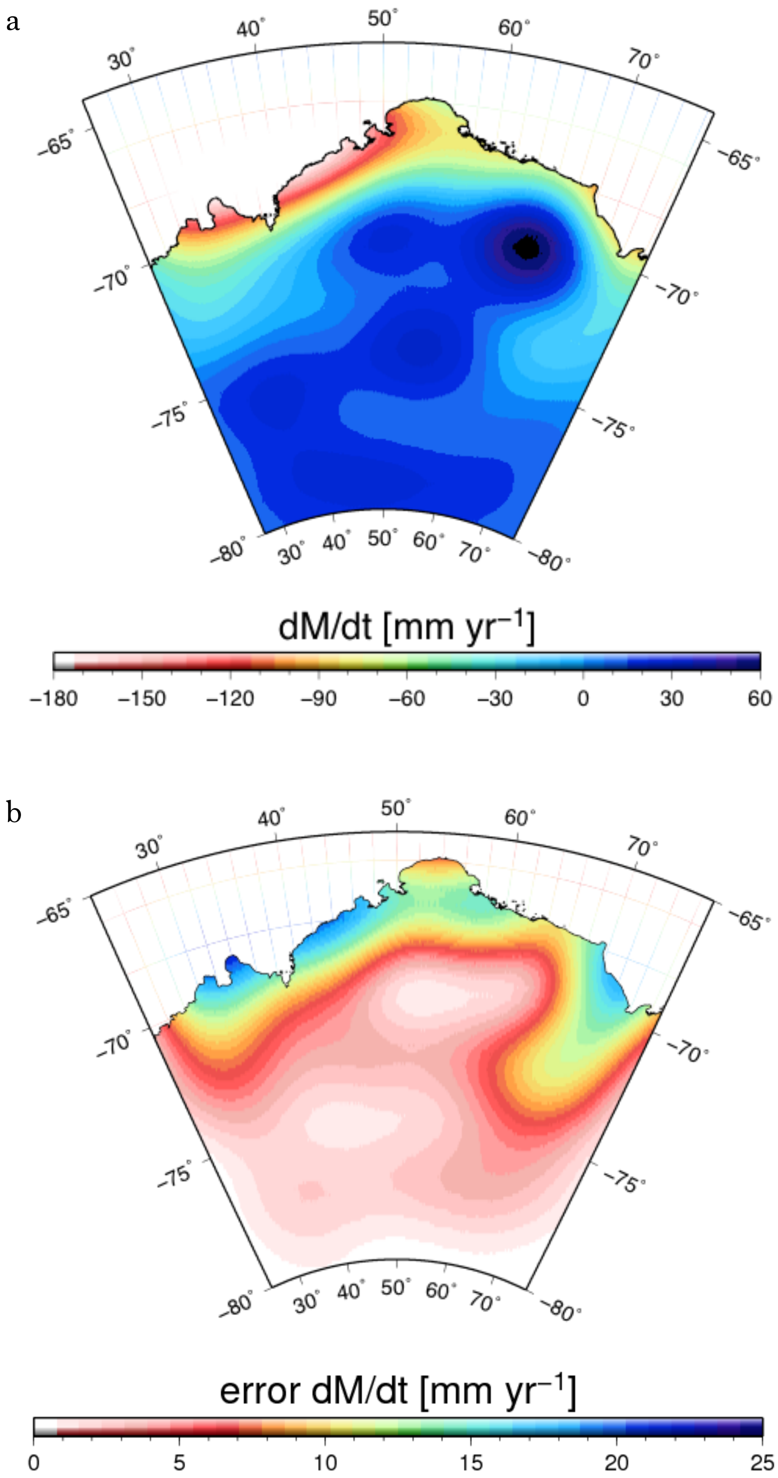

Figure 4.19a-b: a) Ice dynamic rates obtained from the ICESat observations and converted into a change in mass, which is expressed in mm water equivalent and b) the error estimates of the ice dynamic rate.

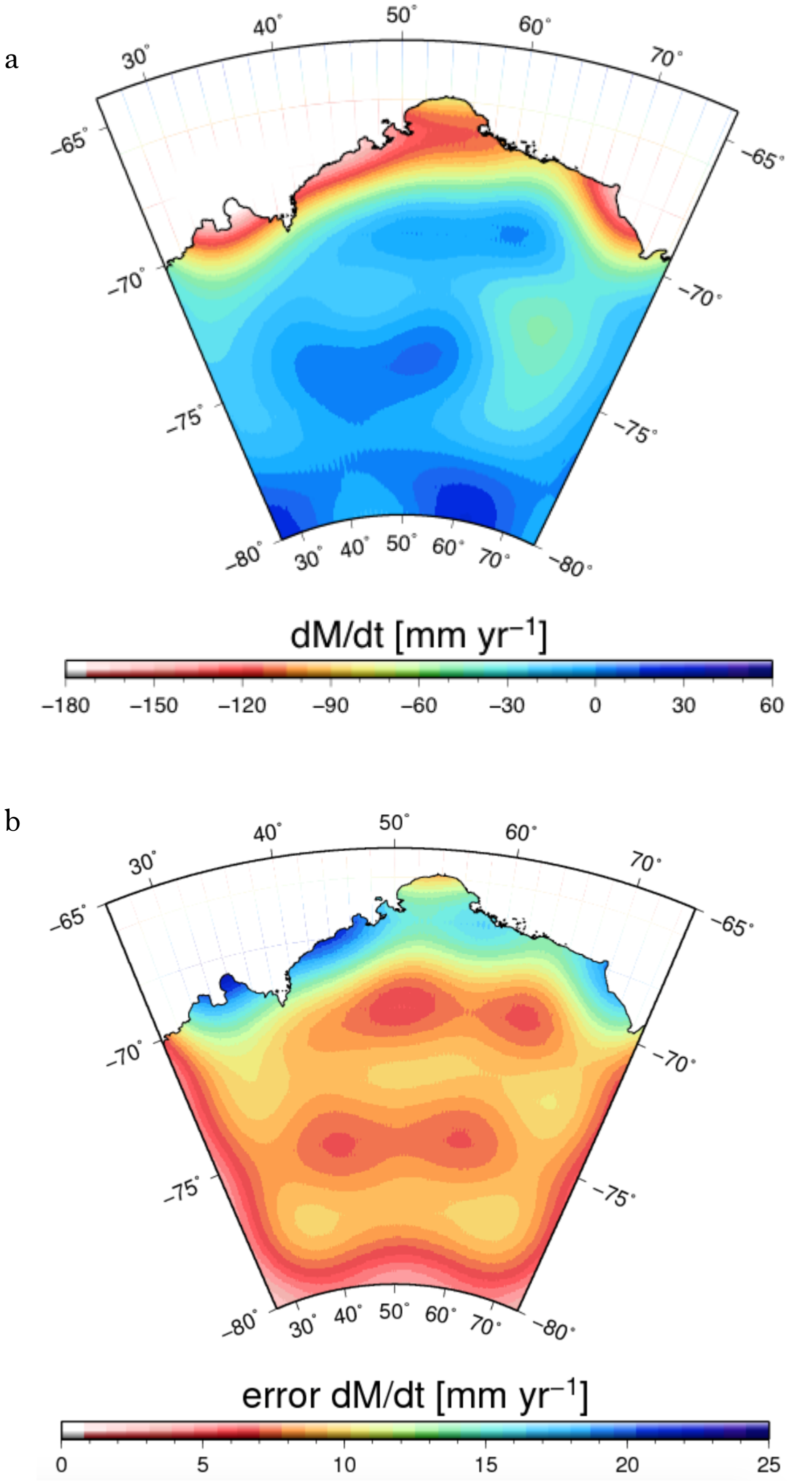

Figure 4.20a-b: a) Ice dynamic rates from the GRACE-GIA mass estimates, expressed in mm water equivalent and b) the error estimates of the ice dynamic rate.

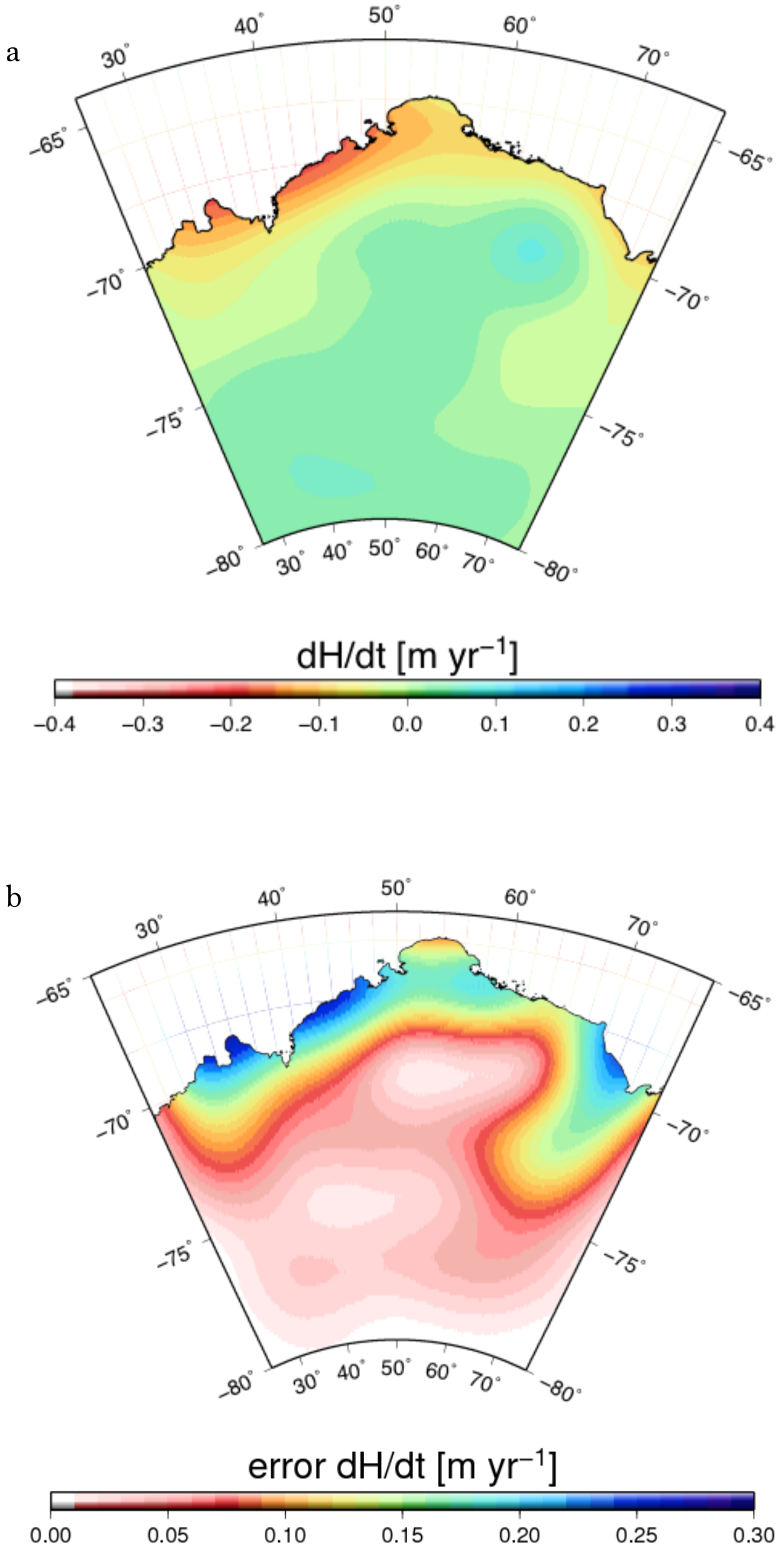

Figure 4.21a-b: a) Ice dynamic rates from the ICESat observations represented as a change in height and b) the error estimates of the ice dynamic rate.

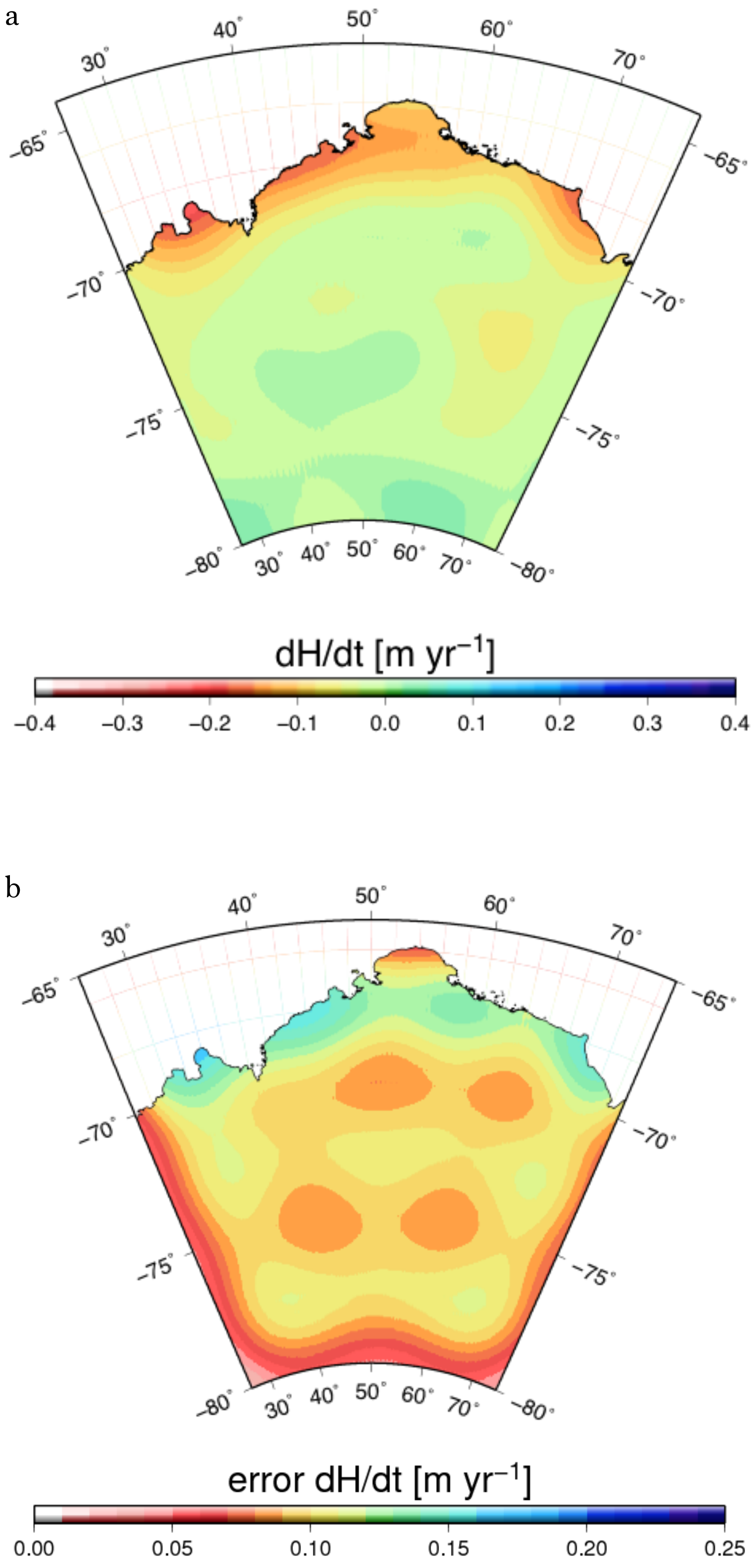

Figure 4.22a-b: a) Ice dynamic rates from GRACE-GIA observations, converted into a change in height and b) the error estimate of the ice dynamic rate.

Figure 4.23b represent the modelled elevation anomaly after removing dH/dt of V_{ice}^{GRACE} , before correcting the GRACE signal for GIA uplift rates, from my modelled elevation trend. Without correcting the GRACE signal for GIA uplift rates, the obtained anomaly shows a clearly positive anomaly across Enderby Land, with strong signals along the ice sheet margins, especially near 35°E and 55°E (Fig. 4.23b). Although this correlates well with the modelled height anomalies obtained in Section 4.4.4, removing V_{ice}^{ICESat} from the RACMO SMB simulations (Fig. 4.18a), thus suggesting that the obtained dH/dt trend in V_{ice}^{GRACE} agree with the V_{ice}^{ICESat} dH/dt rates, the signal is greater than the observed elevation trend from ICESat.

However, after correcting the GRACE signal for GIA, the comparison between the ICESat observations and my modelled elevation trend compares very well (Fig. 4.24b). Under consideration that the resolution of the ICESat observations differs from the resolution of my modelled rate of elevation change, areas observing a positive change in elevation match my modelled areas showing a positive increase in height, while regions of modelled height loss match the regions that recorded a drop in surface elevation.

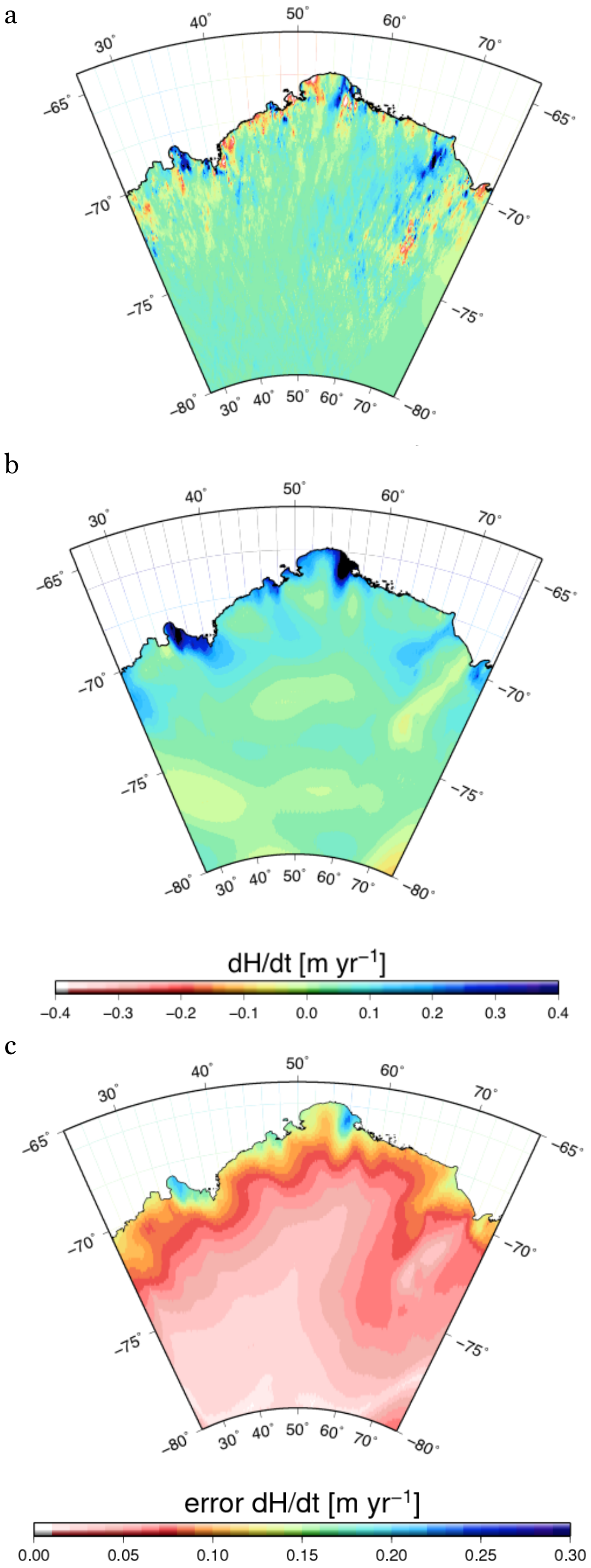

Figure 4.23a-c: a) ICESat observations compared with b) modelled elevation anomalies after removing for GIA uncorrected V_{ice}^{GRACE} dH/dt trends from the modelled SMB trend, and c) estimate of uncertainties.

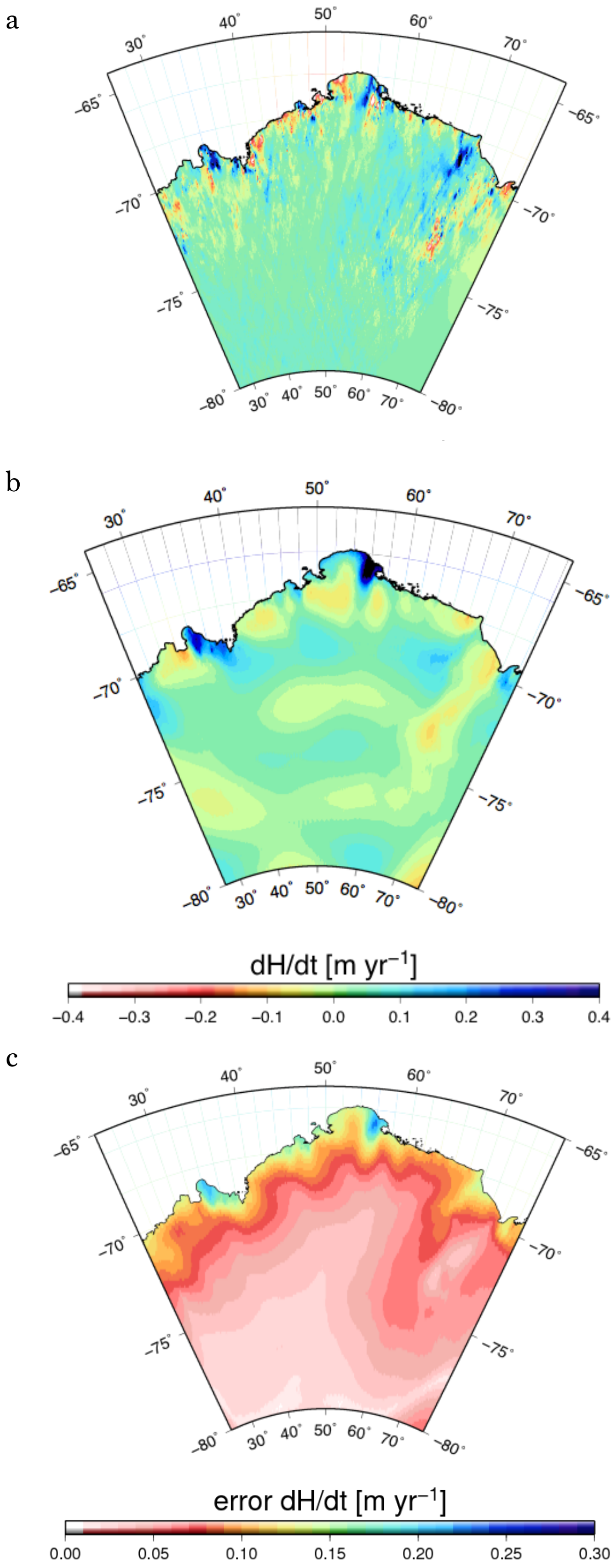

Figure 4.24a-c: a) ICESat observations compared with b) modelled elevation anomalies after removing for GIA corrected V_{ice}^{GRACE} dH/d trends from the modelled SMB trend, and c) estimate of uncertainties.

Similar to obtaining modelled elevation anomalies I also obtain modelled mass anomalies by removing the dM/dt signal of V_{ice}^{ICESat} from the mass trend of the RACMO SMB simulations (Fig. 4.25b). Considering the estimated ice dynamic rates obtained from ICESat and GRACE resulted in a similar estimate it is interesting to notice that the modelled mass anomalies are significantly larger than the GRACE observations.

The greatest difference can be found in a vast area between 55°E and 70°E that resulted in a positive ice dynamic rate of up to 10 cm yr^{-1}. This positive rate was obtained due to a strong positive signal obtained by ICESat in this region, while the modelled rate of elevation change is near-zero for the same region. This leads to a large area of positive ice dynamic rates as illustrated in Figure 4.17a in section 4.4.4. This positive signal is amplified when multiplying the dH/dt trend of V_{ice}^{ICESat} by the density of glacier ice, leading to a dM/dt estimate of V_{ice}^{ICESat} of more than 8 cm yr^{-1} in a large region. The uncertainties for this region are estimated to be between ±0.2-0.6 cm yr^{-1} for dM/dt. Along the ice margins between 30°E and 50°E the mass anomaly is found to be within the same magnitude as the GRACE signal. However, a positive anomaly is modelled between 30°E and 34°E, while GRACE detects a positive anomaly between 38°E and 45°E, a region where the modelled anomaly is much smaller with an estimated rate of ~1 cm yr^{-1} compared to ~4 cm yr^{-1} observed by GRACE. Furthermore, a slightly negative anomaly is modelled near 50°E, estimating dM/dt to be ~2 cm yr^{-1} smaller than recoded by GRACE. Altogether the differences between the observed and modelled mass anomalies are within the uncertainties between 30°E and 50°E. In turn, the large differences between 55°E and 70°E cannot be explained by the uncertainties as the signals differ by as much as ~6 cm yr^{-1}.

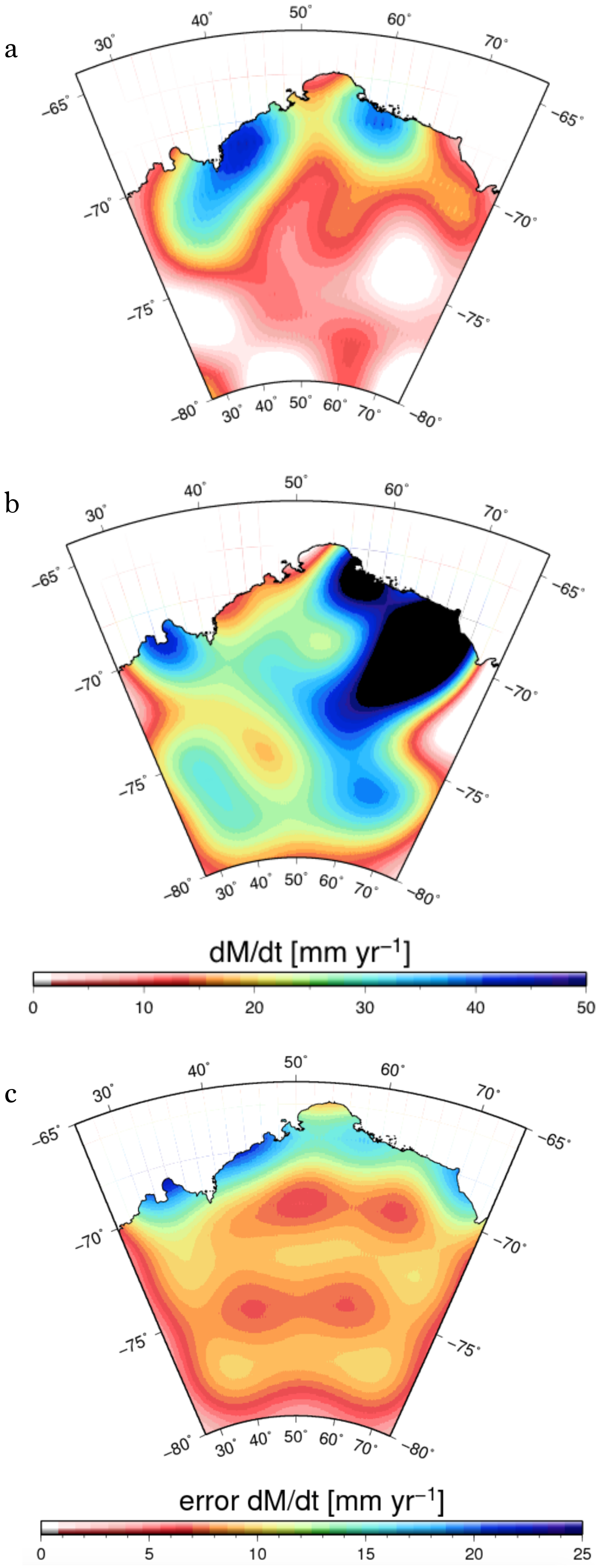

Figure 4.25a-c: a) Mass anomaly from the GRACE signal compared with b) modelled mass anomalies using my modelled SMB trend minus the mass trend in V_{ice} obtained from ICESat, and c) error estimates.

4.5 Discussion

I successfully compared my modelled mass anomalies and surface elevation trends across Enderby Land with gravity observations from GRACE and altimetry observation from ICESat, and I have combined the two datasets by estimating ice dynamic rates, combining observations and model results. First, I modelled the trend in SMB and obtained ice dynamic rates by removing my modelled SMB trend from the GRACE observations, assuming that the observed mass anomaly is solely due to ice mass variations. This provides me with an estimate of ice dynamic rates expressed in water equivalent. The same technique has been applied after the GRACE signal was corrected for GIA uplift rates as estimated by the ICE-6G model [Peltier et al., 2015]. Removing GIA from the GRACE observations results in a generally smaller mass anomaly across Enderby Land, and thus in greater ice dynamic rates. The largest ice dynamic rates are found along the margins of the ice sheet, especially between 30°E and 50°E, with a maximum rate estimate of -20 cm yr^{-1} between 32°E and 34°E, and only marginal smaller rates of more than -13 cm yr^{-1} between 40°E and 48°E. Another region of ice dynamic rates greater than -14 cm yr^{-1} is observed near 70°E. Between 50°E and 66°E the ice dynamic rates are between -8 and 11 cm yr^{-1}.

In the second part I obtained ice dynamic rates with regard to elevation height changes, by removing my modelled surface elevation changes from the ICESat observations. I obtained a rate of change in elevation by dividing the trend in SMB by modelled surface snow densities to convert to snow equivalent and subsequently subtracted the vertical displacement of the surface due to compaction, determined from my firn compaction model. I removed the contribution of GIA uplift rates and have determined the rate of ice dynamics by subtracting my modelled elevation change from the ICESat observations. Generally, ice dynamics are small in the interior, increasing towards the ice sheet margin, and are highest around glaciers (Fig. 4.1). The estimated rates are largely between -10 and -20 cm yr^{-1}, reaching up to -40 cm yr^{-1} in some regions along the margins of the ice sheet (Fig. 4.17). The highest rates are found at the coast between 40°E and 50°E, near 52°E, and across the Robert Glacier near 56°E. In comparison with ice velocity rates found in Enderby Land (Fig. 4.1) [Rignot et al., 2008; Allison et al., 2009; Rignot et al., 2011b; Mouginot et al., 2012] good correlations are found between the spatial distribution of larger discharge rates and some of the major outlet glaciers. With the ice sheet found to be largely in balance in Enderby Land [Rignot et al., 2008] the rate of ice discharge should approximate the rate of SMB, and the obtained rates indeed correlate quite well for regions without high annual SMB rates (Fig. 4.18). Three outstanding locations remain along the coast near 35°E, 55°E and 70°E, recording anomalously high SMB values. All three locations are clearly distinguishable in the RACMO model and the ICESat observations. Generally, throughout the RACMO climate model all three regions not only show high accumulation rates but also large mass depositions due to drifting snow events (Chapter 1, Figure 1c), suggesting that SMB exceeds ice dynamic rates at these locations, resulting in a positive increase in surface height, as observed by ICESat.

Besides the high precipitation locations, there are some regions that show a decrease in mass. The largest area is located where the Lambert Glacier flows into the Amery Ice Shelf (near 74°S 68°E). Smaller areas with mass loss are found between 30°E and 40°E, near the Shirase Glacier at 41°E and at 52°E. Interestingly, the Shirase Glacier (40°E) itself does not reveal large discharge rates, although the glacier was found to exceed accumulation until 2006. However, uncertainties are highest near the Shirase Glacier, not allowing for an adequate assessment of the estimated discharge rates. Another explanation could be that this is related to more frequent storm events and higher accumulation rates in the past decade. Similar results are found near the Rayner and Thyer Glaciers (49°E) with SMB exceeding ice discharge. This agrees with the finding of Rignot et al. [2008] who showed that mass input exceeds outflow at the glaciers. In contrast, the Robert Glacier (58°E) is visible as a region of large discharge rates in Fig. 4.17, but is located near the region of anomalous high SMB rates at 56°E (Fig. 4.18). Rignot et al. [2008] found the basin that includes the Robert Glacier to lose less mass than it accumulates until 2006, which is supported by the mass anomaly seen in my results (Fig. 4.18), and is likely due to the strong positive mass anomaly that is found nearby the glacier. The overall mass balance in the Lambert Glacier basin was found to be slightly positive until 2006 [Rignot et al., 2008]. In my results, a general positive mass balance is present around the Lambert Glacier, supporting the findings of Rignot et al. [2008].

The independently obtained ice dynamic rates can be compared with each other when multiplying or dividing by the average density of the firn and ice column at each location. This takes into account the fact that ice motion affects the entire ice sheet, including the firn layer that covers the Antarctic Ice Sheet, and was proposed by Zwally et al. [2005]. My average firn and ice densities are obtained during the spin up of my firn compaction model (Chapter 3) and represent both the firn layer and ice column. The ice dynamic rates from the altimetry, V_{ice}^{ICESat}, are converted to a change in mass expressed in water equivalent by multiplying by average densities. Then, the result is transformed into spherical harmonics to degree and order 80, to be comparable with the GRACE results. Likewise, the ice dynamic rates from GRACE, V_{ice}^{GRACE}, can be converted to a change in height by dividing V_{ice}^{GRACE} with the average density.

Both rate estimates, V_{ice}^{ICESat} and V_{ice}^{GRACE}, have their greatest ice dynamics rates between 30°E and 50°E with an estimated dM/dt of -12 to -19 ±1 cm yr^{-1} for V_{ice}^{ICESat} and -12 to -21 ±1 cm yr^{-1} for V_{ice}^{GRACE}, respectively. For the coastal region between 50°E and 58°E, V_{ice}^{ICESat} estimates are -7 to -10 ±0.35 cm yr^{-1}, while V_{ice}^{GRACE} is –8 to -12 ±0.4 cm yr^{-1}. Furthermore, V_{ice}^{GRACE} is significantly larger near 70°E, with an estimated rate of –12 to -16 ± 1.8 cm yr^{-1}, compared to -6 to -9 ±1.6 cm yr^{-1} for V_{ice}^{ICESat}. While ice dynamic estimates from V_{ice}^{GRACE} are predominantly negative (Fig. 4.20), ice dynamic rates from V_{ice}^{ICESat} are slightly positive across the interior, especially between 60°E and 70°E where a positive rate of up to 8 ±0.5 cm yr^{-1} was obtained (Fig. 4.19). The positive signal is obtained by the ICESat observations measuring a positive rate across this area (Fig. 4.14a) and is reflected in the modelled ice dynamic rates after removing the signal of the firn layer (Fig. 4.17a). This would mean that more ice from the interior flows into this region, than ice flows out.

Converted to dH/dt, the ice dynamic rates continue to correlate rather well. Estimated V_{ice}^{ICESat} rates are highest between 30°E and 48°E and decrease east of 50°E, with a maximum rate of -20 ±24 cm yr^{-1}. V_{ice}^{GRACE} estimates are slightly higher, showing a general stronger signal across the ice sheet margin, continuing east of 50°E, likewise with a maximum rate of -20 ±16 cm yr^{-1}.

In comparison with ice velocity rates (Fig. 4.1) from Rignot et al. [2011], my obtained ice dynamic rates show good agreement between higher ice dynamic rates near 35°E, covering the higher velocity rates along the ice margins near the Shirase Glacier and greater rates between 40°E and 50°E, covering the higher velocity rates of the Rayner and Thyer Glacier. The large velocity rate near 52°E does not correlate with the smaller ice velocity rates from Rignot et al. [2011], but occurs in a region of larger uncertainties, with an estimated error of ±25 cm yr^{-1}, impeding the comparison. The strong signal at 56°E covers the region of the Robert Glacier and a large rate near 70°E occurs at the Lambert Glacier, near the Amery Ice Shelf. Despite differences between the two modelled ice dynamic rates, general agreement is found between the distribution of the signal and the magnitude of the obtained rates.

Finally, the signal of dH/dt of V_{ice}^{GRACE} is removed from my modelled elevation change due to SMB and firn compaction and compared to the ICESat observations. Like the ICESat observations, strong positive anomalies are obtained near 35°E and 56°E, and negative signals are obtained near 30°E, between 40°E and 50°E and near 60°E. However, two locations remain that are not well correlated. The modelled elevation change suggests a slightly positive signal of 10 cm yr^{-1} near 50°E but shows an overall negative trend of -10 cm yr^{-1} near 70°E, quite in contrast to the ICESat observations that measure a negative trend of -45 cm yr^{-1} and -30 cm yr^{-1}, respectively. The uncertainty for the area of 50°E is estimated to be around ±15 cm yr^{-1}, while the estimate for the region near 70°E is around ±10 cm yr^{-1}. Overall, the modelled trend in elevation correlates well with the ICESat observations (Fig. 4.21).

On the contrary, modelling mass anomalies by removing the dM/dt component of V_{ice}^{ICESat} from the RACMO SMB trend, should result in a similar outcome to the GRACE observations. However, this is not the case. While the area between 30°E and 50°E is of similar magnitude between the modelled and observed mass anomaly, the distributions are different. A strong positive anomaly is modelled near 34°E, while smaller positive anomalies are obtained between 40°E and 50°E. On the contrary, the GRACE observations reveal a strong positive anomaly between 36°E and 46°E and a weaker positive anomaly near 34°E. Furthermore, a large positive anomaly of around 8 cm yr^{-1} is modelled between 60°E and 70°E, quite in contrast to the GRACE measurements that shows a positive anomaly near 60°E of a maximum rate of 4 cm yr^{-1}. While the differences between 30°E and 50°E are within the estimated uncertainties, the large difference between 60°E and 70°E cannot be explained by the uncertainties, with a difference of ~6 cm yr^{-1}.

Generally, it is difficult to compare GRACE observations with other datasets because of the difference in the spatial footprint. The circular shaped anomaly in the GRACE plot (Fig. 4.4 or Fig. 4.7) is unlikely to represent actual physical signals, as both ice sheet mass balance processes and GIA do not occur as circular signals. More likely these are artefacts that are introduced while processing the satellite data.

Nevertheless, it is interesting that the modelled elevation anomaly correlates well using ice dynamic rates obtained by GRACE, while the modelled mass anomaly is not comparable. This actually suggests that the GRACE observations agree well with the RACMO SMB trend resulting in a similar rate of change in elevation as observed by ICESat. However, the modelled elevation change between 55°E and 70°E is much smaller than suggested by ICESat, which leads to the possibility that ICESat rates are too high in this region or modelled SMB and firn compaction rates are too small. This would correlate with the fact that a smaller difference between the modelled and observed elevation change would result in smaller ice dynamic rates, obtained by removing the modelled SMB trend from the ICESat observation. This in turn would result in smaller dM/dt rates for V_{ice}^{ICESat} and thus in smaller modelled mass anomalies. More research is required to validate this concept, as well as observations on elevation changes, mass changes or ice dynamic rates.

4.6 Conclusions

In this chapter I showed that it is possible to obtain an estimate of ice dynamic rates by combining modelled elevation and mass changes with remote satellite observations. In the first step I modelled the trend in elevation due to surface mass balance and firn compaction, based on my firn compaction model presented in Chapter 3. The modelled change in elevation was removed from the ICESat observations to obtain an estimate of ice dynamic rates. The same was done in terms of mass variations, where I removed modelled surface mass balance variations from the GRACE observations, assuming that the observed signal is solely due to ice sheet mass balance. Consequently, I compared my individually obtained ice dynamic rates and found that general agreement exists between the two ice dynamic estimates. Commonly, ice velocity rates are largest towards ice sheet margins and around glaciers, even though the ice dynamic rates are represented in spherical harmonics to degree and order 80. This results in a smearing effect of the obtained signal across the margins. Nevertheless, consistency exists between the obtained ice dynamic rates, showing the same regions of greater rates along the ice sheet margins. While the ice dynamic rates based on GRACE present a general greater signal along most of the ice margin, the ice dynamic rates obtained with ICESat primarily show one dominant negative signal between longitude 30°E and 50°E. This region is susceptible to large uncertainties in the generated rate of change of elevation from the ICESat measurements and the modelled elevation, including uncertainties in the firn compaction rates. With an error estimate of 20-35 cm yr^{-1} in this location, my modelled ice dynamic rates are also prone to such large uncertainties. Should the actual change in surface height in this region be smaller than estimated from the ICESat observations, the difference between the modelled and observed rate of change of elevation would be smaller and thus result in smaller ice dynamic rates. Yet, my obtained ice dynamic rates correlate well with regions of larger ice velocity rates observed by Rignot et al. [2011b] and my modelled mass balance anomalies results in an overall estimate of ice sheet mass balance supporting the finding of Rignot et al [2008]. Moreover, it supports the occurrence of a positive mass balance anomaly in this region, likely as the result of more frequent storm events that have been specified by Boening et al. [2012], Shepherd et al. [2012] and Lenaerts et al. [2013], with the question arising whether more extreme storm events could potentially cover trends in overall mass loss [Rignot et al., 2011].

Finally, I compared my modelled height and mass anomalies with the ICESat and GRACE observations, by combining my obtained ice dynamic estimates. Theoretically, this modelled mass anomaly should correlate with the GRACE observations, if the observed signal is solely due to ice sheet mass balance. However, due to a large positive ice dynamic rate obtained from the altimetry observations between 60°E and 70°E, the modelled mass anomaly shows a very strong positive anomaly on a much larger scale than detected by GRACE. On the other hand, using ice dynamic rates obtained from GRACE to model height anomalies that are compared with ICESat observations, is successfully performed. The ice dynamic rates are converted to a change in height by dividing the rates with an average density of the firn and ice column. Removed from the modelled elevation change due to surface mass, the obtained height anomaly correlates well with the ICESat observations. However, in most regions across the study site the signal is larger than the ICESat observations. This suggested that the estimated ice dynamic rates were too small and that the GRACE observation detects another contributing process besides ice sheet mass balance. Therefore, in my final model I included the process of glacial isostatic adjustment (GIA) to correct for possible mass variations due to isostasy. I removed the GIA signal from the GRACE observations using the ICE-6G model [Peltier et al., 2015] and obtained my for GIA corrected ice dynamic rates. This led to a higher estimate in ice dynamic that was removed from my modelled elevation trend. Consequently, the obtained height anomalies are smaller than before correcting for GIA and correlate well with the ICESat observations. Both, regions of positive elevation changes and negative elevation changes are in agreement.

5 Conclusions

Despite increased availability in geodetic observations about mass variations and surface height, uncertainties remain in interpreting the obtained signals and assessing the origin of the observed change. To obtain a better understanding of the observed signals I have modelled surface height and mass changes over time using a regional climate model specifically adapted to Antarctic climate conditions. However, with few observations available to validate the model at some locations, large areas remaining unsampled. In order to obtain ice mass changes from altimetry observations it is important to include density variations with depth, as the process of firn compaction significantly affects the thickness of the firn layer, without there being any changes in mass.

The process of firn compaction is primarily influenced by surface load (accumulation) and temperature and is principally built on laboratory experiments and empirical models. The densification rate changes with depth due to increasing surface load and temperature changes. Therefore, the temperature evolution through the firn column is of great importance and can contribute to uncertainties in estimating densification rates. I forced the firn compaction model at the surface with near-surface climate observations from the regional climate model RACMO2/ANT. The temperature of the surface layer is assumed to equal the modelled near-surface temperature and the evolution of the temperature in the firn column is estimated using a one-dimensional heat transfer equation.

In Chapter 3, I showed the effects a bias applied to the input values of accumulation and temperature have on the modelled firn compaction rates, with the maximum bias chosen on the uncertainty estimates of the RACMO2.1/ANT model. Furthermore, I tested the sensitivity of the surface snow density parameterisation to varied input values and its effect on the firn compaction modelling. The surface snow density reacts most sensitively to temperature variations with a density variation of up to 20 kg m^{-3} for a temperature variability of 10 K (Fig. 3.1). Applying a 10 % bias to wind speed values result in a density variation of around 10 kg m^{-3}, while a 10 % bias applied to the accumulation shows no significant difference. Beginning the firn compaction model with higher or lower surface densities results in faster/slower densification as shown in Figure 3.2a-d. The sensitivity run for accumulation variations shows no significant changes in the densification rate (Fig. 3.3) but results in a much greater rate for the vertical velocity of the surface, primarily along the ice sheet margins (Fig. 3.6). For a 10 % bias, the vertical velocity varies by as much as 15 cm yr^{-1} at coastal Marie Byrd Land (220°E - 260°E), the Antarctic Peninsula and coastal Wilkes Land (100°E - 130°E).

The effect of a temperature bias is significantly smaller than the effect that accumulation has on modelled firn compaction rates. While the vertical velocity of the surface is reduced by 4 cm yr^{-1} along coastal Marie Byrd Land and Wilkes Land, only minor changes of around -1 cm yr^{-1} are observed across most of the interior for a temperature bias of 10 K (Fig. 3.9). However, interestingly large variability is found in the spatial distribution of the two critical densities, showing much faster densification rates when temperatures are warmer (Fig. 3.7 and 3.8). Such differences between the densification rate and the rate of the vertical velocity of the surface are possible, as a faster densification rate results in firn layers reaching high densities faster. Therefore more dense layers with low densification rates form, resulting in an overall lower velocity of the surface (Fig. 3.10). This is reversed for the accumulation, where no significant change is visible in the spatial distribution of the two critical densities but higher velocity rates are obtained. Faster velocity rates are obtained due to the increased surface-load, resulting in faster densification. However, due to the added surface-load of higher accumulation rates, thicker firn layers build up, burying previous layers faster, moving them to greater depths. Thus, the faster densification is most likely offset by the added material at the surface.

With simulations of SMB varying greatly between different climate models [Bromwich et al., 2011] and an uncertainty of 10 % within the RACMO climate model itself, accumulation represents a large error source when modelling the effect of firn compaction. While the effect of temperature variations is considerably smaller, the effect on firn compaction modelling can still be significant with differences between simulated RACMO temperatures and observed surface temperatures found to be ±5° K in some locations in Antarctica, and modelled temperature variations of up to ±12° K between different regional climate models [Maris et al., 2012].

The total uncertainty estimate of the modelled firn compaction rates is estimated to be ±6 cm yr^{-1} in the coastal regions of Marie Byrd Land and Wilkes Land, as well as the Antarctic Peninsula. For the vast interior, uncertainties are less than ±1 cm yr^{-1} (Fig. 3.12d).

Besides the uncertainties that are inserted by discrepancies within the input values, further uncertainties are introduced by a general lack of knowledge on snow and firn densities, with densities remaining largely unknown in Antarctica. Therefore uncertainties are introduced not only when modelling the firn layer density evolution, but also when converting the amount of accumulation into snow equivalent. Only a small number of observations are available to compare and verify density evolutions obtained with firn compaction models. Although Ligtenberg et al. [2011] validated their compaction model with 48 firn cores across Antarctica, large areas remain unsampled and modelled densities cannot be verified with in-situ observations. Furthermore, surface mass balance modelled by the RACMO climate model is provided in terms of mm w.e. yr^{-1} and thus needs to be converted into snow equivalent in order to represent a change in height as would be seen by an altimeter. With snow and firn densities largely unknown, and solely obtained from a firn compaction model, there are potential errors in converting surface mass balance into snow equivalent.

Besides uncertainties remaining in the process of firn compaction and thus ice sheet densities, another uncertainty lies within the conversion from ice height to mass due to ice dynamics. Although ice discharge can be estimated knowing ice velocities and ice thickness at the grounding line of the glacier, ice dynamics have an effect on the entire ice sheet due to ice motion.

Based on modelled changes in surface elevation from RACMO2/ANT surface mass estimates and my firn compaction model (Fig. 4.16), I obtained an estimate of ice dynamic rates in Enderby Land (Fig. 4.17). I first corrected the ICESat measurements for GIA uplift rates in Enderby Land as proposed by Peltier et al. [2015] (Fig. 4.6). Therefore, with changes in elevation assumed to be related solely to ice mass balance and firn compaction, the deviation between modelled and observed changes in surface height should represent ice dynamic rates (V_{ice}^{ICESat}). I therefore removed the modelled elevation change due to snowfall and firn compaction from the ICESat observations to derive V_{ice}^{ICESat} (Fig. 4.17).

Consequently, I followed the same method to obtain ice dynamic rates from the GRACE solutions. I modelled surface mass balance from the RACMO climate model, to obtain a trend in SMB between 2003-2009 (Fig. 4.8). First I removed GIA and my modelled rate of change of SMB from the GRACE observations, assuming that the remaining signal is due to ice dynamic (V_{ice}^{GRACE}) (Fig. 4.9b). To be able to compare the ice dynamic rates obtained from ICESat and GRACE, I must multiply my V_{ice}^{ICESat} by the density of glacier ice (Fig. 4.19). Generally, ice dynamic rates are highest near the ice sheet margin, with V_{ice}^{GRACE} (Fig. 4.20) resulting in a generally larger signal than V_{ice}^{ICESat}. For V_{ice}^{ICESat}, ice dynamic rates are smaller in most regions, apart from the coastal region between 30°E and 50°E, where a strong negative signal is obtained. In this region both, V_{ice}^{GRACE} and V_{ice}^{ICESat} are approximately -20 cm yr^{-1}. However, west of 50°E, V_{ice}^{GRACE} ice dynamic rates are -10 cm yr^{-1} or more, while V_{ice}^{ICESat} rates are less than -9 cm yr^{-1}. Yet, a strong positive V_{ice}^{ICESat} rate is obtained between 60°E and 70°E, contrary to V_{ice}^{GRACE} showing large negative values in this region. This large positive signal has a great effect on the modelled mass balance when combined with my modelled SMB. Thus, my modelled mass anomalies do not correlate well, with the positive anomalies from ICESat showing a much greater magnitude than the GRACE observations. Therefore, modelled mass balance anomalies using ice dynamic rates derived from ICESat do not agree with the observed GRACE signal at this stage in this location (Fig. 4.25).

Removing not for GIA corrected V_{ice}^{GRACE} rates as a change in height from my modelled elevation changes results in an elevation trend similar to the ICESat observations, though the signal is greater in my modelled height anomalies (Fig. 4.23). This supports the assumption that mass variations due to GIA are present in the observed GRACE signal and I therefore repeat the process using GRACE observations corrected for the effect of GIA (Fig. 4.24). I removed the contribution of GIA from the GRACE observations using estimations from the ICE-6G model [Peltier et al., 2015]. Correcting the GRACE signal for GIA variations results in slightly higher ice dynamic rates across the study site, and thus significantly smaller height anomalies. This results in a rate of change of elevation very similar to the ICESat observations in Enderby Land and, accordingly, shows that it is possible to extract ice dynamic rates from the GRACE signal by removing surface mass variations and GIA. Moreover, to some extent it validates the ICE-6G deglaciation model, estimating GIA uplift rates in Enderby Land, as smaller

GIA uplift rates (as suggested by Whitehouse et al [2012b]) would result in a pattern similar to using uncorrected GRACE observations.

Comparing observed and modelled anomalies from the RACMO2/ANT climate model provides information about the spatial distribution of surface mass balance variations. This is crucial when investigating local ice mass balance variations, as the smoothing of the signal due to the representation in spherical harmonics can cover regions of significant mass loss as seen in the comparison between the modelled surface mass balance trend, presented on the high resolution grid of the RACMO model, and transformed into spherical harmonics.

Finally, the V_{ice}^{ICESat} provides significant insights into ice dynamic rates in Enderby Land. Generally, the difference between surface mass and ice dynamic rates presents the mass balance of an ice sheet. Hence, removing the obtained ice dynamic rates from modelled surface mass balance rates yields mass anomalies in terms of surface height. According to Rignot et al [2008] the ice sheet in East Antarctica was found to be largely in balance until 2006. This is supported by my results, largely showing a positive signal across the study site and supports the occurrence of more frequent high precipitation events in East Antarctica. With my modelled ice dynamic rates showing agreement to the estimated ice dynamic rates of Rignot et al. [2008] I show that it is possible to obtain ice dynamic and ice discharge rates by removing the rate of change of elevation due to surface mass balance and firn compaction from altimetry observations. In order to validate this method, altimetry observations from other missions have to be included, to be able to compare the estimated ice dynamic rates and to obtain an average rate.

Because of the discrepancies, with the comparison between modelled and observed mass anomalies, more research is needed to understand these ambiguities. Uncertainties remain in both modelled and measured rates of change of elevation and mass, as well as GIA uplift rate estimates and firn compaction modelling. The largest uncertainty most likely is related to modelled density values of surface snow and firn in Antarctica, due to the paucity of observations and the complex processes that affect densification.

Nevertheless, my model results effectively suggest that the observed positive mass anomaly across Enderby Land is related to an increase in present day surface mass balance, and that the overall ice sheet remains in balance in this part of Antarctica.

References

Abshire, J. B., X. Sun, et al. (2005). "Geoscience Laser Altimeter System (GLAS) on the ICESat Mission: On-orbit measurement performance." Geophysical Research Letters 32(21): L21S02.

Allison, I., R. B. Alley, et al. (2009). "Ice sheet mass balance and sea level." Antarctic Science 21(05): 413-426.

Argus, D. F., G. Blewitt, et al. (2011). "Rise of the Ellsworth mountains and parts of the East Antarctic coast observed with GPS." Geophysical Research Letters 38(16): L16303.

Argus, D. F., W. R. Peltier, et al. (2014). "The Antarctica component of postglacial rebound model ICE-6G_C (VM5a) based on GPS positioning, exposure age dating of ice thicknesses, and relative sea level histories." Geophysical Journal International 198(1): 537-563.

Arthern, R. J., Vaughan, D.G., et al. (2010). "In situ measurements of Antarctic snow compaction compared with predictions of models." Journal of Geophysical Research 15: 306.

Arthern, R. J., D. P. Winebrenner, et al. (2006). "Antarctic snow accumulation mapped using polarization of 4.3-cm wavelength microwave emission." Journal of Geophysical Research: Atmospheres 111(D6): D06107.

Arthern, R. J., D. J. Wingham, et al. (2001). "Controls on ERS altimeter measurements over ice sheets: Footprint-scale topography, backscatter fluctuations, and the dependence of microwave penetration depth on satellite orientation." Journal of Geophysical Research: Atmospheres 106(D24): 33471-33484.

Arthern, R. J. and W., D.j. (1998). "The natural fluctuations of firn densification and their effect on the geodetic determination of ice sheet mass balance." Climate Change 40: 605-624.

Bahlburg, H. and Breitkreuz, C. (2004). "Grundlagen der Geologie." Spektrum Akademischer Verlag 2. Auflage.

Bamber, J. L., J. A. Griggs, et al. (2013). A new bed elevation dataset for Greenland.

Bamber, J. L., D. G. Vaughan, et al. (2000). "Widespread Complex Flow in the Interior of the Antarctic Ice Sheet." Science 287(5456): 1248-1250.

Benson, C. S. (1959). Physical Investigations on the Snow and Firn of Northwest Greenland 1952, 1953, and 1954, U.S Snow, Ice and Permafrost Research Establishment.

Biancale, R. (2012). GRACE/LAGEOS. GRGS Groupe de recherche de géodésie spatiale [Online]. Available: http://grgs.obs-mip.fr/grace [2015, January, 28]

Boening, C., M. Lebsock, et al. (2012). "Snowfall-driven mass change on the East Antarctic ice sheet." Geophysical Research Letters 39(21): L21501.

Bouman, J., M. Fuchs, et al. (2014). "Antarctic outlet glacier mass change resolved at basin scale from satellite gravity gradiometry." Geophysical Research Letters 41(16): 2014GL060637.

Brenner, A. C., J. P. DiMarzio, et al. (2007). "Precision and Accuracy of Satellite Radar and Laser Altimeter Data Over the Continental Ice Sheets." Geoscience and Remote Sensing, IEEE Transactions on 45(2): 321-331.

Bromwich, D. and W., Sheng-Hung (2008). "A review of the temporal and spatial variability of Arctic and Antarctic atmospheric circulation based upon ERA-40." Dynamics of Atmospheres and Oceans 44: 213-243.

Bromwich, D. H., J. P. Nicolas, et al. (2011). "An Assessment of Precipitation Changes over Antarctica and the Southern Ocean since 1989 in Contemporary Global Reanalyses*." Journal of Climate 24(16): 4189-4209.

Bruinsma, S., J.-M. Lemoine, et al. (2010). "CNES/GRGS 10-day gravity field models (release 2) and their evaluation." Advances in Space Research 45(4): 587-601.

Carrère, L. and F. Lyard (2003). "Modeling the barotropic response of the global ocean to atmospheric wind and pressure forcing - comparisons with observations." Geophysical Research Letters 30(6): 1275.

Chambers, D. P. and J. Schröter (2011). "Measuring ocean mass variability from satellite gravimetry." Journal of Geodynamics 52(5): 333-343.

Chen, J. L., C. R. Wilson, et al. (2009). "Accelerated Antarctic ice loss from satellite gravity measurements." Nature Geosci 2(12): 859-862.

Church, J. and N. White (2011). "Sea-Level Rise from the Late 19th to the Early 21st Century." Surveys in Geophysics 32(4-5): 585-602.

Church, J. A., N. J. White, et al. (2011). "Revisiting the Earth's sea-level and energy budgets from 1961 to 2008." Geophysical Research Letters 38(18): L18601.

Clark, P. U., A. S. Dyke, et al. (2009). "The Last Glacial Maximum." Science 325(5941): 710-714.

Cuffey, K.M. and Paterson, W.S.B.. (2010). "The Physics of Glaciers." 4th Edn., Pergamon, Oxford, U.K.

Dalziel, I. W. D. and Lawver, L.A. (2001). "The lithospheric setting of the West Antarctic ice sheet." The West Antarctic Ice Sheet: Behaviour and Environment, American Geophysical Union: 29-44.

Davis, J. L., P. Elósegui, et al. (2004). "Climate-driven deformation of the solid Earth from GRACE and GPS." Geophysical Research Letters 31(24): L24605.

Desai, S. D. (2002). "Observing the pole tide with satellite altimetry." Journal of Geophysical Research: Oceans 107(C11): 3186.

DiMarzio, J., et al. (2007). "GLAS/ICESat 500 m laser altimetry digital elevation model of Antarctica." Boulder, Colorado USA: National Snow and Ice Data Center. Digital media.

Ewert, H., A. Groh, et al. (2012). "Volume and mass changes of the Greenland ice sheet inferred from ICESat and GRACE." Journal of Geodynamics 59-60(0): 111-123.

Flament, T. and F. d. r. Rémy (2012). "Dynamic thinning of Antarctic glaciers from along-track repeat radar altimetry." Journal of Glaciology 58(211): 830-840.

Fogt, R., D. Bromwich, et al. (2010). "Understanding the SAM influence on the South Pacific ENSO teleconnection." Climate Dynamics 36(7): 1555-1576.

Fountain, A., Nylen, TH, MacClune, KJ, Dana, GL (2006). "Glacier mass balances (1993-2001) Taylor Valley, McMurdo Dry Valleys, Antarctica." Journal of Glaciology 52.

Francis, R., Wingham, D. and Cullen, R (2010). "CryoSat-2: Measuring fluctuations of land and marine ice fields from space." Geophysical Research Abstracts Vol. 12, EGU2010-6362-1.

Fretwell, P., H. D. Pritchard, et al. (2013). "Bedmap2: improved ice bed, surface and thickness datasets for Antarctica, The Cryosphere." The Cryosphere 7: 375-393.

Fricker, H. A., Borsa,A., Minster, B., Carabajal, C., Quinn, K., Bills, B. (2005). "Assessment of ICESat performance at the salar de Uyuni, Bolivia." Geophysical Research Letters 32(21).

Gilbert, L., S. Baker, et al. (2014). “REAPER Product Handbook for ERS Altimetry Reprocessed Products” Mullard Space Science Laboratory (MSSL), University College London 3.1: REA-UG-PHB-7003

Gunter, B., T. Urban, et al. (2009). "A comparison of coincident GRACE and ICESat data over Antarctica." Journal of Geodesy 83(11): 1051-1060.

Gunter, B. C., O. Didova, et al. (2014). "Empirical estimation of present-day Antarctic glacial isostatic adjustment and ice mass change." The Cryosphere 8(2): 743-760.

Haran, T., J. Bohlander, T. Scambos, T. Painter, and M. Fahnestock (2014). "MODIS Mosaic of Antarctica 2008-2009 (MOA2009) Image Map." Boulder, Colorado USA: National Snow and Ice Data Center. .

Helm, V., A. Humbert, et al. (2014). "Elevation and elevation change of Greenland and Antarctica derived from CryoSat-2." The Cryosphere Discuss. 8(2): 1673-1721.

Helsen, M. M., M. R. van den Broeke, et al. (2008a). "Elevation Changes in Antarctica Mainly Determined by Accumulation Variability." Science 320(5883): 1626-1629.

Helsen, M. M., M. R. van den Broeke, et al. (2008b). "Elevation Changes in Antarctica Mainly Determined by Accumulation Variability. Supplementary information" Science 320(5883): 1626-1629.

Herron, M., and Langway, C. (1980). "Firn Densification: An emperical model." Journal of Glaciology 25.

Hoffmann, J. (2014). “Ice height changes in East Antarctica derived from satellite laser altimetry.” PhD thesis, The Australian National University.

Horwath, M., B. Legrésy, et al. (2012). "Consistent patterns of Antarctic ice sheet interannual variations from ENVISAT radar altimetry and GRACE satellite gravimetry." Geophysical Journal International 189(2): 863-876.

Howat, I. M., B. E. Smith, et al. (2008). "Rates of southeast Greenland ice volume loss from combined ICESat and ASTER observations." Geophysical Research Letters 35(17): L17505.

Hurkmans, R. T. W. L., J. L. Bamber, et al. (2012). "Brief communication "Importance of slope-induced error correction in volume change estimates from radar altimetry"." The Cryosphere 6(2): 447-451.

Huybrechts, P. (2002). "Sea-level changes at the LGM from ice-dynamic reconstructions of the Greenland and Antarctic ice sheets during the glacial cycles." Quaternary Science Reviews 21(1-3): 203-231.

Ivins, E. R. and T. S. James (2005). "Antarctic glacial isostatic adjustment: a new assessment." Antarctic Science 17(04): 541-553.

Ivins, E. R., T. S. James, et al. (2013). "Antarctic contribution to sea level rise observed by GRACE with improved GIA correction." Journal of Geophysical Research: Solid Earth 118(6): 3126-3141.

Jacka, T. H. and J. Li (1994). "The steady-state crystal size of deforming ice." Annals of Glaciology 20(1): 13-18.

Janjic, T., Schroeter, J., et al. (2012). "Impact of combining GRACE and GOCE gravity data on ocean circulation estimates." Ocean Science 8: 65-79.

Johnston, P. and K. Lambeck (1999). "Postglacial rebound and sea level contributions to changes in the geoid and the Earth’s rotation axis." Geophysical Journal International 136(3): 537-558.

King, M. A., R. J. Bingham, et al. (2012). "Lower satellite-gravimetry estimates of Antarctic sea-level contribution." Nature 491(7425): 586-589.

Kuipers Munneke, P., M. R. van den Broeke, et al. (2011). "A new albedo parameterization for use in climate models over the Antarctic ice sheet." Journal of Geophysical Research: Atmospheres 116(D5).

Kuipers Munneke, P., S. R. M. Ligtenberg, et al. (2015). "A model study of the response of dry and wet firn to climate change." Annals of Glaciology 56(70): 1-8.

Kruizinga and Williams (2015). "GRACE Gravity Recovery and Climate Experiment." CSR Utexas [Online]. Available: http://www.csr.utexas.edu/grace/operations/mission_status/ [2015, February, 02]

Legresy, B., F. Papa, et al. (2005). "ENVISAT radar altimeter measurements over continental surfaces and ice caps using the ICE-2 retracking algorithm." Remote Sensing of Environment 95(2): 150-163.

Lemoine, J.-M., S. Bruinsma, et al. (2007). "Temporal gravity field models inferred from GRACE data." Advances in Space Research 39(10): 1620-1629.

Lemoine et al. (2013). Release 3 of the GRACE gravity solutions from CNES/GRGS. Geophysical Research Abstracts, Vol. 15, EGU2013-11123, 2013. EGU General Assembley, 2013.

Lenaerts, J. T. M. and M. R. van den Broeke (2012). "Modeling drifting snow in Antarctica with a regional climate model: 2. Results." Journal of Geophysical Research: Atmospheres 117(D5): D05109.

Lenaerts, J. T. M., M. R. van den Broeke, et al. (2012). "Modeling drifting snow in Antarctica with a regional climate model: 1. Methods and model evaluation." Journal of Geophysical Research: Atmospheres 117(D5): D05108.

Lenaerts, J. T. M., M. R. van den Broeke, et al. (2012). "A new, high-resolution surface mass balance map of Antarctica (1979–2010) based on regional atmospheric climate modeling." Geophysical Research Letters 39(4): L04501.

Lenaerts, J. T. M., E. van Meijgaard, et al. (2013). "Recent snowfall anomalies in Dronning Maud Land, East Antarctica, in a historical and future climate perspective." Geophysical Research Letters 40(11): 2684-2688.

Li, J. and H. J. Zwally (2004). "Modeling the density variation in the shallow firn layer." Annals of Glaciology 38(1): 309-313.

Li, J. and H. J. Zwally (2010). "Firn-compaction modeling of ice-sheet elevation changes driven by variation of accumulation and temperature for estimating mass changes from observed dH/dt." 59A076-IGS Ohio meeting.

Li, J. and H. J. Zwally (2011). "Modeling of firn compaction for estimating ice-sheet mass change from observed ice-sheet elevation change." Annals of Glaciology.

Ligtenberg, S. R. M., Helsen, M.M. and van den Broeke, M.R. (2011). "An improved semi-emperical model for the densification of Antarctic firn." The Cryosphere 5: 809-819.

Ligtenberg, S. (2014). "The present and future state of the Antarctic firn layer." PhD thesis, Institute for Marine and Atmospheric research Utrecht University.

Ligtenberg, S. R. M., J. T. M. Lenaerts, et al. (2014). "On the formation of blue ice on Byrd Glacier, Antarctica." Journal of Glaciology 60(219): 41-50.

Maris, M.N.A., B. de Boer, et al. (2012). "A climate model intercomparison for the Antarctic region: present and past." Clim. Past **8**(2): 803-814.

McCarthy, D.D. and Petit, G (2003). IERS Conventions (2003). IERS Technical Note 32, Frankfurt am Main: Verlag des Bundesamts für Kartographie und Geodäsie, 2004

Melachroinos, S., J.-M. Lemoine, et al. (2009). "Quantifying FES2004 S2 tidal model from multiple space-geodesy techniques, GPS and GRACE, over North West Australia." Journal of Geodesy 83(10): 915-923.

Michel, A. l., T. Flament, et al. (2014). "Study of the Penetration Bias of ENVISAT Altimeter Observations over Antarctica in Comparison to ICESat-Observations." Remote Sensing 6(10): 9412-9434.

Moholdt, G., C. Nuth, et al. (2010). "Recent elevation changes of Svalbard glaciers derived from ICESat laser altimetry." Remote Sensing of Environment 114(11): 2756-2767.

Monaghan, A. J. and B., David H. (2008). "Advances in describing recent Antarctic climate variabilty." American Meteorological Society.

Mouginot J., B. S. and E. R. (2012). "Mapping of Ice Motion in Antarctica Using Synthetic-Aperture Radar Data." Remote Sensing, doi 10.3390/ rs4092753.

Nakada, M., R. Kimura, et al. (2000). "Late Pleistocene and Holocene melting history of the Antarctic ice sheet derived from sea-level variations." Marine Geology 167(1-2): 85-103.

Nakada, M. and K. Lambeck (1988). "The melting history of the late Pleistocene Antarctic ice sheet." Nature 333(6168): 36-40.

Nakada, M. and L., K. (1989). "Late Pleistocene and Holocene sea-level change in the Australian region and mantle rheology." Geophys. J. 96: 497-517.

Nguyen, A. T.-T. (2006). “Height change detection in Antarctica using satellite altimetry data and Kriging / Kalman filtering techniques.” PhD thesis, Massachusetts Institute of Technology.

Okuno, J. i. and H. Miura (2013). "Last deglacial relative sea level variations in Antarctica derived from glacial isostatic adjustment modelling." Geoscience Frontiers 4(6): 623-632.

Pagiatakis, S. D. (1990). "The response of a realistic earth to ocean tide loading." Geophysical Journal International 103(2): 541-560.

Parish, T. R. and D. H. Bromwich (2007). "Reexamination of the Near-Surface Airflow over the Antarctic Continent and Implications on Atmospheric Circulations at High Southern Latitudes." Monthly Weather Review 135(5): 1961-1973.

Peltier, W. R. (2002). "On eustatic sea level history: Last Glacial Maximum to Holocene." Quaternary Science Reviews 21(1-3): 377-396.

Peltier, W. R. (2004). "Global glacial isostasy and the surface of the ice-age earth: The ice-5G (VM2) model and grace." Annual Review of Earth and Planetary Sciences 32: 111-149.

Peltier, W. R., D. F. Argus, et al. (2015). "Space geodesy constrains ice age terminal deglaciation: The global ICE-6G_C (VM5a) model." Journal of Geophysical Research: Solid Earth: 2014JB011176.

Pritchard, H. D., R. J. Arthern, et al. (2009a). "Extensive dynamic thinning on the margins of the Greenland and Antarctic ice sheets." Nature 461(7266): 971-975.

Pritchard, H. D., R. J. Arthern, et al. (2009b). "Extensive dynamic thinning on the margins of the Greenland and Antarctic ice sheets. Supplementary information" Nature 461(7266): 971-975.

Pritchard, H. D., S. B. Luthcke, et al. (2010). "Understanding ice-sheet mass balance: progress in satellite altimetry and gravimetry." Journal of Glaciology 56(200): 1151-1161.

Purcell, A., Dehecq, A. et al. (2011). "Relationship between glacial isostatic adjustment and gravity perturbations observed by GRACE." Geophys. Res. Lett. 38.

Rémy, F. d. r., T. Flament, et al. (2014). "Ice sheet survey over Antarctica using satellite altimetry: ERS-2, Envisat, SARAL/AltiKa, the key importance of continuous observations along the same repeat orbit." International Journal of Remote Sensing 35(14): 5497-5512.

Ramillien, G., F. Frappart, et al. (2005). "Time variations of land water storage from an inversion of 2 years of GRACE geoids." Earth and Planetary Science Letters 235(1-2): 283-301.

Ramillien, G., A. Lombard, et al. (2006). "Interannual variations of the mass balance of the Antarctica and Greenland ice sheets from GRACE." Global and Planetary Change 53(3): 198-208.

Ray, R. D. and Ponte, R.M. (2003). "Barometric tides from ECMWF operational analyses." Ann. Geophy. 21.

Reeh, N. (2008). "A nonsteady-state firn-densification model for the percolation zone of a glacier." Journal of Geophysical Research 113.

Reeh, N., D. A. Fisher, et al. (2005). "An empirical firn-densification model comprising ice lenses." Annals of Glaciology 42(1): 101-106.

Reijmer, C. H., E. van Meijgaard, et al. (2005). "Evaluation of temperature and wind over Antarctica in a Regional Atmospheric Climate Model using 1 year of automatic weather station data and upper air observations." J. Geophys. Res. 110(D4): D04103.

Rémy, F. and M. Frezzotti (2006). "Antarctica ice sheet mass balance." Comptes Rendus Geosciences 338(14-15): 1084-1097.

Riffenburgh, B. (2006). Encyclopedia of the Antarctic. Hoboken, Routledge.

Rignot, E. (2006). "Changes in ice dynamics and mass balance of the Antarctic ice sheet.” Phil. Trans. R. Soc. A 2006 364 1637-1655:DOI: 10.1098/rsta. 2006.1793

Rignot, E., J. L. Bamber, et al. (2008). "Recent Antarctic ice mass loss from radar interferometry and regional climate modelling." Nature Geosci 1(2): 106-110.

Rignot, E., S. Jacobs, et al. (2013). "Ice-Shelf Melting Around Antarctica." Science 341(6143): 266-270.

Rignot, E. and S. S. Jacobs (2002). "Rapid Bottom Melting Widespread near Antarctic Ice Sheet Grounding Lines." Science 296(5575): 2020-2023.

Rignot, E., J. Mouginot, et al. (2011a). "Antarctic grounding line mapping from differential satellite radar interferometry." Geophysical Research Letters 38(10): L10504.

Rignot, E., J. Mouginot, et al. (2011b). "MEaSUREs InSAR-Based Antarctica Velocity Map." Boulder, Colorado USA: NASA EOSDIS Distributed Active Archive Center at NSIDC Accessed on [03/04/2015]. http://nsidc.org/data/nsidc-0484.html.

Rignot, E., I. Velicogna, et al. (2011c). "Acceleration of the contribution of the Greenland and Antarctic ice sheets to sea level rise." Geophysical Research Letters 38(5): L05503.

Rignot, E. and R. H. Thomas (2002). "Mass Balance of Polar Ice Sheets." Science 297(5586): 1502-1506.

Riva, R. E. M., B. C. Gunter, et al. (2009). "Glacial Isostatic Adjustment over Antarctica from combined ICESat and GRACE satellite data." Earth and Planetary Science Letters 288(3-4): 516-523.

Robin, G. d. Q. (1958). Seismic Shooting and Related Investigations, Norsk Polarinstitutt.

Sasgen, I., H. Dobslaw, et al. (2010). "Satellite gravimetry observation of Antarctic snow accumulation related to ENSO." Earth and Planetary Science Letters 299(3,4): 352-358.

Sasgen, I., H. Konrad, et al. (2013). "Antarctic ice-mass balance 2003 to 2012: regional reanalysis of GRACE satellite gravimetry measurements with improved estimate of glacial-isostatic adjustment based on GPS uplift rates." The Cryosphere 7(5): 1499-1512.

Sasgen, I., M. van den Broeke, et al. (2012). "Timing and origin of recent regional ice-mass loss in Greenland." Earth and Planetary Science Letters 333-334(0): 293-303.

Scambos, T. A., T. M. Haran, et al. (2007). "MODIS-based Mosaic of Antarctica (MOA) data sets: Continent-wide surface morphology and snow grain size." Remote Sensing of Environment 111(2-3): 242-257.

Scarchilli, C., Frezzotti, M., et al. (2010). "Extraordinary blowing snow transport events in East Antarctica." Climate Dynamics 34: 1195-1206.

Schlosser, E., J. G. Powers, et al. (2010). "An extreme precipitation event in Dronning Maud Land, Antarctica: a case study with the Antarctic Mesoscale Prediction System." Polar Research 29(3): 330-344.

Schutz, B. and Zwally, H.J (2008). "Overview of the Science Results from ICESat." 16th International Workshop On Laser Ranging, Poznan Poland.

Schutz, B. E., H. J. Zwally, et al. (2005). "Overview of the ICESat Mission." Geophysical Research Letters 32(21): L21S01.

Shepherd, A., E. R. Ivins, et al. (2012). "A Reconciled Estimate of Ice-Sheet Mass Balance." Science 338(6111): 1183-1189.

Simonsen, S. B., L. Stenseng, et al. (2013). "Assessing a multilayered dynamic firn-compaction model for Greenland with ASIRAS radar measurements." Journal of Glaciology 59(215): 545-558.

Slobbe, D. C., Lindenbergh, R.C. and Ditmar, P. (2008). "Estimation of volume change rates of Greenland's ice sheet from ICESat data using overlapping footprints." Remote Sensing of Environment 112.

Smith, B. E., H. A. Fricker, et al. (2009). "An inventory of active subglacial lakes in Antarctica detected by ICESat (2003-2008)." Journal of Glaciology 55(192): 573-595.

Solomon et al. (2007). “IPCC, 2007: Climate Change 2007: The Physical Science Basis. Contribution of Working Group I to the Fourth Assessment Report of the Intergovernmental Panel on Climate Change.” Cambridge University Press, Cambridge, United Kingdom and New York, NY, USA, 996 pp.

Sørensen, L. S., Simonsen, S.B., et al. (2011). "Mass balance of the Greenland ice sheet (2003-2008) from ICESat data-the impact of interpolation, sampling and firn density." The Cryosphere 5: 173-186.

Steffen, H. and P. Wu (2011). "Glacial isostatic adjustment in Fennoscandia -A review of data and modeling." Journal of Geodynamics 52(3-4): 169-204.

Sutterley, T. C., I. Velicogna, et al. (2014). Evaluating Greenland glacial isostatic adjustment corrections using GRACE, altimetry and surface mass balance data.

Swenson, S. and J. Wahr (2009). "Monitoring the water balance of Lake Victoria, East Africa, from space." Journal of Hydrology 370(1-4): 163-176.

Tapley, B. D., S. Bettadpur, et al. (2004). "The gravity recovery and climate experiment: Mission overview and early results." Geophys. Res. Lett. 31(9): L09607.

Tietäväinen, H. and T. Vihma (2008). "Atmospheric moisture budget over Antarctica and the Southern Ocean based on the ERA-40 reanalysis." International Journal of Climatology 28(15): 1977-1995.

Tregoning, P., Twilley, B., Hendy, M. and Zwartz, D. (1999). "Monitoring isostatic rebound in Antarctica using continuous remote GPS observations."

Tregoning, P., G. Ramillien, et al. (2009). "Glacial isostatic adjustment and nonstationary signals observed by GRACE." J. Geophys. Res. 114(B6): B06406.

Tregoning, P., C. Watson, et al. (2009). "Detecting hydrologic deformation using GRACE and GPS." Geophys. Res. Lett. 36(15): L15401.

van de Berg, W. J., M. R. van den Broeke, et al. (2006). "Reassessment of the Antarctic surface mass balance using calibrated output of a regional atmospheric climate model." Journal of Geophysical Research: Atmospheres 111(D11): D11104.

van den Broeke, M. R. (2007). "Climate Oscillactions." in B. Riffenburgh (Ed.): Encyclopedia of the Antarctic, Routledge New York: 1146 pp.

van den Broeke, M. (2008). "Depth and Density of the Antarctic Firn Layer." Arctic, Antarctic, and Alpine Research 40(2): 432-438.

van den Broeke, M., W. J. van de Berg, et al. (2006). "Identification of Antarctic ablation areas using a regional atmospheric climate model." J. Geophys. Res. 111(D18): D18110.

Velicogna, I. (2009). "Increasing rates of ice mass loss from the Greenland and Antarctic ice sheets revealed by GRACE." Geophysical Research Letters 36(19): L19503.

Velicogna, I. and J. Wahr (2002). "A method for separating Antarctic postglacial rebound and ice mass balance using future ICESat Geoscience Laser Altimeter System, Gravity Recovery and Climate Experiment, and GPS satellite data." J. Geophys. Res. 107(B10): 2263.

Velicogna, I. and J. Wahr (2006). "Measurements of Time-Variable Gravity Show Mass Loss in Antarctica." Science 311(5768): 1754-1756.

Velicogna, I. and J. Wahr (2013). "Time-variable gravity observations of ice sheet mass balance: Precision and limitations of the GRACE satellite data." Geophysical Research Letters 40(12): 3055-3063.

Wahr, J., DaZhong, H. and Trupin, A. (1995). "Predictions of vertical uplift caused by changing polar ice volumes on a viscoelastic earth." Geophys. Res. Lett. 22: 977-980.

Wahr, J., M. Molenaar, et al. (1998). "Time variability of the Earth's gravity field: Hydrological and oceanic effects and their possible detection using GRACE." J. Geophys. Res. 103(B12): 30205-30229.

Wahr, J., S. Swenson, et al. (2006). "Accuracy of GRACE mass estimates." Geophys. Res. Lett. 33(6): L06401.

Wahr, J., Wingham, D. and Bentley, C. (2000). "A method of combining ICESat and GRACE satellite data to constrain Antarctic mass balance." Journal of Geophysical Research 105.

Watson, C. S., N. J. White, et al. (2015). "Unabated global mean sea-level rise over the satellite altimeter era." Nature Clim. Change advance online publication.

Whitehouse, P. L., M. J. Bentley, et al. (2012). "A deglacial model for Antarctica: geological constraints and glaciological modelling as a basis for a new model of Antarctic glacial isostatic adjustment." Quaternary Science Reviews 32(0): 1-24.

Whitehouse, P. L., M. J. Bentley, et al. (2012). "A new glacial isostatic adjustment model for Antarctica: calibrated and tested using observations of relative sea-level change and present-day uplift rates." Geophysical Journal International 190(3): 1464-1482.

Whitehouse, P. L. and S. L. Bradley (2013). SEA LEVEL STUDIES | Eustatic Sea-Level Changes Since the Last Glacial Maximum. Encyclopaedia of Quaternary Science (Second Edition). S. A. E. J. Mock. Amsterdam, Elsevier: 439-451.

Williams, S. D. P., P. Moore, et al. (2014). "Revisiting GRACE Antarctic ice mass trends and accelerations considering autocorrelation." Earth and Planetary Science Letters 385(0): 12-21.

Wingham, D. J., C. R. Francis, et al. (2006). "CryoSat: A mission to determine the fluctuations in Earth’s land and marine ice fields." Advances in Space Research 37(4): 841-871.

Wingham, D. J., A. J. Ridout, et al. (1998). "Antarctic Elevation Change from 1992 to 1996." Science 282(5388): 456-458.

Wu, X., M. B. Heflin, et al. (2010). "Simultaneous estimation of global present-day water transport and glacial isostatic adjustment." Nature Geoscience 3(9): 642-646.

Zwally, H. J., Giovinetto, M.B., Li, J., Cornejo, H.G., Beckley, M.A., Brenner, A.C., Saba, J.L., Yi, D. (2005). "Mass changes of the Greenland and Antarctic ice sheets and shelves and contributions to sea-level rise: 19922002." Journal of Glaciology 51: 509-527.

Zwally, H. J. and Li, J. (2002). "Seasonal and interannual variations of firn densification and ice-sheet surface elevation at the Greenland summit." Journal of Glaciology 48(161): 199-207.

Zwally, H. J., Li, J., et al. (2011). "Greenland ice sheet mass balance: distribution of increased mass loss with climate warming; 200307 versus 19922002." Journal of Glaciology 57(201): 88-102.

Zwally, H. J., Schutz, B. et al. (2002). "ICESat'l laser measurements of polar ice, atmosphere, ocean and land." Journal of Geodynamics 34: 405-445.

Zwartz, D., M. Bird, et al. (1998). "Holocene sea-level change and ice-sheet history in the Vestfold Hills, East Antarctica." Earth and Planetary Science Letters 155(1-2): 131-145.